

DOT/FAA/AR-98/72

Office of Aviation Research
Washington, D.C. 20591

Evaluation of Technologies for the Design of a Prototype In-Flight Remote Aircraft Icing Potential Detection System

December 1998

Final Report

This document is available to the U.S. public
through the National Technical Information
Service (NTIS), Springfield, Virginia 22161.



U.S. Department of Transportation
Federal Aviation Administration

NOTICE

This document is disseminated under the sponsorship of the U.S. Department of Transportation in the interest of information exchange. The United States Government assumes no liability for the contents or use thereof. The United States Government does not endorse products or manufacturers. Trade or manufacturer's names appear herein solely because they are considered essential to the objective of this report.

This report is available at the Federal Aviation Administration William J. Hughes Technical Center's Full-Text Technical Reports page: www.tc.faa.gov/its/act141/reportpage.html in Adobe Acrobat portable document format (PDF).

1. Report No. DOT/FAA/AR-98/72		2. Government Accession No.		3. Recipient's Catalog No.	
4. Title and Subtitle EVALUATION OF TECHNOLOGIES FOR THE DESIGN OF A PROTOTYPE IN-FLIGHT REMOTE AIRCRAFT ICING POTENTIAL DETECTION SYSTEM				5. Report Date December 1998	
				6. Performing Organization Code	
7. Author(s) James B. Mead, Andrew Pazmany, and Mark Goodberlet				8. Performing Organization Report No.	
9. Performing Organization Name and Address Quadrant Engineering Inc. 107 Sunderland Road Amherst, MA 01002				10. Work Unit No. (TRAIS)	
				11. Contract or Grant No. DACA39-97-M-1476	
12. Sponsoring Agency Name and Address U.S. Department of Transportation Federal Aviation Administration Office of Aviation Research Washington, DC 20591				13. Type of Report and Period Covered Final Report	
				14. Sponsoring Agency Code AIR-100	
15. Supplementary Notes Administered by US Army Cold Regions Research and Engineering Laboratory, Snow and Ice Division, Hanover, NH 03755-1290 The Federal Aviation Administration William J. Hughes Technical Center COTR was Edward Pugacz.					
16. Abstract <p>This document presents the results of an investigation of remote sensing technologies applicable to the problem of remote aircraft icing potential detection. The long-term goal is to develop an aircraft mounted sensor capable of detecting dangerous levels of supercooled liquid water tens of kilometers ahead of the aircraft. Instruments capable of mapping range profiles of cloud liquid water content and mean particle size were investigated, specifically multifrequency radar and lidar (light detection and ranging). Multifrequency radar proved to be the most promising method for detecting liquid water content and parameters related to particle size. Backscattered power measurements at one, two, and three frequencies were input to a neural network trained to estimate liquid water content and two sizing parameters. This investigation showed that both two- and three-frequency radars were able to extract liquid water content and particle size parameters for various trial distributions of clouds and precipitation. Accuracy was highest for the three-frequency algorithm, especially in the estimation of liquid water content. Instruments capable of providing horizontal profiles of air temperature were also investigated, because they potentially provide a means of detecting regions of warmer air, free of supercooled drops. The technologies studied for temperature profiling were oxygen band radiometry and a radar-acoustic sensor. Neither of these technologies was deemed promising enough to warrant further development within the current program.</p>					
17. Key Words Multifrequency radar, Remote sensing, Liquid water content			18. Distribution Statement Document is available to the public through the National Technical Information Service (NTIS), Springfield, Virginia 22161.		
19. Security Classif. (of this report) Unclassified		20. Security Classif. (of this page) Unclassified		21. No. of Pages 83	
				22. Price	

TABLE OF CONTENTS

	Page
EXECUTIVE SUMMARY	xi
1 INTRODUCTION	1
1.1 Multiparameter Radar	1
1.2 Polarimetric Lidar	2
1.3 Temperature Profiling Techniques	2
2 MULTIPARAMETER RADAR	2
2.1 Radar Configuration	3
2.2 Neural Network Classification of Particle Parameters	5
2.2.1 Training and Test Data	9
2.2.2 Drop-Size Distributions	10
2.2.3 Inversion of Particle Parameters With Randomly Varying Conditions	13
2.2.4 Simulation of Stratus Layer	15
2.2.5 Modified Gamma Distributions Used to Represent All Clouds, Rain, and Drizzle	17
2.2.6 Summary of Multifrequency Inversion Study	21
2.3 Polarimetric Radar	23
2.4 Scanning Strategy	26
2.5 Signal-to-Noise Analysis	29
2.5.1 Minimum Detectable Particle Size	31
2.5.2 Statistical Analysis of Range Performance	33
2.5.3 Sensitivity of Solid-State Radar	34
3 LIDAR	37
4 TEMPERATURE PROFILING	40
4.1 Oxygen Band Radiometry	40
4.2 Temperature Profiling Using RASS	41
4.3 Summary of Temperature Profiling Research	44

5	MULTIFREQUENCY RADOME AND LOSSES DUE TO ICE AND WATER	44
6	PROPOSED PROTOTYPE SYSTEM DESIGN	48
7	CONCLUSIONS	51
8	BIBLIOGRAPHY	52
9	GLOSSARY	54

APPENDICES

- A—Atmospheric Temperature Profiling by Radiometers
- B—Front-End Loss Effects on Radiometer Performance

LIST OF FIGURES

Figure	Page
1 Geometry for Airborne Multifrequency Radar	3
2 Using a Single Multiple-Frequency Feed Horn to Generate Colocated Beams at Several Frequencies	4
3 Pulsed and FM-CW Radar Configurations	5
4 Neural Network Estimation of Cloud Parameters Is Derived Solely From Measured Profiles of Reflectivity, $Z_{m1} - Z_{m5}$ at One, Two, or Three Frequencies	7
5 Network Topology for Single Input Frequency Neural Network	8
6 Simulation Software Flow Chart	9
7 Typical Particle Diameter Distribution, $p_d(d)$, Associated Volume Distribution, $p_v(d)$, and Reflectivity Distribution, $p_z(d)$	11
8 Range of Distribution Shapes for Smallest Mode Radius	12
9 Range of Distribution Shapes for Drizzle	12
10 Range of Distribution Shapes for Rain	13
11 Scatter Plot of dBZ Versus MVD and Liquid Water Content for the Training Data Set and Test Data Set	14
12 Scatter Plots of Estimated Versus Input Liquid Water Content, MVD, and MZD for Totally Random Profile of Cloud and Precipitation Conditions Using One Frequency, Two Frequencies, and Three Frequencies	16
13 Scatter Plots of Estimated Versus Input Liquid Water Content, MVD, and MZD for Stratus Layer With 90 Percent Profile-to-Profile Overlap of Cloud Conditions Using One Frequency, Two Frequencies, and Three Frequencies	18
14 Scatter Plots of Estimated Versus Input Liquid Water Content, MVD, and MZD for Stratus Layer With 75 Percent Profile-to-Profile Overlap of Cloud Conditions Using One Frequency, Two Frequencies, and Three Frequencies	20
15 Results for Cloud, Drizzle, and Rain Model Using Modified Gamma Distributions Using One Frequency, Two Frequencies, and Three Frequencies	22
16 Sector Scan With Three-Frequency Radar	26

17	Beam Averaging to Achieve Common Sample Volume	27
18	Number of Averages Versus Maximum Range With Update Rate as a Parameter	28
19	Cloud Reflectivity in dBZ as a Function of Liquid Water Content With Particle Size as a Parameter	30
20	Atmospheric Extinction Due to Scattering and Absorption by Liquid Water at 0°C	31
21	Minimum Detectable Particle Diameter Versus Range With Liquid Water Content as a Parameter at 10, 35, and 95 GHz	32
22	Cumulative Distribution Function and Highest 20 Percent of CDF for Simulated Cloud Liquid Water Content	33
23	Simulated Temperature Distribution	33
24	Typical Range Profiles of Liquid Water and Temperature	34
25	Minimum Detectable Reflectivity Versus Range With Simulated Cloud Liquid and Temperature Distribution at 10, 35, and 95 GHz for a Tube-Powered System	35
26	Minimum Detectable Reflectivity for Solid-State Radars With Simulated Cloud Liquid and Temperature Distribution at 10, 35, and 95 GHz	36
27	Optical Extinction Coefficient for Liquid Water Contents Between 0.001 and 1 gram/Cubic Meter	37
28	Liquid Water Content Versus Rain Rate	38
29	Large Droplet Particle Sizing Using Three-Frequency Neural Network and Three-Frequency Neural Network Plus Lidar	39
30	Radar Acoustic Sounding System Concept	41
31	Airborne RASS Concept	42
32	Airborne RASS Geometry	42
33	Phase Error in Degrees Versus Illumination Angle θ	43
34	RASS SNR Versus Range	44
35	Radome Showing Ice and Water Buildup	45

36	One-Way Transmission Loss of Dry Radome and Radome Coated With 1 cm of Ice and 0.3 mm of Water	46
37	Transmission Loss as a Function of Ice Thickness	46
38	Transmission Loss as a Function of Ice Thickness With 0.3-mm Coating of Water	47
39	Transmission Loss as a Function of Water Thickness Assuming Ice Thickness of 1 cm	47
40	Transmission Loss as a Function of Water Thickness Without Ice	48
41	System Block Diagram of the Proposed Multifrequency Radar	49
42	Receiver Block Diagram	50

LIST OF TABLES

Table		Page
1	Summary of Estimation Errors for One-, Two-, and Three-Frequency Radar Estimates of Liquid Water Content, MVD, and MZD	24
2	Absorption Due to Water Vapor for Saturation Conditions at 800 mb	30
3	Parameters for a High-Powered, Tube-Pulsed Radar Used in Estimating Range Performance of Multifrequency Radar	31
4	Parameters Used in Estimating Range Performance of Solid-State FM-CW Multifrequency Radar	34
5	Conditions for Evaluating Equation 31	43
6	Conditions Used in Predicting SNR for Airborne RASS	44
7	Specifications for the Proposed Multiparameter Radar	50

DEFINITION OF VARIABLES

a	bias factor in radiometric calibration
A_i	two-way atmospheric attenuation (dB)
α	shape parameter for gamma distribution; larger values of α yield a narrower distribution, also averaging kernel in appendix A
b	shape parameter for the Marshall-Palmer distribution; also calibration bias term in appendix B
B	receiver bandwidth (Hz)
β	antenna beamwidth (radians)
β_x	antenna beamwidth at X-band (radians)
c	speed of light (2.997×10^8 meters/second)
C	correlation factor ($0 < C < 1$) to determine overlap between range gates
δ	variable used to express linear depolarization ratio in lidar
d	particle diameter (m)
f	frequency (Hertz)
f_p	radar pulse repetition frequency (often PRF)
γ	shape parameter for gamma distribution, larger values of γ yield narrower distributions
G	antenna gain
k_e	electromagnetic wavenumber (radians/m)
k_w	extinction due to liquid water (dB/km)
K	complex quantity related to the index of refraction of water or ice
λ	electromagnetic wavelength (m)
l	ice ohmic loss
L_a	atmospheric loss (dB/km)
m_v	liquid water content ($g \cdot m^{-3}$)
η	volume backscattering coefficient ($m^2 \cdot m^{-3}$)
n	index of refraction
N_i	number of input nodes in neural network
N_r	number of range gates sampled by neural network
N_f	number of frequencies sampled by neural network
N_p	number of parameters output by neural network
N_o	number of output nodes in neural network

N_{ave}	number of radar samples averaged (power average)
N_0	number density parameter for the Marshall-Palmer distribution
ϕ	general angular variable
Φ_{az}	scan range in azimuth (radians)
Φ_{el}	scan range in elevation (radians)
$p(r)$	drop size distribution (number of drops per cubic meter per meter diameter)
P_t	transmit power (W)
P_{rmin}	minimum detectable received power (W)
r_c	mode radius (radius corresponding to the peak value of the drop size distribution)
r	particle radius (μ m); also ice reflective loss (appendix B)
R	radar range (m)
R_{max}	maximum unambiguous radar range (m), determined by f_p .
R_r	rain rate (mm/hr)
$SDTB$	standard deviation of the measured brightness temperature (K)
τ	pulse length (s)
θ	general angular variable
T	time variable (s)
T_I	time traveled by aircraft during acoustic propagation
T	temperature (K)
T_a	antenna temperature (K)
T_r	brightness temperature of radiometer propagating toward antenna (K)
T_s	time required to scan entire sample volume (s)
T_{sys}	system noise temperature (K)
ΔT	radiometric temperature measurement precision, (K)
v	aircraft velocity (m/s)
V_s	speed of sound (m/s)
Z	cloud reflectivity ($mm^6 \cdot m^{-3}$). Z_{vv} is the copolarized reflectivity for transmission and reception of vertical polarization; Z_{hh} is the copolarized reflectivity for transmission and reception of horizontal polarization; Z_{vh} is the cross-polarized reflectivity, for transmission of horizontal and reception of vertical polarization.
Z_{dr}	differential reflectivity, equal to the ratio of Z_{hh} to Z_{vv}

EXECUTIVE SUMMARY

This document presents the results of an investigation of remote sensing technologies applicable to the problem of aircraft icing potential detection. The long-term goal is to develop an aircraft-mounted sensor capable of detecting dangerous levels of supercooled liquid water tens of kilometers ahead of the aircraft. Clouds with supercooled liquid water exhibit a potential for icing that is a function of water content, and to some degree, the range of droplet diameters [14 CFR Part 25 Appendix C]. Appendix C conditions are dangerous to aircraft without ice protection; however, they are not dangerous to most aircraft with ice protection. Instruments capable of mapping cloud liquid water content and mean particle size were investigated. Furthermore, instruments capable of probing air temperature were also investigated, in as much as they may provide a means of detecting regions of warmer air where drops are not supercooled.

REMOTE SENSING OF DROPLET SIZE AND LIQUID WATER CONTENT.

Two technologies were evaluated for estimation of cloud particle size and water content, specifically, multiparameter radar¹ and lidar (light detection and ranging). Multifrequency radar proved to be the most promising method. A neural network was trained to estimate cloud parameters using backscattered power measurements at one, two, and three frequencies, spanning 10 to 95 GHz. The network was trained to measure liquid water content and two sizing parameters: the diameter corresponding to the mean drop volume and the diameter corresponding to the mean radar reflectivity. In all cases the range resolution was set to 2 km, although range performance can be traded off against measurement precision if finer ranging is required. This investigation showed that both two- and three-frequency radars were able to extract liquid water content and particle size parameters for various trial distributions of clouds and precipitation. Error analysis showed from 25% to 100% improvement in estimation of liquid water content for the three-frequency radar as compared to a dual-frequency sensor.

For long range sensing of cloud parameters, optical attenuation in clouds is too high for lidar to be used as a stand-alone instrument. Adding a lidar channel to the three-frequency radar neural network algorithm yielded a small improvement in particle sizing. However, this is only applicable to conditions of low optical attenuation, such as in drizzle below the cloud base. The addition of a lidar channel will be of limited value, given the inability of lidar to penetrate optically thick cloud layers.

POLARIMETRIC RADAR.

Polarimetric research radars can measure up to nine independent scattering parameters related to the shape and orientation of cloud particles. These parameters are useful in detecting the presence of certain ice habits, hail, and large liquid droplets. Due to their small size, supercooled liquid cloud droplets are nearly spherical and therefore present a uniform polarimetric signature showing no depolarization. The main advantage of a polarimetric radar is its ability to detect the presence of ice in mixed-phase clouds. This information can be used in inversion algorithms to improve particle size estimates that are biased to larger sizes by the presence of ice.

¹ A multiparameter radar combines various functions, in this case, a multiple frequency radar with polarimetric and velocity measurement capability.

RANGE PERFORMANCE OF MULTIFREQUENCY RADAR.

A statistical study of the range performance of tube-powered and solid-state radars was carried out for 10-, 35-, and 95-GHz systems appropriate for a compact airborne sensor. Using statistics of stratus clouds taken from published reports, it was shown that tube-powered 10- and 35-GHz radars had a high probability of detecting supercooled clouds to ranges of 30 kilometers or more. Range performance at 95 GHz is more strongly impacted by attenuation so that clouds with drops in the range of 80-430 micrometers fall below the detection threshold 10 percent of the time at 30-kilometers range. Therefore, a three-frequency inversion algorithm would be configured to revert to a two-frequency algorithm in cases when the 95-GHz signal level fell below the detection threshold.

TEMPERATURE PROFILING.

Two techniques were investigated for remote temperature profiling: multichannel radiometry in the 50- to 60-GHz band and a technique known as Radar Acoustic Sounding System (RASS). These techniques are currently in use for vertical temperature profiling from fixed ground sites. Both techniques appear feasible over short ranges (a few km) but are severely limited at longer ranges. Although horizontal profiling over long ranges may be technically impractical, Quadrant Engineering Inc.'s investigation of the 50- to 60-GHz radiometer showed that vertical profiling of temperature may be practical with a small airborne sensor. Such information would be valuable to a pilot seeking warmer air either above or below flight level.

PRELIMINARY DESIGN OF A PROTOTYPE ICING POTENTIAL DETECTION RADAR.

The final section of this report considers the design of a prototype system for detecting cloud parameters associated with aircraft icing. After conducting a statistical analysis of signal to noise in stratus clouds, it was concluded that the proposed three-frequency radar should employ high-powered tube sources (either magnetron or klystron) with peak power levels in excess of 1 kW. Solid-state sources were also considered but resulted in a loss of detection capability of a factor of three to four in mean particle diameter.

SUMMARY OF FINDINGS.

In summary, Quadrant Engineering Inc. has shown that the complex problem of inverting cloud parameters from range profiles of backscattered radar power is feasible with a radar operating at two or more frequencies. Particle sizing was characterized by two parameters: measure of the mean particle size and spread of the size distribution. Addition of a polarimetric capability can reduce biases in size estimation in mixed phase clouds by identifying the presence of ice. The addition of a lidar channel can provide a modest improvement in particle sizing in rain or drizzle but is of little value in remote sensing through optically thick clouds. Horizontal temperature profiling using radiometric techniques and RASS were also investigated. Although both techniques appear viable over short ranges (a few kilometers), neither was found to be sufficient for the longer ranges needed for icing avoidance.

1. INTRODUCTION.

This document presents the results of an investigation of remote sensing technologies applicable to aircraft icing. The long-term goal is to develop an aircraft-mounted sensor capable of detecting dangerous levels of supercooled liquid water tens of kilometers ahead of the aircraft.

Aircraft icing due to supercooled liquid in the atmosphere can significantly deteriorate airworthiness and has been cited for accidents in both military and general aviation [Ryerson, 1996]. Furthermore, icing forecasts have low resolution and are often inaccurate, so aircraft are left to contend with icing or to abandon flying altogether when an icing potential exists. An on-board remote icing potential detection system would forewarn flight crews of hazardous environmental conditions early enough to allow appropriate crew decisions and actions. Once the decision is made to avoid a detected icing environment, air traffic control procedures must be followed and an appropriate flight path determined. Therefore, any practical remote icing potential detection system should be able to look ahead of the aircraft a significant distance (about 20-30 kilometers, although this value is not firmly established).

A number of remote sensing techniques have been investigated or suggested for icing detection [Ryerson, 1997]. To remotely detect icing potential, any instrument or combination of instruments must have the capability of detecting cloud liquid water content and particle size parameters. In addition, the capability of remotely profiling temperature would also be beneficial, although on-board temperature sensors may be adequate to estimate temperature under some conditions. In this study, Quadrant has investigated a number of technologies to detect particle size parameters, liquid water content, and temperature. These technologies are as follows:

- a. Multiparameter radar using two or more frequencies and multiple polarizations to estimate liquid water content and particle size parameters.
- b. Lidar (light detection and ranging) as an aid to multiparameter radar for particle sizing and liquid water estimation.
- c. Oxygen band radiometry to profile air temperature.
- d. Radar Acoustic Sounding System (RASS) to profile air temperature.

A brief review of each technology is given below.

1.1 MULTIPARAMETER RADAR.

Multiparameter radar has the greatest potential for probing cloud particle parameters due to the combination of moderate attenuation and adequate scattering cross section. A working hypothesis was formulated that cloud parameters could be extracted by measuring backscatter at a combination of attenuating and nonattenuating frequencies. Since scattering is a complex nonlinear function of particle size and frequency, it is impractical to consider an *analytical* solution to the inverse problem of computing particle size and liquid water content based on measured backscattered power at multiple frequencies. Quadrant therefore focused its efforts on an approximate numerical solution to the inversion, specifically, a neural network. The network

was trained by simulating thousands of test cases of radar scattering from assumed particle size distributions. The neural network is described in section 2.2, where results of one-, two-, and three-frequency algorithms are compared.

1.2 POLARIMETRIC LIDAR.

From the outset of our research, it was clear that lidar was not a viable stand-alone technique for remote detection of particle size and liquid water content. This is because the optical attenuation coefficient in clouds of small particles can exceed 100 dB/km. However, for drizzle size particles (several hundred micrometers in diameter) the optical attenuation coefficient is moderate. Lidar can improve the accuracy of the multiparameter radar inversion algorithm simply by adding an additional frequency to the inversion. The advantage of adding lidar for drizzle sizing is marginal, however, since it is only applicable below cloud base. Overall, it is difficult to make a strong case for including lidar in an airborne icing avoidance system, since lidar cannot penetrate optically thick clouds.

1.3 TEMPERATURE PROFILING TECHNIQUES.

To our knowledge, there is no established technology or literature on temperature profiling over horizontal paths. Quadrant investigated two potential methods for remote temperature profiling: oxygen band radiometry and RASS. The uniform mixing of oxygen in the atmosphere means that brightness temperature measured near the oxygen absorption bands centered at 60 and 118 GHz depends only on temperature, pressure, and water content. Investigations carried out during this study showed that horizontal range profiles of temperature can be estimated if multiple frequencies are sampled in the 50- to 60-GHz band. This technique is well established for vertical measurement of temperature but has not been applied to horizontal temperature profiling. In section 4.1 the capabilities and limitations of oxygen band radiometry are summarized. A more detailed analysis is presented in appendix A.

Another method for remote detection of temperature is the concept of using a novel implementation of the RASS technique to measure the speed of the acoustic wavefront emitted by the aircraft. Initial calculations showed that a moderately powered radar could detect acoustic scatter from engine noise at distances in excess of 10 km. However, later analysis demonstrated that the radar cross-section of the acoustic wavefront will decrease rapidly as the aircraft moves forward from the locus of the acoustic wavefront. These calculations, presented in section 4.2, suggest that RASS is impractical for airborne temperature profiling. Other difficulties with long-distance RASS include distortion of the acoustic wavefront by turbulence, as well as advection by the mean wind field. Therefore, the technique is also impractical for slower moving aircraft, such as helicopters.

2. MULTIPARAMETER RADAR.

Conventional weather radars, operating between 2 and 10 GHz, sample a single parameter, reflectivity, Z , which is the sixth moment of the particle size distribution, given by

$$Z = \sum_{i=1}^{N_v} d_i^6 \text{ mm}^6/\text{m}^3 \quad (1)$$

where N_v is the number of particles per cubic meter and d_i is the diameter of the i^{th} particle in millimeters. Doppler radars add an additional pair of parameters: the mean and variance of the Z-weighted velocity spectrum of the particles. Vertically pointed radar observations of the velocity spectrum have been used to characterize drop-size distribution from airborne [Galloway et al., 1998] and ground-based installations. For these measurements, the relationship between particle size and fall velocity² can be used to extract the drop-size distribution, provided some means is available to remove vertical air motions. For horizontal observations, there is no equivalent method for extracting particle size from the velocity spectrum. Research weather radars usually add an orthogonal polarization channel that provides five additional parameters related to particle shape and ice/water phase. Some benefit may be derived from adding polarization, especially in detecting pristine crystals or large droplets, as described in section 2.3.

2.1 RADAR CONFIGURATION.

Figure 1 shows the geometry of the multifrequency airborne radar. Radar pulse volume is determined by range resolution, ΔR , and antenna 3-dB one-way beamwidth, delineated by the dashed lines. Two beamwidths are shown in this figure, one for a high-frequency radar and one for a low-frequency radar. A single main reflector can serve two or more frequencies simultaneously, as shown in figure 2. In this configuration, a single feedhorn supporting multiple frequencies and multiple polarization is used, resulting in coaxial beams at all frequencies with no increase in aperture blockage [Sekelsky and McIntosh, 1995]. Frequency reuse of a common aperture is essential for the present application where limited space will be allotted for an airborne icing avoidance antenna. For each frequency, radar sensitivity is inversely proportional to beamwidth. Therefore, it is crucial to use the narrowest beamwidth possible for each frequency, (i.e., use as much of the available antenna area as possible) since sensitivity is likely to be a key performance issue. Although some error may result from unmatched beamwidths, effective beamwidths can be normalized in postprocessing by spatial averaging, as described in section 2.4.

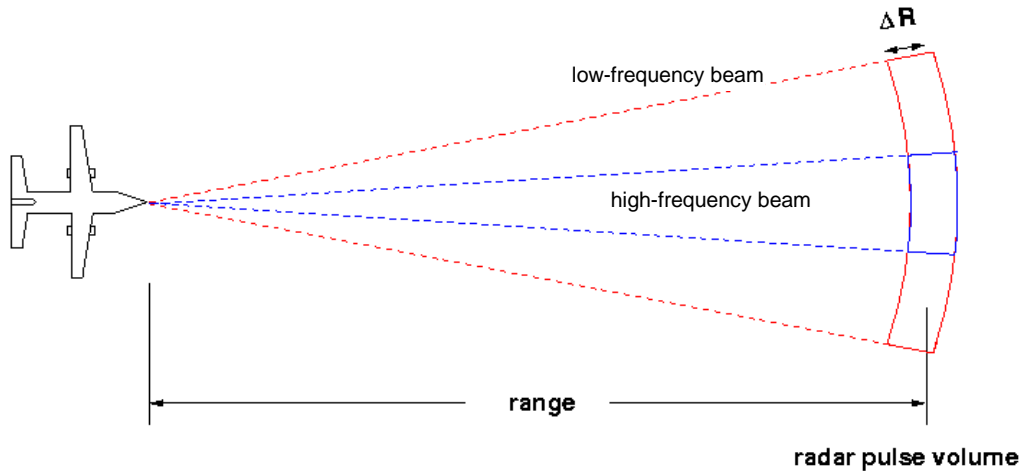


FIGURE 1. GEOMETRY FOR AIRBORNE MULTIFREQUENCY RADAR

² Fall velocity is the vertical velocity of a droplet in the absence of vertical winds.

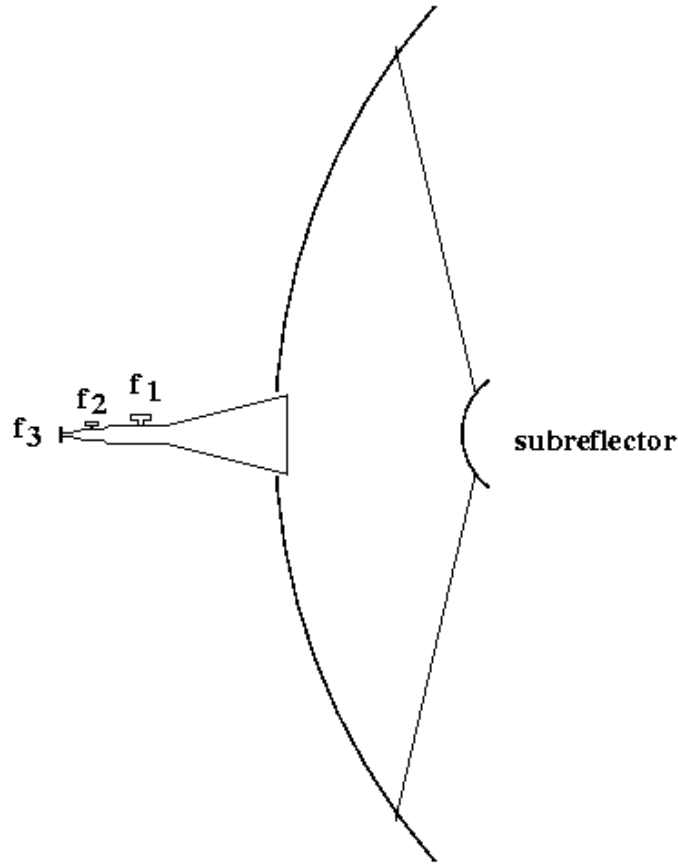


FIGURE 2. USING A SINGLE MULTIPLE-FREQUENCY FEED HORN TO GENERATE COLOCATED BEAMS AT SEVERAL FREQUENCIES
(Feed ports for three frequencies, f_1 , f_2 , and f_3 , are shown.)

Two types of radars were considered for the present application: a high-power pulsed radar using a klystron or magnetron tube as a power source and a low-power FM-CW³ radar built with a solid-state transmitter. These basic radar configurations are shown in figure 3. A pulsed radar typically uses a single antenna for transmission and reception by using a t/r (transmit/receive) network. FM-CW radars are usually built using a pair of antennas to minimize leakage of the transmit signal into the receiver. For a pulsed radar, range resolution ΔR is equal to $c\tau/2$ where c is the speed of light and τ is the transmitted pulse length. For example, a range resolution of 2 km requires a pulse length of $13.33 \mu\text{s}$. For an FM-CW radar, $\Delta R = \frac{c}{2B}$, where B is the bandwidth of the frequency-modulated transmit signal.

³ Frequency modulated continuous wave

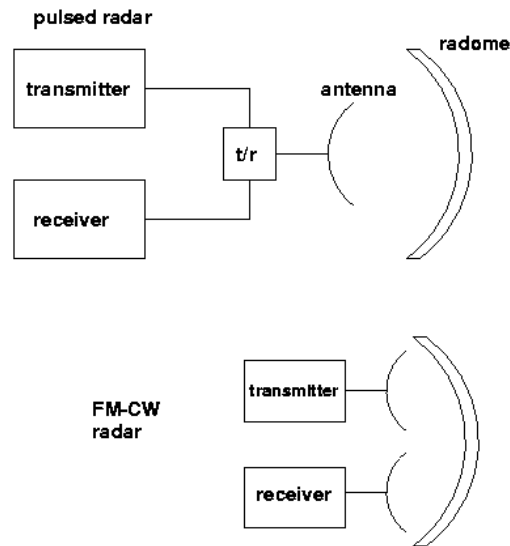


FIGURE 3. PULSED AND FM-CW RADAR CONFIGURATIONS

2.2 NEURAL NETWORK CLASSIFICATION OF PARTICLE PARAMETERS.

Neural networks have recently gained favor in solving complex, nonlinear problems where it is difficult to construct closed-form analytic solutions [Chen, 1996]. Quadrant used the Stuttgart Neural Network Simulator (SNNS), Version 4.1, running on a Silicon Graphics Workstation. The following description of neural networks is excerpted from the SNNS manual [Zell et al., 1995]:

Connectionism is a current focus of research in a number of disciplines, among them artificial intelligence (or more general computer science), physics, psychology, linguistics, biology, and medicine. Connectionism represents a special kind of information processing: Connectionist systems consist of many primitive cells (*units*) which are working in parallel and are connected via directed links (*links, connections*). The main processing principle of these cells is the distribution of activation patterns across the links similar to the basic mechanism of the human brain, where information processing is based on the transfer of activation from one group of neurons to others through synapses...

The high performance of the human brain in extremely complex cognitive tasks like visual and auditory pattern recognition was always a great motivation for modeling the brain. From this historic motivation, connectionist models are also called *neural nets*. However, most current neural network architectures do not try to closely imitate their biological model, but rather can be regarded simply as a class of parallel algorithms.

In these models, knowledge is usually distributed throughout the neural network and is stored in the structure of the topology and weights of the links. Neural networks are organized by (automated) training methods, which greatly simplify

the development of specific applications. Classical logic in ordinary artificial intelligence systems is replaced by vague conclusions and associative recall (exact match vs. best match). This is a big advantage in all situations where no clear set of logical rules can be given...

The inverse problem of extracting cloud parameters from the measured range profiles of backscattered power is a good example of a problem without well defined rules for estimation. The forward problem is straightforward: for a given drop-size distribution, reflectivity and attenuation can easily be calculated using Mie scattering formulas. Also, cloud and precipitation properties, such as liquid water content or rain rate, can be directly calculated from drop-size distribution. Solving the inverse problem, that is, calculating cloud parameters from measured reflectivity profiles, is very difficult due to the nonlinearity of the forward problem. Neural nets are ideal for solving problems where the forward problem is well characterized but the inverse is nonlinear and complicated.

The neural network was designed to extract cloud parameters using only measured power at multiple radar frequencies as a function of range.⁴ The basic concept is shown in figure 4 for a simulation using five range gates. From the range profiles of measured reflectivity, Z_m , the network estimates three cloud and precipitation properties, including liquid water content, m_v , mean volume diameter (MVD) and mean Z diameter (MZD). MVD and MZD were used in place of the more common ice sizing parameter of median volume diameter, since they are readily defined in terms of ratios of moments of the drop-size distribution. Mean volume diameter (particle diameter corresponding to the mean of the volume distribution) is defined as the fourth moment divided by the third moment of the drop-size distribution

$$MVD = \frac{\int_0^{\infty} p^4(r)dr}{\int_0^{\infty} p^3(r)dr} . \quad (2)$$

where $p(r)$ is the number of particles per cubic meter per meter drop radius.

Mean Z diameter (diameter corresponding to the mean of the distribution of the sixth power of the drop size) is defined as the seventh moment divided by the sixth moment of the drop-size distribution:

$$MZD = \frac{\int_0^{\infty} p^7(r)dr}{\int_0^{\infty} p^6(r)dr} . \quad (3)$$

⁴ A similar neural network-based algorithm, one that estimates snowfall amounts from radar reflectivity profiles, was recently published in [Xiao, et al. 1998].

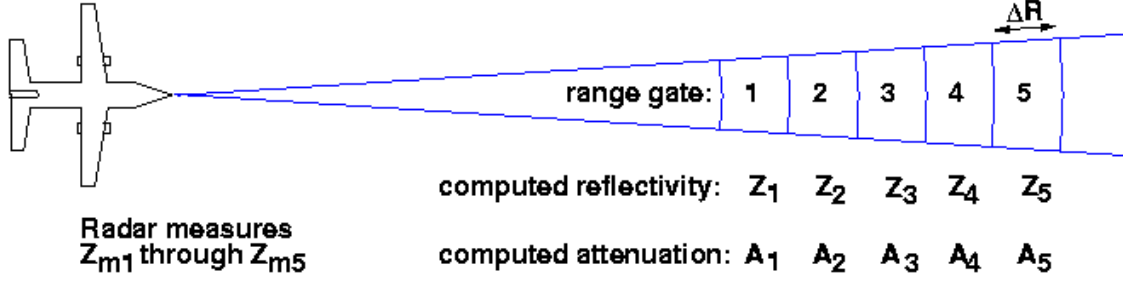


FIGURE 4. NEURAL NETWORK ESTIMATION OF CLOUD PARAMETERS IS DERIVED SOLELY FROM MEASURED PROFILES OF REFLECTIVITY, $Z_{m1} - Z_{m5}$ AT ONE, TWO, OR THREE FREQUENCIES
(Attenuation values are only used to compute the effect of attenuation on measured power.)

When the size distribution is narrow, MVD and MZD are almost equal. MZD is considerably larger than MVD for drop-size distributions with a wide range of particle sizes. We show below that MVD is close to median volume diameter for the modified gamma distribution.

Radar reflectivity data is calculated from drop-size distributions in each range cell, using Mie scattering for spherical particles by implementing an iterative procedure developed by Deirmendjian [Deirmendjian, 1969] [Ulaby et al., 1981]. Reflectivity and attenuation are calculated for each range cell at each operating frequency, then combined to obtain the radar observed reflectivity for each cell. At each frequency, the measured reflectivity (Z_{mN}) corresponding to the N-th cell is calculated from radar reflectivity of the N-th cell, in dB, (Z_N) and one-way attenuation due to propagation, in dB, (A_N) according to

$$Z_{mN} = Z_N - A_N \Delta R - \sum_{i=1}^{N-1} 2A_i \Delta R, \quad (4)$$

where A_i is the attenuation rate in dB/km corresponding to cell i . Our model uses five range cells with $\Delta R = 2$ km, so each set of training and test data contains five observed radar reflectivities at each operating frequency. Random measurement errors are accounted for by adding noise of 1 dB standard deviation to each value of Z_{mN} .

The neural networks used in this analysis consisted of an input layer, two hidden layers, and an output layer. Hidden layers consist of nodes that are not directly connected to input or output. The number of input (N_i) and output nodes (N_o) is determined by the number of radar operating frequencies (N_f), number of range gates (N_r), and number of cloud parameters (N_p) according to

$$N_i = N_f N_r \quad (5)$$

and

$$N_o = N_p * (N_r - 2). \quad (6)$$

Cloud and precipitation parameters of the first and last range cells are not estimated because the multifrequency technique relies on the reflectivity gradient (related to attenuation), which becomes less accurate if data from adjacent range gates are not available. The number of nodes in the hidden layers increases with the number of input nodes, allowing the neural network to implement a more complex algorithm as additional input data is available. Figure 5 shows the neural network topology for a single input frequency. The top row of inputs is equal to the measured reflectivity at five range gates. The bottom row corresponds to the estimated liquid water content, MVD, and MZD at the three central range gates. The diameter of the nodes in figure 5 indicates the strength of its output. These diameters change as a function of input, depending on the weights of the interconnecting lines and the node transfer function. The node connections were configured to implement a simple feed forward neural network, while standard backpropagation⁵ learning was employed to train the neural network. It was found that the largest neural network (three-frequency) could be accurately trained within a few hours on an SGI workstation. The neural network was originally trained using the total root mean square (rms) error between input and output data sets. However, this led the neural network to focus on the largest particles. Subsequently, we trained the neural network to minimize the percentage error, which gave more uniform results as a function of particle size and liquid water content.

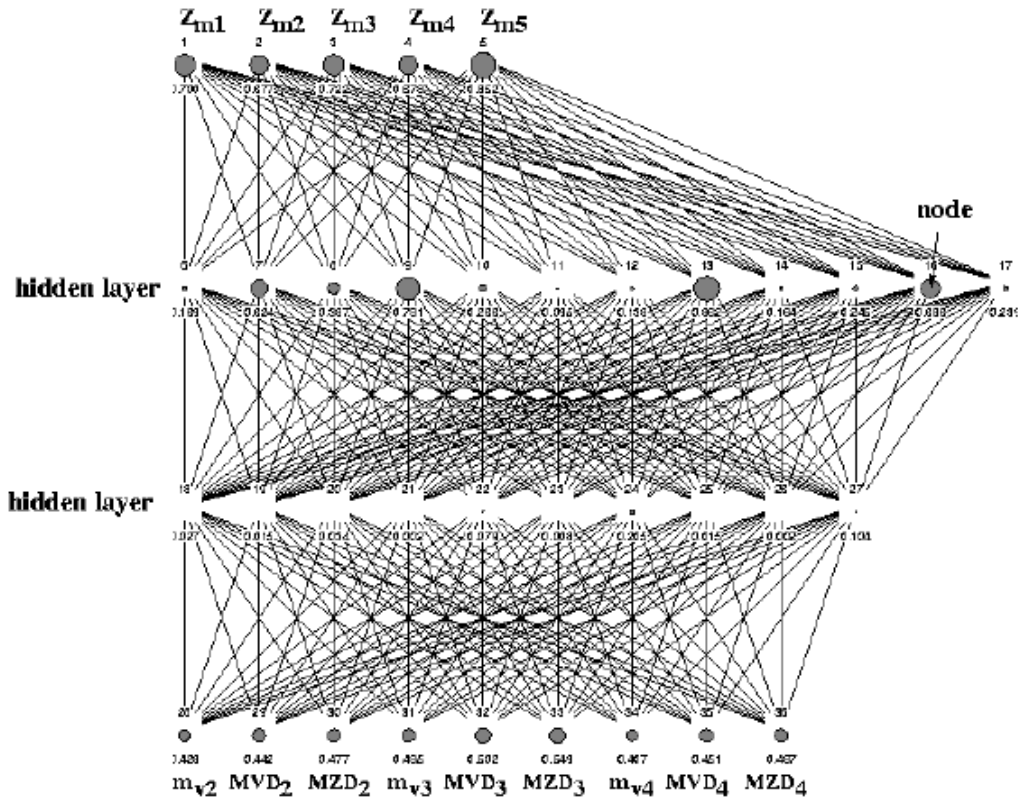


FIGURE 5. NETWORK TOPOLOGY FOR SINGLE INPUT FREQUENCY NEURAL NETWORK

⁵ Standard backpropagation seeks to minimize the global error between network output vectors and training output vectors [Rumelhart, et al. 1986].

2.2.1 Training and Test Data.

A flow chart of the simulation software is shown in figure 6. The bulk of the chart describes the procedure used to generate training and test data. This data, generated using the models presented below, turned out to be the most critical aspect of this analysis. These files contain a large number of input/output data vector pairs, each of which represents a particular cloud or precipitation case. The variety of cases, the relationships built between the various elements of the input and output vectors, and the errors of the radar data must be realistic and must represent nature to ensure that the results predict the performance capability of a real system. Unrealistic training and test data will produce unrealistic results.

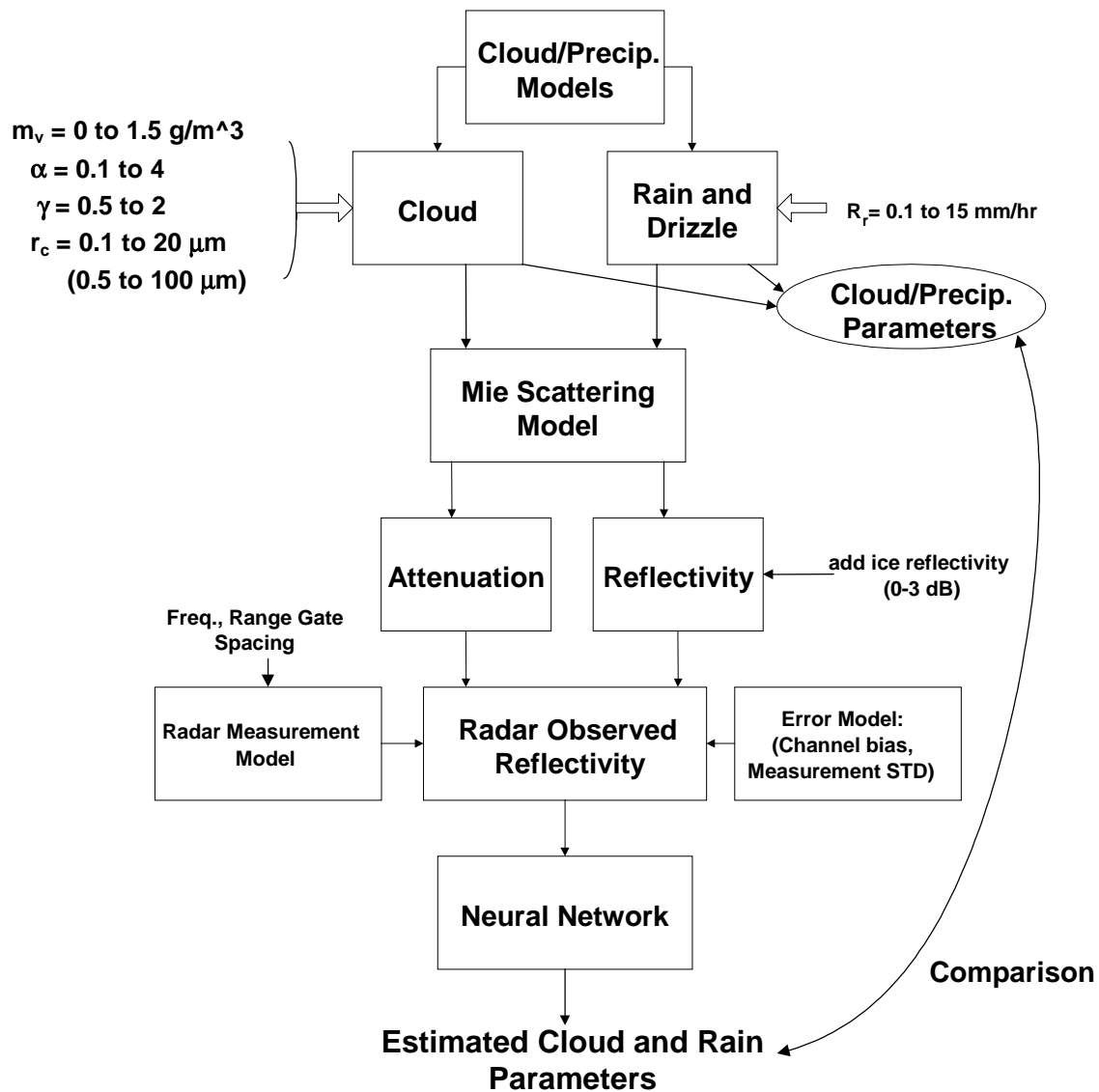


FIGURE 6. SIMULATION SOFTWARE FLOW CHART

Test data and training data sets were generated independently using the same statistical models. Training data files contain a much larger number of cases (10,000 training compared to 200 test cases), assuring coverage of the entire space of cloud and precipitation conditions. Another reason for training the neural network with a very large data set is to avoid under-sampling the input/output function and to prevent memorization,⁶ which can lead to large errors when an independent test data set is applied to the neural network. The test data files do not have to be large, but they should sample the range of conditions a real system might encounter.

2.2.2 Drop-Size Distributions.

Cloud drop-size distributions are commonly modeled using the modified gamma distribution [Deirmendjian, 1969]:

$$p(r) = ar^\alpha e^{-br^\gamma} m^{-4} \quad (7)$$

where a, α, b and γ are positive, real constants that can be used to parameterize drop-size distribution. These constants are related to the number of particles per cubic meter, N_v , and the mode radius, r_c , (the particle radius corresponding to the peak of the drop-size distribution) by the following formulas:

$$b = \frac{\alpha}{\gamma r_c^\gamma} \quad (8)$$

$$a = \frac{N_v \gamma b^\beta}{\Gamma(\beta)} \quad (9)$$

where $\Gamma()$ is the gamma function and

$$\beta = \frac{\alpha + 1}{\gamma}. \quad (10)$$

The cloud liquid water content is related to N_v and particle radius, r , in meters, by

$$m_v = 10^6 \sum_{i=1}^{N_v} \frac{4\pi}{3} r_i^3. \quad (11)$$

Thus, drop-size distribution is completely specified by liquid water content, mode radius, and shape parameters α and γ .

⁶ If the number of training points is small, the network can implement an error-free mapping of each set of input values into the proper output values.

The Marshall-Palmer distribution was used for the rain and drizzle cases tested below:

$$p(d) = N_0 e^{-bd} \quad (12)$$

where $N_0 = 8.0 \times 10^6$ for rain, $N_0 = 8.0 \times 10^6$ for drizzle, and d is the drop diameter in meters. The parameter, b , is given by

$$b = 4100R_r^{-0.21} \quad (\text{for rain}) \quad (13)$$

$$b = 5700R_r^{-0.21} \quad (\text{for drizzle}) \quad (14)$$

where R_r is the rain rate in mm/hr.

Mean volume diameter and mean Z diameter were calculated from drop-size distributions which, together with liquid water content, served as output vector elements of the training and test data sets. The difference between MVD and MZD is a measure of the spread in particle size distribution. A narrow distribution of particles will exhibit nearly equal values of MVD and MZD, while a broad distribution of particle sizes will have a larger value of MZD than MVD. Figure 7 displays a typical gamma distribution, $p_d(d)$ ($\alpha = 1.0$, $\gamma = 0.5$), and associated volume distribution, $p_v(d) = d^3 p_d(d)$, and reflectivity distribution, $p_z(d) = d^6 p_d(d)$. Also shown are MVD, MZD, and median volume diameter (MeVD). For the range of gamma distributions used in the simulations, the ratio MZD/MVD ranged from 1.27 (for narrow distribution) to 2.91 (for wide distribution). The ratio MeVD/MVD varied from 0.78 to 0.99.

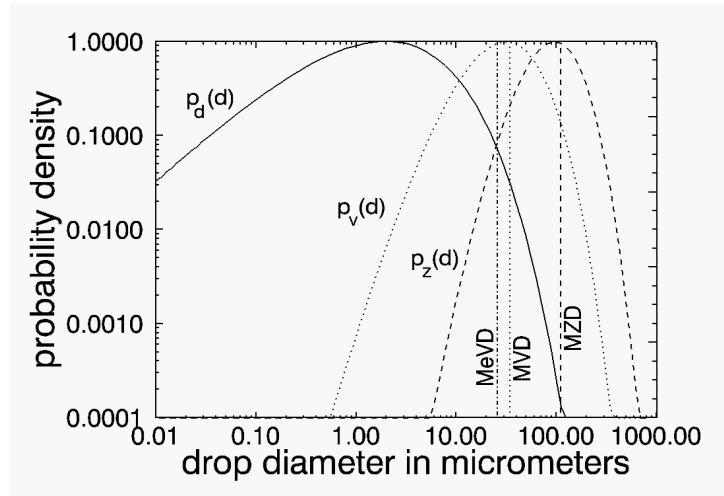


FIGURE 7. TYPICAL PARTICLE DIAMETER DISTRIBUTION, $p_d(d)$, ASSOCIATED VOLUME DISTRIBUTION, $p_v(d)$, AND REFLECTIVITY DISTRIBUTION, $p_z(d)$ (The dashed lines show MVD, MZD, and median volume diameter (MeVD)).

Extreme examples of cloud distributions are shown in figure 8 for the smallest and largest mode radius. Extreme examples of drizzle and rain distributions are shown in figures 9 and 10 for both smallest and largest rain rates.

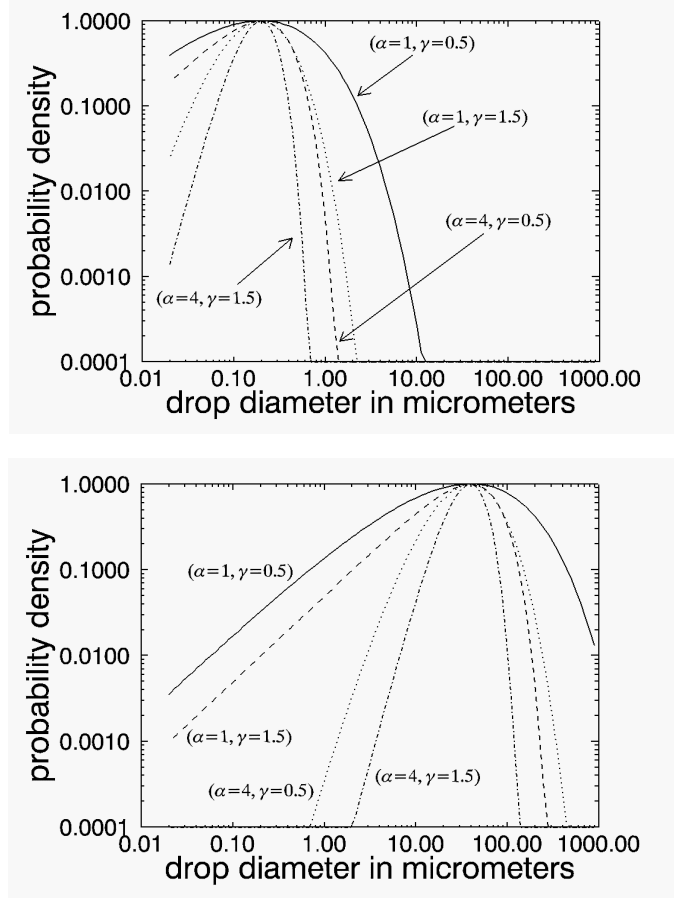


FIGURE 8. RANGE OF DISTRIBUTION SHAPES FOR SMALLEST MODE RADIUS (Top, $r_c = 0.1 \mu\text{m}$) and largest mode radius (bottom, $r_c = 20 \mu\text{m}$)

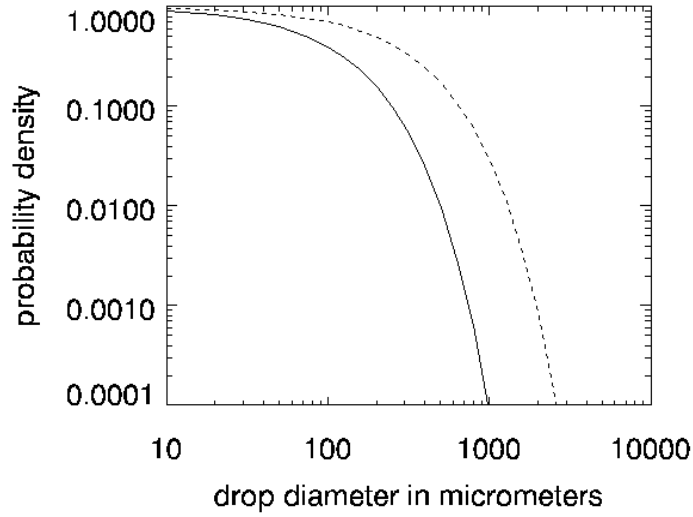


FIGURE 9. RANGE OF DISTRIBUTION SHAPES FOR DRIZZLE (Solid line: $R_r = 0.1 \text{ mm/hr}$; dotted line: $R_r = 10 \text{ mm/hr}$)

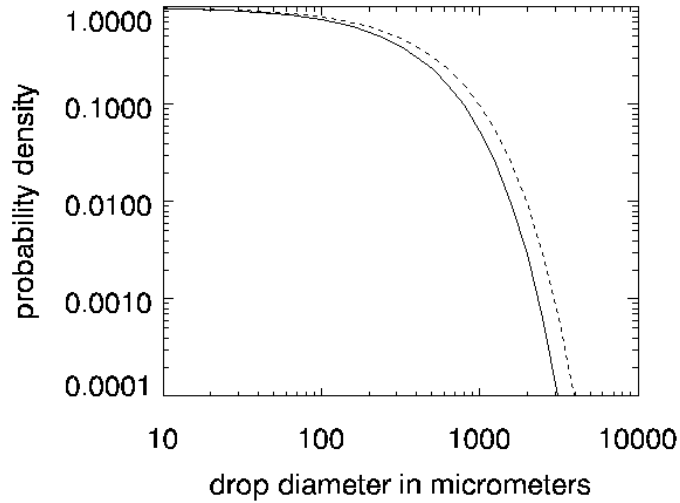


FIGURE 10. RANGE OF DISTRIBUTION SHAPES FOR RAIN
(Solid line: $R_r = 5$ mm/hr; dotted line: $R_r = 15$ mm/hr)

2.2.3 Inversion of Particle Parameters With Randomly Varying Conditions.

The first test of the inversion algorithm includes a random mixture of clouds and precipitation. Conditions were varied randomly from range-cell to range-cell with no correlation between adjacent cells. These rapidly changing, uncorrelated conditions from cell to cell make estimation difficult because reflectivity gradients are not only a function of attenuation, but can quickly change due to variations in drop size and number of drops contained in the range-cell. The test and training data contained 75% cloud cases, 15% drizzle, and 10% rain.

Model parameters used for cloud, drizzle, and rain are tabulated below. Unless noted, parameters are uniformly distributed over the given range. Temperature fluctuations were included (from -15 to $+5^\circ\text{C}$) since the index of refraction of water is temperature dependent. The algorithm uses temperature in computing the index of refraction of water, which affects scattering efficiency and attenuation.

- Cloud model (based on gamma distribution) (75% of all cases):

Mode Radius: 0.1 to $20\ \mu\text{m}$
 Shape Parameter α : 1 to 4
 Shape Parameter γ : 0.5 to 1.5
 Liquid Water Content m_v : 0.05 to $1.5\ \text{g}\cdot\text{m}^{-3}$

- Drizzle (Marshall-Palmer distribution) (15% of all cases):

Rain Rate R_r : 0.1 to $10\ \text{mm/hr}$

- Rain (Marshall-Palmer distribution) (10% of all cases):

Rain Rate R_r : 5 to $15\ \text{mm/hr}$

Three neural networks were trained and tested with simulated data. Figure 11 shows the liquid water content and MVD versus reflectivity distribution of the training and test data sets, including a mixture of clouds, rain, and drizzle. The highly clustered tail at the upper end of the dBZ versus MVD plot (see the left-hand plots in figure 11) corresponds to the rain and drizzle cases only. Clustering in the rain and drizzle cases is due to the fact that there is a one-to-one correspondence between reflectivity and mean volume diameter for the Marshall-Palmer distribution. Clustering due to the Marshall-Palmer distribution can also be seen in the plots of dBZ versus liquid water content (see the right-hand plots in figure 11).

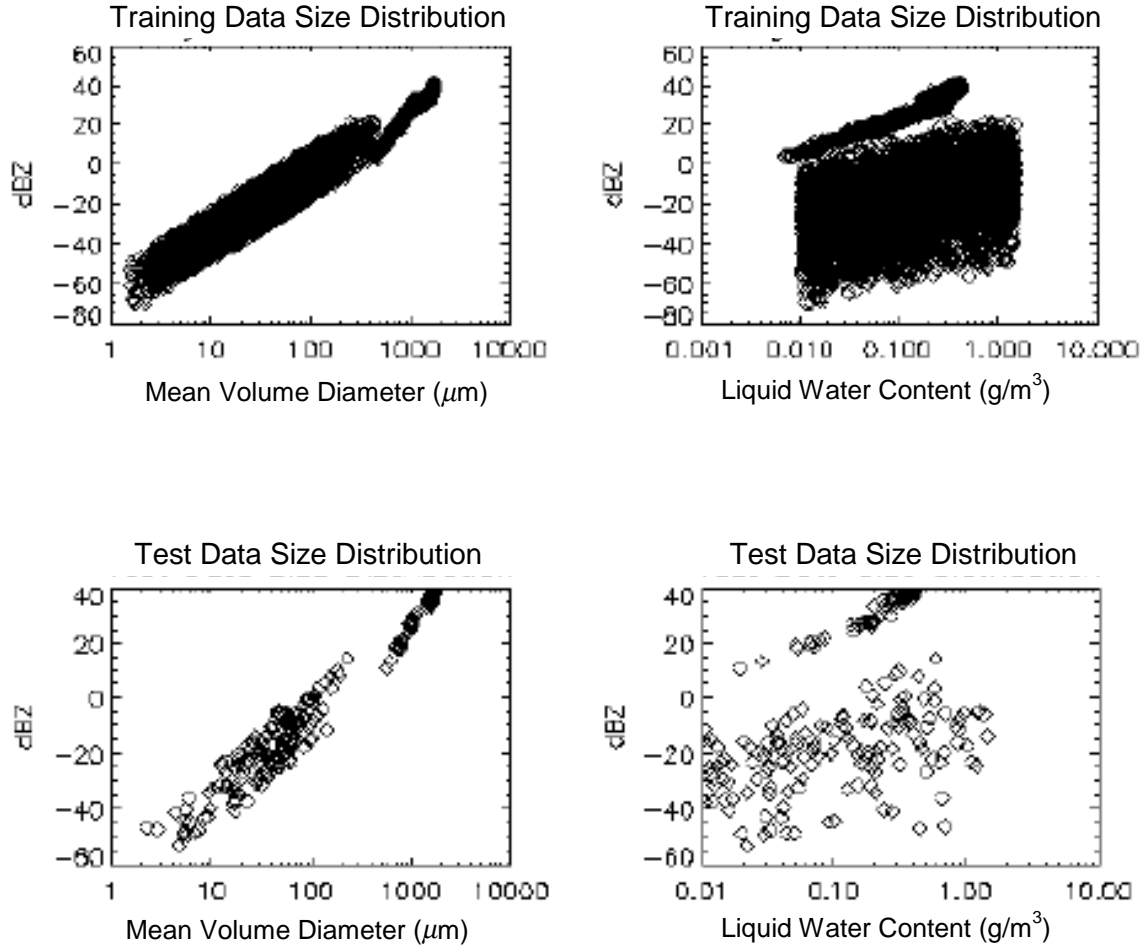


FIGURE 11. SCATTER PLOT OF dBZ VERSUS MVD AND LIQUID WATER CONTENT FOR THE TRAINING DATA SET AND TEST DATA SET (Drizzle and rain (25% of cases) were generated using the Marshall-Palmer distribution; Clouds (75% of cases) are gamma distributed.)

The neural networks included one trained for X-band only (10 GHz); one for X-band and Ka-band (10 and 35 GHz); and one trained for X-band, Ka-band, and W-band (10, 35, and 95 GHz). The effectiveness of these algorithms was evaluated by generating scatter plots of the true value of various parameters for the test data set versus the neural network estimates of these parameters.

Results for the case of mixed precipitation and clouds is presented in figure 12. Root mean square (rms) errors are tabulated along with scatter plots of estimated versus input values of liquid water content, MVD, and MZD. Liquid water content errors were reported using an absolute scale, since the effect of liquid water on aircraft icing is linearly related to liquid water content. A percent scale was used to display MVD and MZD errors, emphasizing that sizing accuracy was almost constant over a wide range of input sizes. Using an absolute scale for particle size errors is misleading, since the absolute error is dominated by small percentage errors in the largest particles.

The results presented in figure 12 show that estimation accuracy improves substantially for liquid water content as more operating frequencies are used. On the other hand, sizing is fairly robust, even using a single 10 GHz radar. This is because reflectivity is most strongly dependent on particle size (MZD) and only secondarily on liquid water content, since Z is proportional to d^6 while m_v is proportional to d^3 .

2.2.4 Simulation of Stratus Layer.

To simulate flight through a stratus layer, the neural network was also trained with a model that only contained clouds. In order to simulate a slowly varying cloud deck, adjacent range cells were correlated with two different correlation factors. The range of cloud parameters used for the stratus simulation are (Stratus Clouds 100% of all cases):

Mode Radius: 0.1 to 20 μm
Shape Parameter α : 1 to 4
Shape Parameter γ : 0.5 to 1.5
Liquid Water Content m_v : 0.01 to 1.5 $\text{g}\cdot\text{m}^{-3}$
Temperature: -15 to +5°C.

For the previous simulation, liquid water content was uniformly distributed between 0.05 to 1.5 $\text{g}\cdot\text{m}^{-3}$. This resulted in a low probability of generating clouds with low liquid water content (only 3.3 percent of the cases were less than 0.1 $\text{g}\cdot\text{m}^{-3}$). For stratus clouds, liquid water content was distributed log-uniformly between 0.05 and 1.5 $\text{g}\cdot\text{m}^{-3}$, emphasizing cases with smaller liquid water content

$$m_v = 0.5 \times 10^{1.47U[0-1]}(m) \quad (15)$$

where $U[0-1]$ is a uniformly distributed random variable on the interval $[0,1]$. In this way, the probability of simulating clouds with liquid water content below 0.1 $\text{g}\cdot\text{m}^{-3}$ was increased from 3.3 percent to 20 percent of all cases.

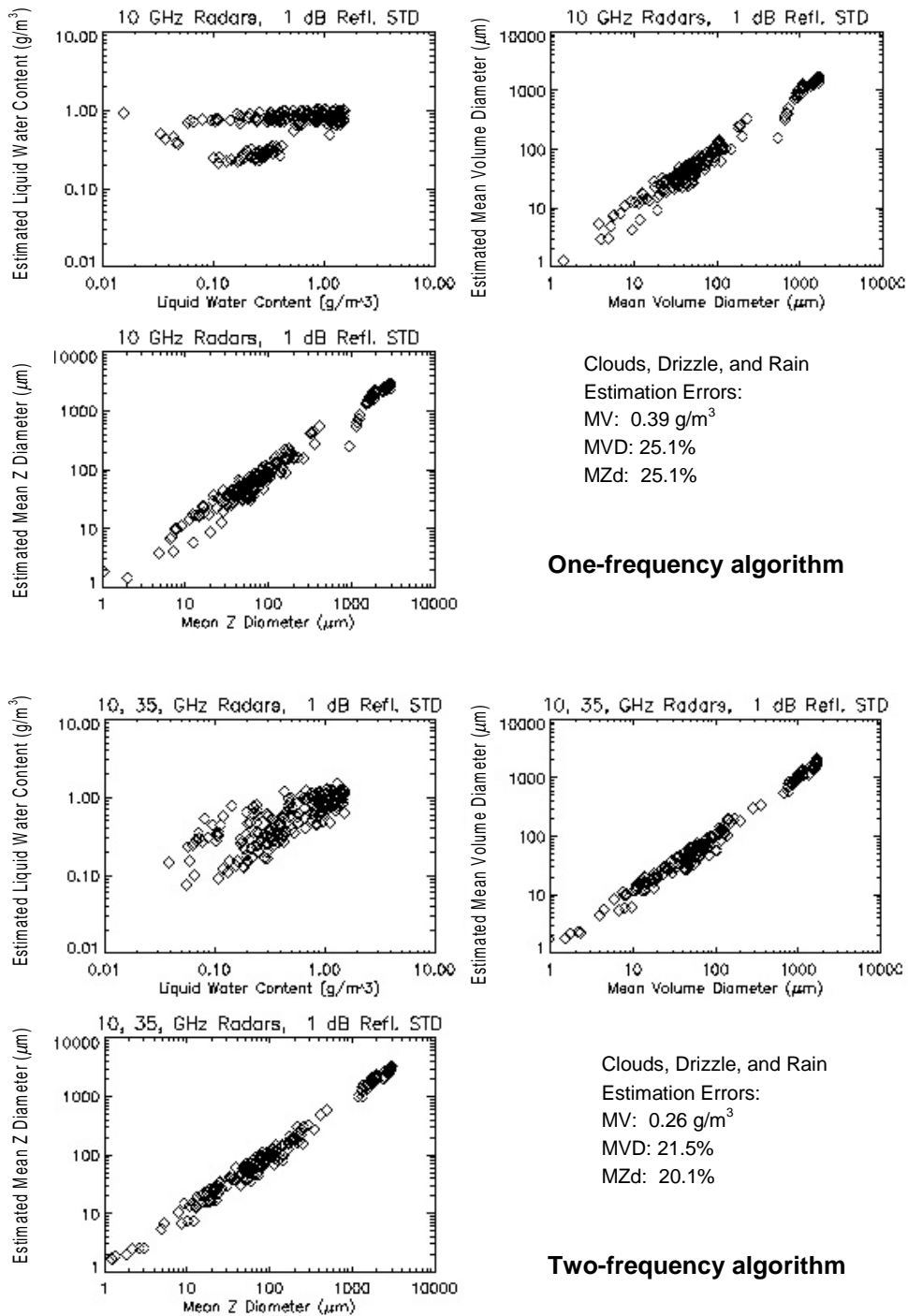


FIGURE 12. SCATTER PLOTS OF ESTIMATED VERSUS INPUT LIQUID WATER CONTENT, MVD, AND MZD FOR TOTALLY RANDOM PROFILE OF CLOUD AND PRECIPITATION CONDITIONS USING ONE FREQUENCY, TWO FREQUENCIES, AND THREE FREQUENCIES (Drizzle and rain (25% of cases) were generated using the Marshall-Palmer distribution; clouds (75% of cases) are gamma distributed.)

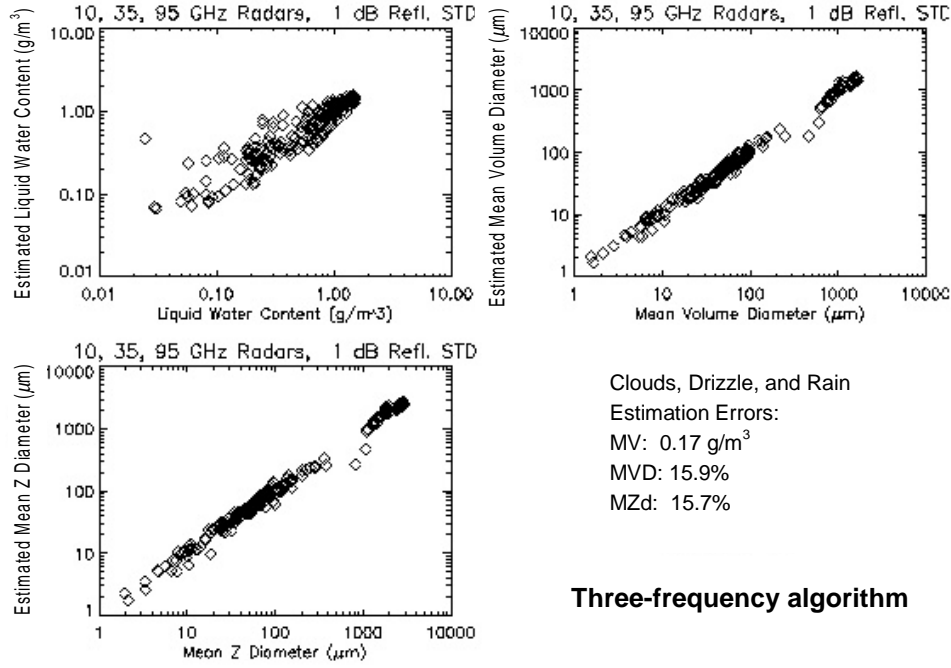


FIGURE12. SCATTER PLOTS OF ESTIMATED VERSUS INPUT LIQUID WATER CONTENT, MVD, AND MZD FOR TOTALLY RANDOM PROFILE OF CLOUD AND PRECIPITATION CONDITIONS USING ONE FREQUENCY, TWO FREQUENCIES, AND THREE FREQUENCIES (Continued)

Mode radius, shape parameters, liquid water content, and temperature were correlated from range gate to range gate within a particular case, but each case (10000 for training and 200 for testing) was independent from the rest. This correlation was generated by the following mixing formula (shown for m_v)

$$m_v(i+1) = m_v(i) * C + \tilde{m}_v * (1 - C) \quad (16)$$

where \tilde{m}_v is a randomly generated value within the allowable range, and C is the correlation factor. Two test cases for $C = 0.9$ and 0.7 are presented below.

Data from stratus simulations are presented in figures 13 and 14. These cases show improved ability to detect liquid water content using two and three frequencies as compared to the totally random case.

2.2.5 Modified Gamma Distribution Used to Represent All Clouds, Rain, and Drizzle.

The Marshall-Palmer drop-size distribution used in the rain simulations described above results in a fixed relationship between Z and R_r

$$Z = 200R_r^{1.6} \quad (17)$$

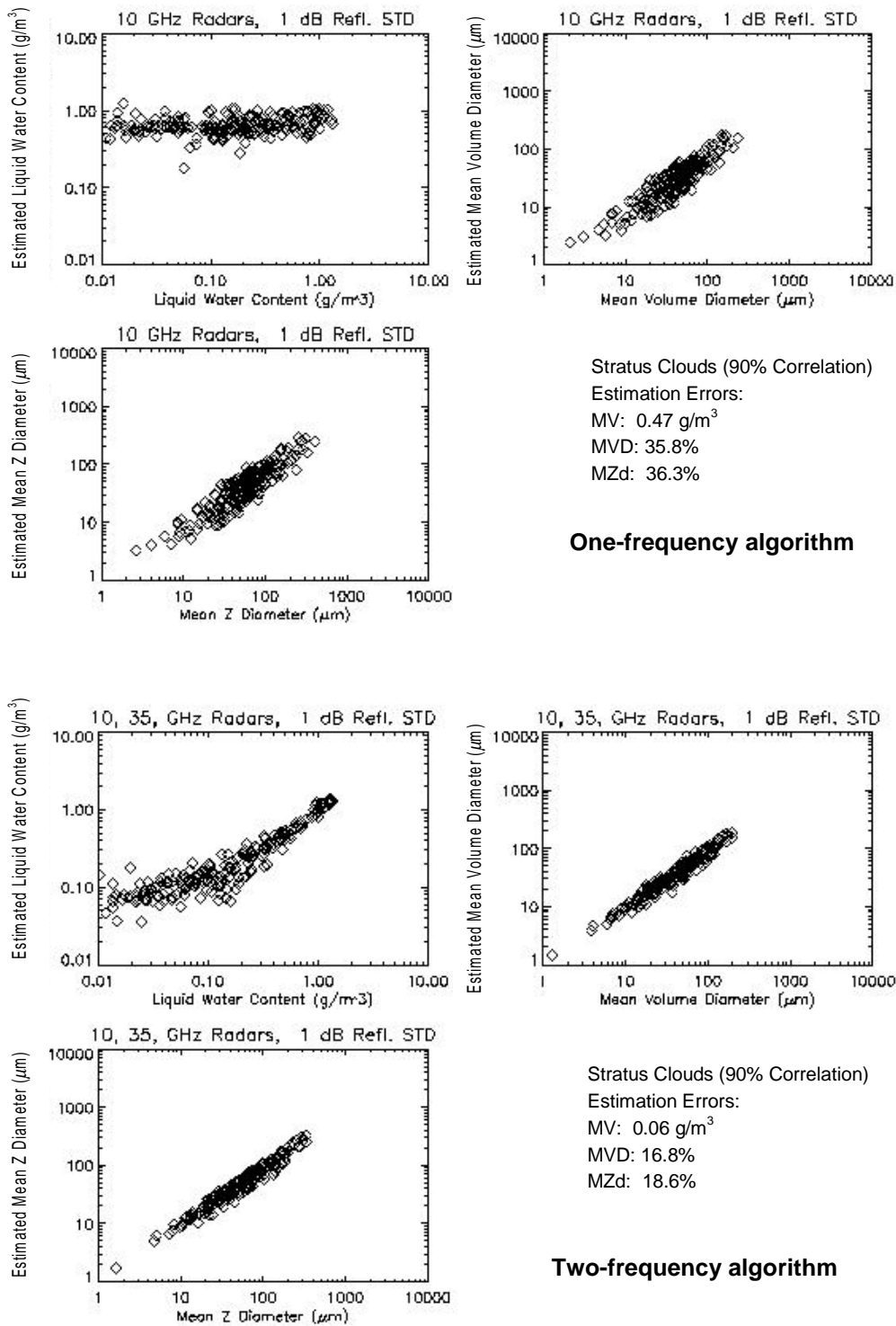


FIGURE 13. SCATTER PLOTS OF ESTIMATED VERSUS INPUT LIQUID WATER CONTENT, MVD, AND MZD FOR STRATUS LAYER WITH 90 PERCENT PROFILE-TO-PROFILE OVERLAP OF CLOUD CONDITIONS USING ONE FREQUENCY, TWO FREQUENCIES, AND THREE FREQUENCIES (All data were generated using the modified gamma distribution.)

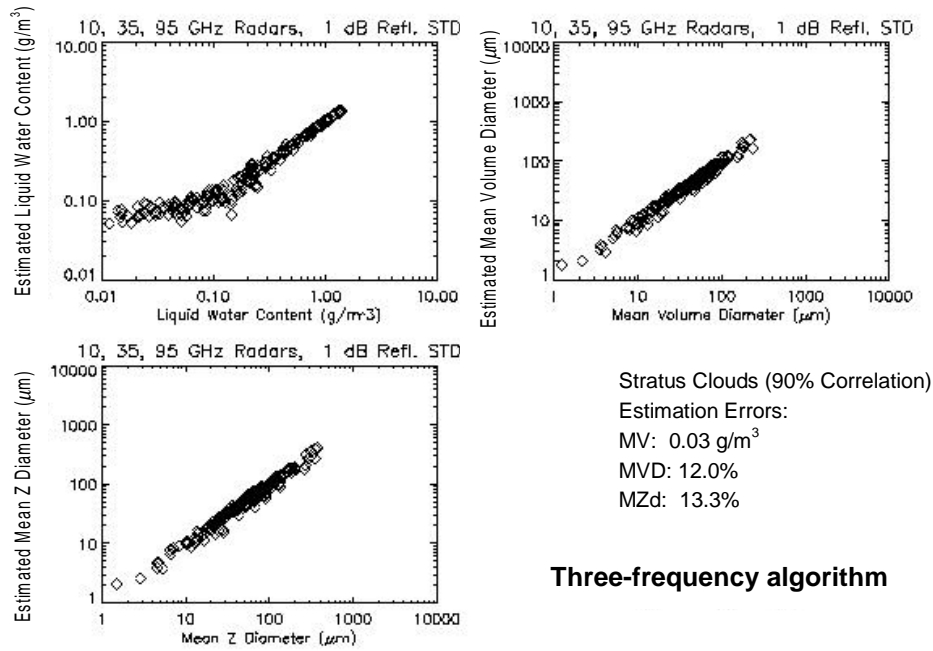


FIGURE 13. SCATTER PLOTS OF ESTIMATED VERSUS INPUT LIQUID WATER CONTENT, MVD, AND MZD FOR STRATUS LAYER WITH 90 PERCENT PROFILE-TO-PROFILE OVERLAP OF CLOUD CONDITIONS USING ONE FREQUENCY, TWO FREQUENCIES, AND THREE FREQUENCIES (Continued)

referred to as the Marshall-Palmer formula [Doviak and Zrníc, 1993]. When the neural network is trained with a Marshall-Palmer distribution for rain, measurements of Z made at X-band (a nearly nonattenuating wavelength) are equivalent to nearly exact measurements of rain rate⁷. Once the rain rate is known, the entire particle size distribution is determined through equations 12 and 13. Therefore, once Z is measured at X-band, all cloud properties are pinned down deterministically. To avoid this problem, the modified gamma distribution was used to model precipitation. The modified gamma distribution has no fixed relationship between Z and particle size distribution, making it more difficult for the algorithm to invert particle parameters from radar measurements. The following range of parameters was used to model clouds, drizzle, and rain. Modified gamma distribution model for clouds, drizzle, and rain:

Mode Radius: 0.5 to $160 \mu\text{m}$
 Shape Parameter α : 0.1 to 4.1
 Shape Parameter γ : 0.5 to 2.0
 Liquid Water Content m_v : 0.001 to $1.5 \text{ g}\cdot\text{m}^{-3}$
 Temperature: -15 to $+5^\circ \text{C}$.

⁷ Errors still arise in the inversion due to added noise in the X-band test data.

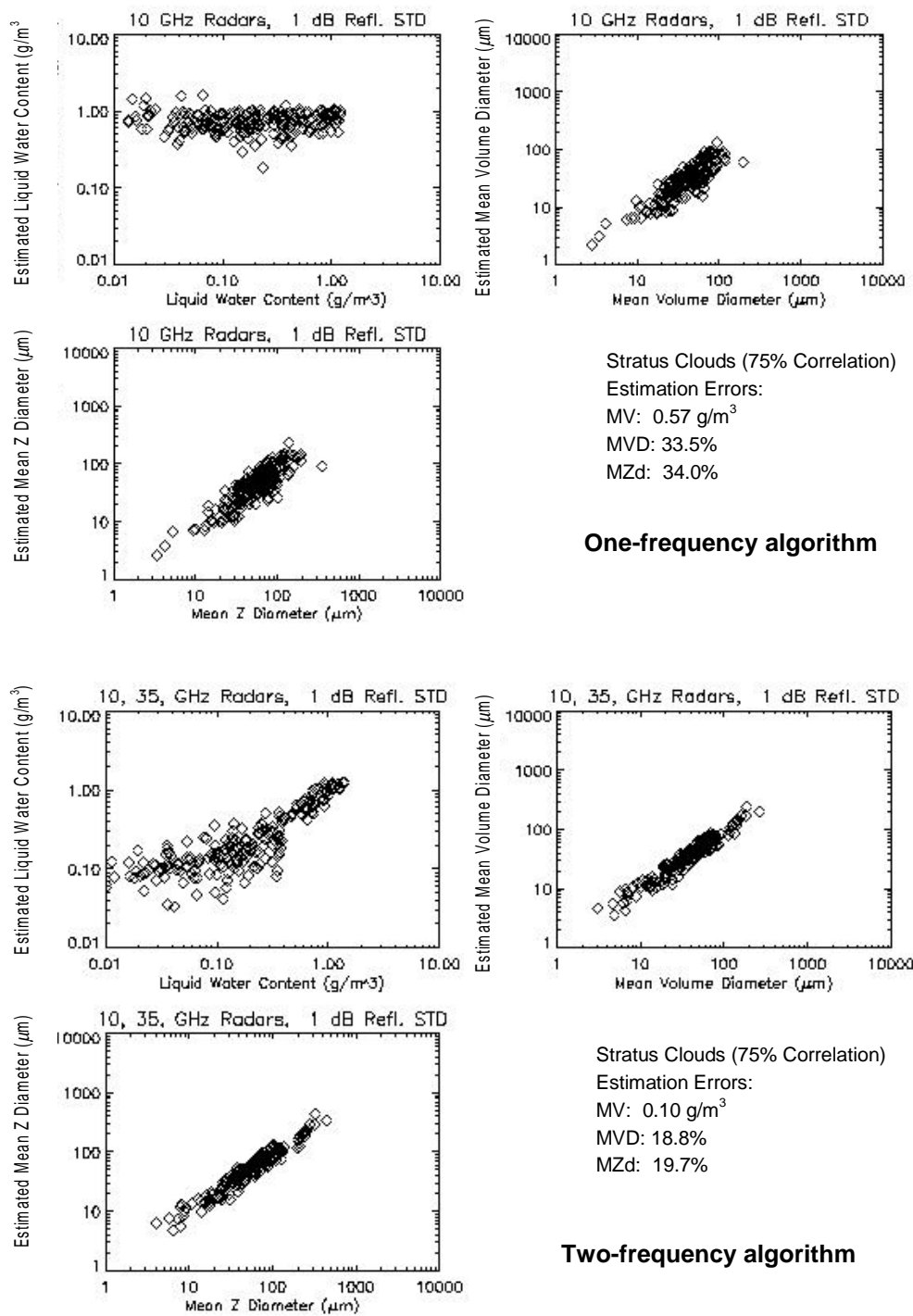


FIGURE 14. SCATTER PLOTS OF ESTIMATED VERSUS INPUT LIQUID WATER CONTENT, MVD, AND MZD FOR STRATUS LAYER WITH 75 PERCENT PROFILE-TO-PROFILE OVERLAP OF CLOUD CONDITIONS USING ONE FREQUENCY, TWO FREQUENCIES, AND THREE FREQUENCIES (All data were generated using the modified gamma distribution.)

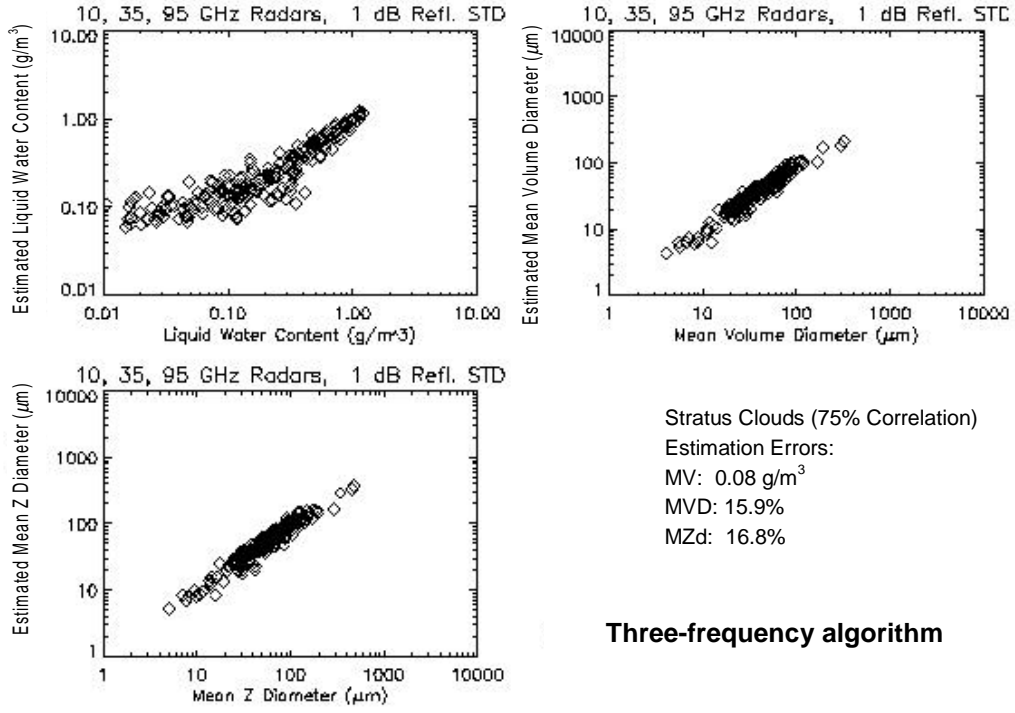


FIGURE 14. SCATTER PLOTS OF ESTIMATED VERSUS INPUT LIQUID WATER CONTENT, MVD, AND MZD FOR STRATUS LAYER WITH 75 PERCENT PROFILE-TO-PROFILE OVERLAP OF CLOUD CONDITIONS USING ONE FREQUENCY, TWO FREQUENCIES, AND THREE FREQUENCIES (Continued)

To avoid assigning high liquid water contents to distributions containing very large droplets, the liquid water content was coupled to the mode radius using the following distribution function:

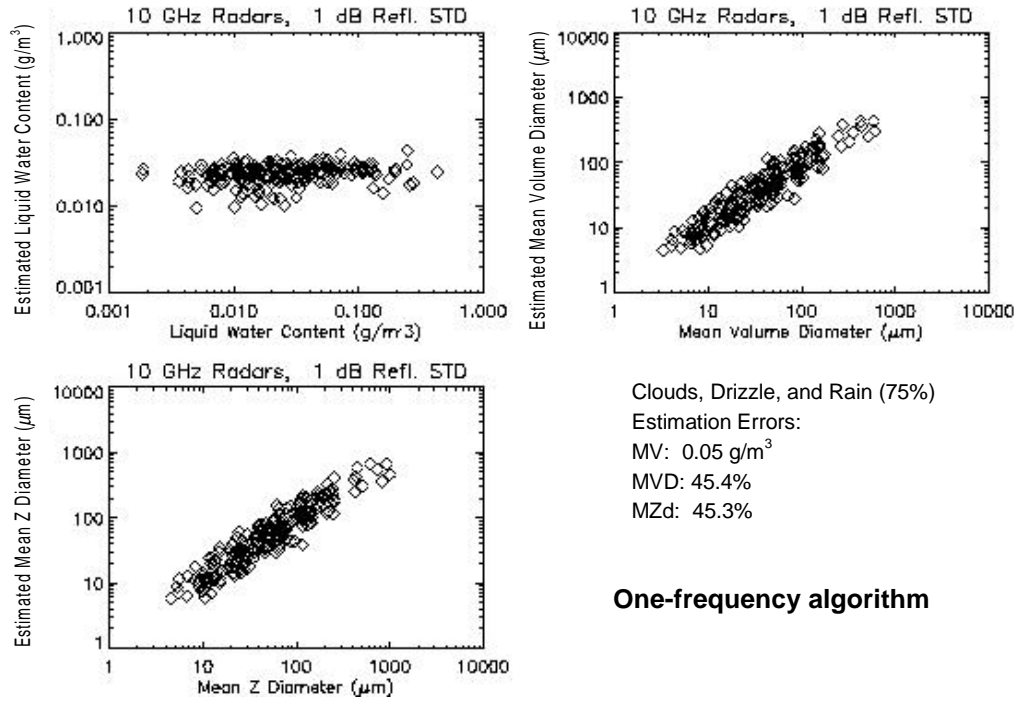
$$m_v = 0.001 \times 10^{U[0-1](3.176-1.3)\sqrt{\frac{r_c}{10^{-4}}}} g \cdot m^{-3} \quad (18)$$

The mode radius was also distributed using a log-uniform distribution to give a higher probability of small droplets:

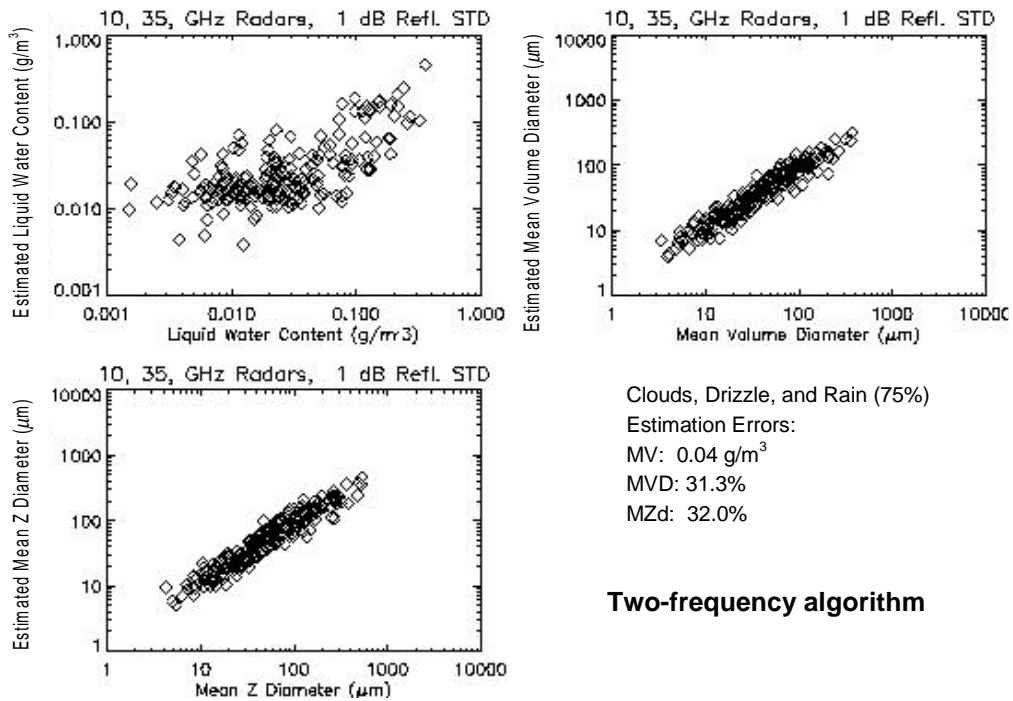
$$r_c = .5 \times 10^{-6} 10^{2.5U[0-1]} (m). \quad (19)$$

2.2.6 Summary of Multifrequency Inversion Study.

Figure 15 plots liquid water content, MVD, and MZD inversions using one-, two-, and three-frequency neural networks for the cloud, drizzle, and rain case with modified gamma distributed particle sizes. Like the second stratus case presented above, the correlation between gates was 75 percent. Note that the average error in liquid water content is greatly reduced for the single-frequency case. This is an artifact of the training process, where liquid water content was intentionally biased towards smaller values than in the previous test cases.



One-frequency algorithm



Two-frequency algorithm

FIGURE 15. RESULTS FOR CLOUD, DRIZZLE, AND RAIN MODEL USING MODIFIED GAMMA DISTRIBUTIONS USING ONE FREQUENCY, TWO FREQUENCIES, AND THREE FREQUENCIES

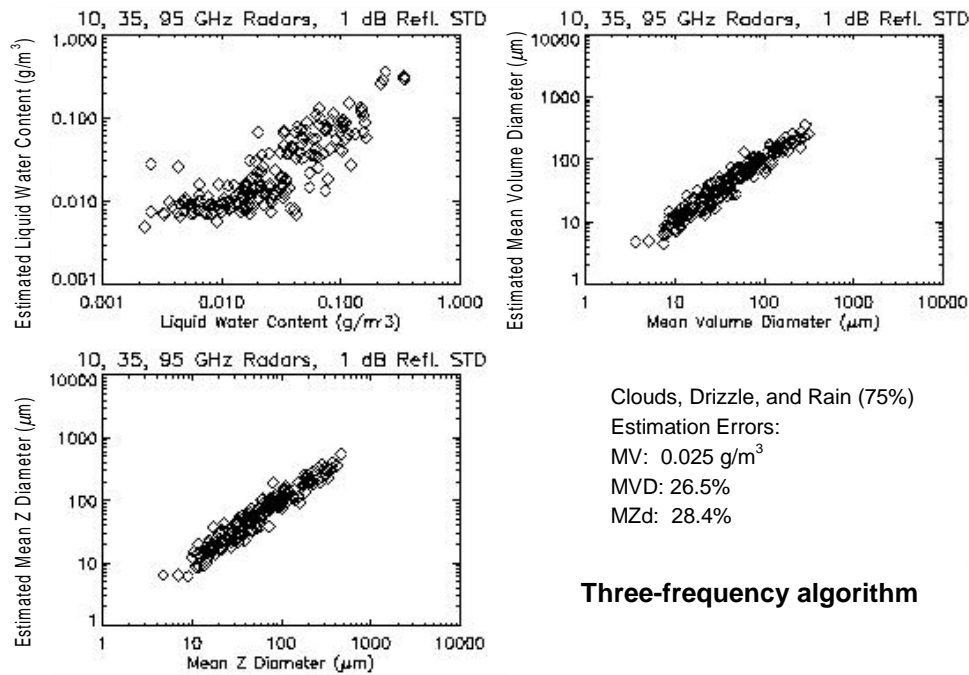


FIGURE 15. RESULTS FOR CLOUD, DRIZZLE, AND RAIN MODEL USING MODIFIED GAMMA DISTRIBUTIONS USING ONE FREQUENCY, TWO FREQUENCIES, AND THREE FREQUENCIES (Continued)

Table 1 summarizes errors in liquid water content, MVD, and MZD for one-, two-, and three-frequency estimates for the case of random cloud variation, the two stratus layer cases, and the simulation based solely on the modified gamma distribution. These results suggest that a two- or three-frequency radar system can be used to extract particle size and liquid water content from measured values of backscattered power. For all four test cases, the three-frequency inversion errors are smaller than the two-frequency inversion by as much as 100 percent, although the improvement is not as dramatic as between the one- and two-frequency cases.

Following the program review at CRREL, the neural network was retrained separately for each individual parameter. Training each parameter separately made a small improvement in performance for MVD and MZD and no improvement for liquid water content. The neural network was also trained to extract *median* volume diameter. The error reported for median volume diameter was within 1 percent of the error reported for mean volume diameter, when tested on a three-frequency inversion.

2.3 POLARIMETRIC RADAR.

For the most general case of scattering from natural surfaces, a polarimetric radar can report as many as nine independent parameters to represent the average scattering behavior of a collection of particles [Huynen, 1970]. For scatterers having azimuthal symmetry, the number of independent parameters is reduced to five. For a linearly polarized radar, these parameters

include reflectivity at vertical polarization, Z_v ; differential reflectivity, Z_{dr} ; linear depolarization ratio, LDR ; and magnitude and phase of the copolarized correlation coefficient, $|\rho_{hv}|$ and $\angle\rho_{hv}$.

TABLE 1. SUMMARY OF ESTIMATION ERRORS FOR ONE-, TWO-, AND THREE-FREQUENCY RADAR ESTIMATES OF LIQUID WATER CONTENT, MVD, AND MZD

Liquid Water Content Error, $\text{g}\cdot\text{m}^{-3}$			
Test Case	Frequency		
	10 GHz	35 GHz	95 GHz
Randomly varying clouds and rain	0.39	0.26	0.17
Stratus, 75% correlation	0.57	0.1	0.08
Stratus, 90% correlation	0.47	0.06	0.03
Modified gamma distribution, 75% correlation	0.05	0.04	0.02
MVD Error, %			
Test Case	Frequency		
	10 GHz	35 GHz	95 GHz
Randomly varying clouds and rain	25.1	21.5	15.9
Stratus, 75% correlation	33.5	18.8	15.9
Stratus, 90% correlation	35.8	16.8	12.0
Modified gamma distribution, 75% correlation	46.4	31.3	28.5
MZD Error, %			
Test Case	Frequency		
	10 GHz	35 GHz	95 GHz
Randomly varying clouds and rain	25.1	20.1	15.7
Stratus, 75% correlation	34.0	18.8	16.8
Stratus, 90% correlation	36.3	18.6	13.3
Modified gamma distribution, 75% correlation	45.3	32.0	28.4

Similar parameters are available for a circularly polarized radar and have been shown to contain equivalent information [Jameson, 1987]. The parameters can be reported at one or more frequencies, thus, an N_f frequency polarimetric radar can report as many as $5N_f$ polarimetric parameters. In practice, many of these parameters are correlated or partially correlated to one another, reducing the effective number of independent polarimetric parameters below $5N_f$. Conditions where the number of polarimetric parameters is less than five include

- Clouds with particles that are isotropic in the polarization plane. For this case, the number of independent scattering parameters is reduced from five to two. These two include Z_{vv} and Z_{vh} .
- Clouds with particles that are nearly spherical and dominated by single scattering. In this case, $LDR = 0$ and $Z_v = Z_h$, so the number of independent scattering parameters is reduced from five to one.

Thus, a polarimetric radar adds no additional detection capability as compared to a conventional weather radar when observing nonprecipitating clouds that only contain supercooled liquid water droplets. The primary advantage of a polarimetric radar is in detecting particles with a nonzero

axial ratio. Common particle shapes that can be detected over a horizontal or near horizontal path using polarimetric radar are listed below along with the applicable polarimetric quantities:

- Precipitation sized liquid droplets (Z_{dr} , $\angle\rho_{hv}$)
- Pristine ice crystals, such as plates or needles with preferred orientation (Z_{dr} , LDR , or ρ_{hv} .)
- Tumbling ice crystals without preferred alignment (LDR , $|\rho_{hv}|$).
- Hail (Z_{dr} , LDR , or ρ_{hv}).
- Water coated aggregates or rimed particles, especially in the melting band (LDR or $|\rho_{hv}|$).

Aggregates and rimed ice particles in the frozen state exhibit a small amount of depolarization (LDR values of -15 dB or less) and are usually difficult to detect on the basis of polarization alone.

Two other factors reduce the number of useful polarimetric parameters. First, polarimetric terms such as LDR and Z_{dr} are not strongly frequency dependent. For this reason, a practical multifrequency radar would most likely employ a single X-band polarimetric channel. Second, LDR measurements, exhibiting usable values 5 to 25 dB below the copolarized return, are not practical for a system that must operate at long ranges. Practical LDR measurements require high signal-to-noise ratios that can only be expected within a few kilometers of the aircraft. The only polarimetric parameters that are practical for long range measurements are Z_{dr} and ρ_{hv} , parameters that only depend on copolarized measurements.

Z_{dr} and ρ_{hv} measurements could aid the neural network inversion by identifying the presence of ice in mixed phase clouds. Ice biases reflectivity measurements without adding appreciably to attenuation. This bias appears as a change in drop size, which causes errors in the inversion of liquid water and size parameters. It is important to point out that regions exhibiting high levels of Z_{dr} are not all that common in nonprecipitating clouds other than cirrus. Such clouds must include pristine crystals in the absence of aggregates or other large particles that will dominate the backscattered power. A mixed-phase cloud containing aggregates would not be detectable by a polarimetric radar.

In summary, multiparameter radar can provide as many as $7N_f$ independent parameters (five polarimetric and two Doppler parameters per frequency). However, for the present application, where an N_f frequency radar would likely include no Doppler capability and only a single polarimetric channel, the total number of parameters is reduced to $4 + N_f$. In addition, for the case of liquid clouds containing small, nonprecipitation sized particles, the polarimetric channel adds no information, in which case the number of parameters is reduced to N_f , the backscattered power sampled at each frequency.

For research purposes, it is recommended that the X-band radar include a polarimetric channel to improve particle sizing of large droplets and identify pristine ice crystals when they occur. Adding a single-frequency polarimetric capability means adding an additional polarization port to the antenna feed and requires that the antenna be more carefully constructed to reduce coupling between orthogonal polarizations. A polarimetric channel also requires some additional switching circuitry for polarization agility and additional algorithm complication for calibration. Adding a single-frequency polarimetric channel to the radar will add approximately 5 percent to the total cost of the prototype system.

2.4 SCANNING STRATEGY.

For optimal sensitivity, a multifrequency radar will generate antenna patterns with differing beamwidths. Therefore, at any given instant, the low-frequency radar samples a much larger volume than the higher frequency systems. The scanning strategy described below can be used to mitigate this problem. In addition, any radar system sampling a distributed scatterer must average many pulses to converge to a usable estimate of the mean scattered power. The number of averages expected as a function of scan rate, maximum range, and size of the scan sector is derived below and is used subsequently to estimate signal-to-noise ratio.

A cross section of the scan volume is shown in figure 16 where 3-dB contours of the antenna beams are displayed for a three-frequency radar. The beam radii are drawn in a ratio of 1:3:9 and represent the X-band, Ka-band, and W-band 3-dB antenna gain contours. If sensitivity were not an issue, the antenna beamwidths would be designed to be the same at all frequencies—assuring that sample volumes are frequency independent. However, for a system designed to detect cloud parameters at long ranges, the antenna pattern should be designed to maximize signal-to-noise ratio. Since the backscattered power scales inversely with beamwidth, it is important to transmit the narrowest possible beamwidth to achieve optimal signal-to-noise ratio.

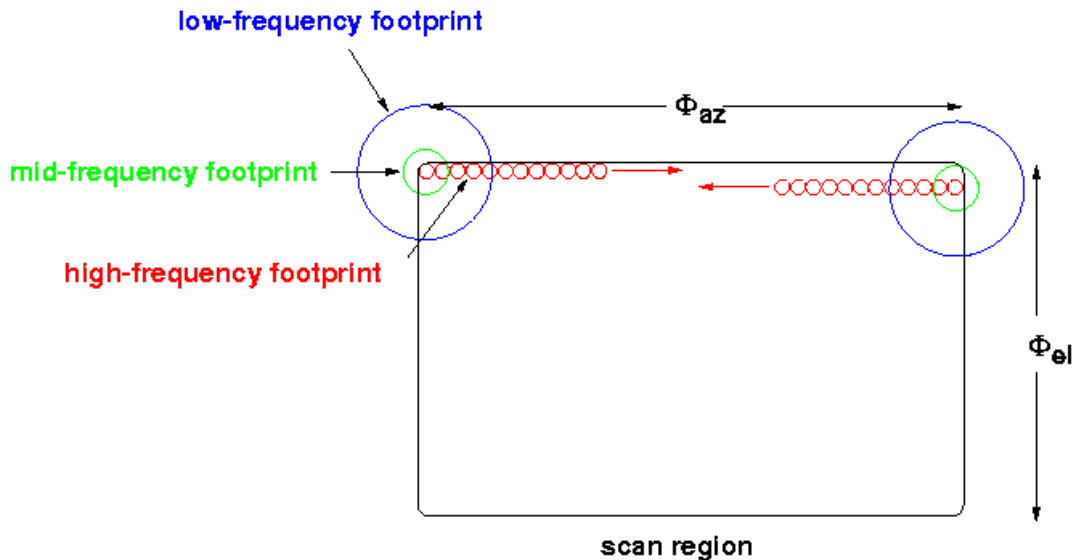


FIGURE 16. SECTOR SCAN WITH THREE-FREQUENCY RADAR

One method to reduce the effect of nonequal beamwidths is to average the higher-frequency beams as shown in figure 17 (the Ka-band footprint is eliminated for clarity). Within the scan volume (spanning Φ_{az} in azimuth and Φ_{el} in elevation), data is averaged into cells, outlined in black in figure 17, representing 50 percent beam overlap in azimuth and elevation for the lowest frequency beam. This provides adequate averaging of the low-frequency beam to generate stable sample statistics. The volume sampled by the lowest-frequency beam (blue) is replicated at the higher frequency by averaging the high-frequency beams (red). Amplitude weights are applied to the higher-frequency beams to replicate the amplitude variation across the lowest-frequency beam.

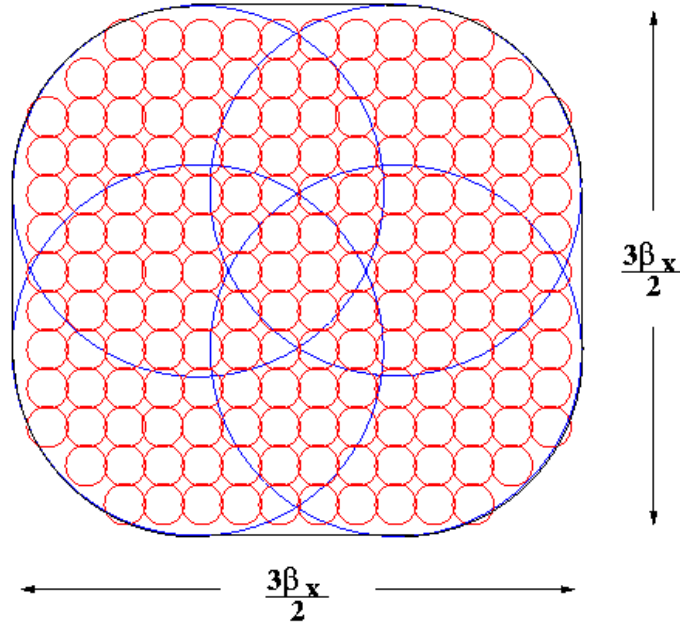


FIGURE 17. BEAM AVERAGING TO ACHIEVE COMMON SAMPLE VOLUME

Referring to figure 16, the total sample volume, expressed in steradians, is equal to the product $\Phi_{az}\Phi_{el}$. With 50 percent beam overlap, the total number of cells in the scan volume can be approximated by taking the ratio of the total cross-sectional area of the scan volume divided by the cell cross-sectional area

$$N_{cells} = \frac{\Phi_{az} \Phi_{el}}{\left(\frac{3\beta_x}{2}\right)^2} \quad (20)$$

where β_x is the 3-dB one-way beamwidth of the X-band antenna (note that the cell cross section is approximated by a square of width $\frac{3\beta_x}{2}$ in equation 20).

The number of pulses averaged within the cell, N_{ave} , is given by the total number of pulses in the entire scan volume divided by the number of cells. The total number of pulses in the scan volume, N_{pulse} , is given by

$$N_{pulse} = f_p T_s \quad (21)$$

where f_p is the radar pulse repetition frequency and T_s is the time required to scan the entire volume. Thus, N_{ave} is given by

$$N_{ave} = \frac{N_{pulse}}{N_{cells}} = \frac{9f_p T_s \beta_x^2}{4\Phi_{az} \Phi_{el}} \quad (22)$$

Noting that the maximum allowable pulse repetition frequency is equal to $C/2R_{max}$ where R_{max} is the maximum range, the maximum value for N_{ave} is given by

$$N_{ave} = \frac{9cT_s \beta_x^2}{8R_{max} \Phi_{az} \Phi_{el}} \quad (23)$$

which shows that the number of averages is governed by the beamwidth of the widest or lowest frequency beam. N_{ave} is plotted in figure 18 for three scan periods of 3.3, 10, and 33 seconds to sweep the entire scan volume. Equation 23 is used in section 2.5 when estimating signal-to-noise ratio.

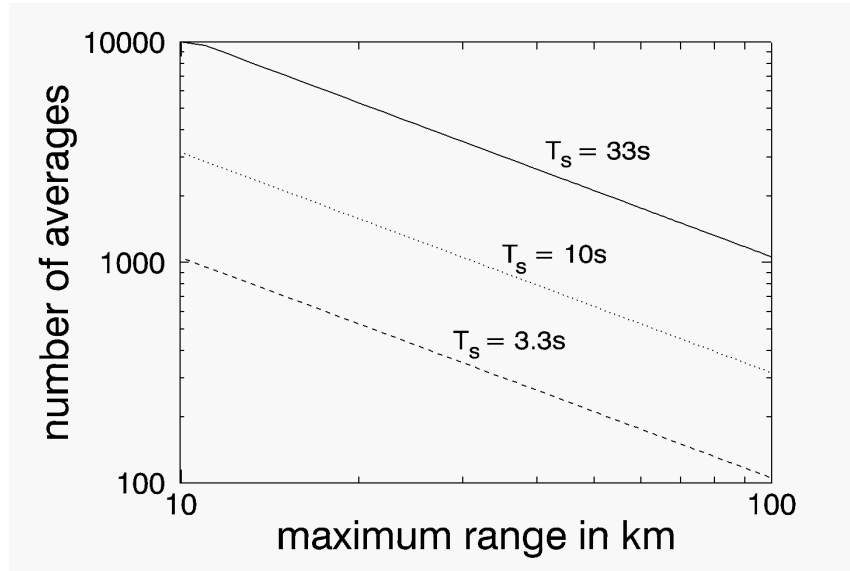


FIGURE 18. NUMBER OF AVERAGES VERSUS MAXIMUM RANGE WITH UPDATE RATE AS A PARAMETER

2.5 SIGNAL-TO-NOISE ANALYSIS.

The sensitivity of a meteorological radar is expressed in terms of the minimum detectable volume backscattering coefficient, η_{min} :

$$\eta_{min} = \frac{1024 \ln(2) \pi^2 R^2 P_{rmin}}{P_t 10^{-2L_a/10} G^2 \lambda^2 \beta^2 c \tau \sqrt{N_{ave}}} \quad (24)$$

where R is the range in meters to the center of the volume cell under observation, P_{rmin} is the minimum detectable signal level in Watts, P_t is the peak power of the transmitter in Watts, L_a is the atmospheric loss in dB/m due to liquid water and water vapor, G is the gain of the antenna, λ is the free-space wavelength in meters, β is the beamwidth of the antenna in radians, and $c\tau/2$ is the length in meters of the range cell in the direction of propagation.

η is related to reflectivity through

$$\eta = 10^{-18} \frac{\pi^5}{\lambda^4} |K|^2 Z. \quad (25)$$

where K is proportional to the complex index of refraction, n

$$K = \frac{n^2 - 1}{n^2 + 2}. \quad (26)$$

Substitution of Z for η is only valid when the scatterers fall within the Rayleigh region, that is, when the maximum drop diameter is less than approximately one tenth of a wavelength, a criteria which is valid below 100 GHz for most nonprecipitating clouds. Converting equation 24 to $10 \log(Z) = \text{dBZ}$ yields

$$\begin{aligned} \text{dBZ}_{min} = & 193.6 + 20 \log R - 20 \log |K| + 20 \log \lambda + P_{rmin} (\text{dBm}) \\ & - P_t (\text{dBm}) + 2L_a - 5 \log(N_{ave}) - 2G(\text{dB}) - 20 \log \beta - 10 \log(c\tau) \end{aligned} \quad (27)$$

For the present problem, it is useful to relate reflectivity to particle diameter for a particular liquid water content. Assuming a monodisperse (constant particle size) particle size distribution, reflectivity is given by

$$Z = \frac{6 \times 10^{12} m_v d^3}{\pi} \quad (28)$$

where d is the particle diameter. Equation 28 is plotted in figure 19 and is used in generating figure 21.

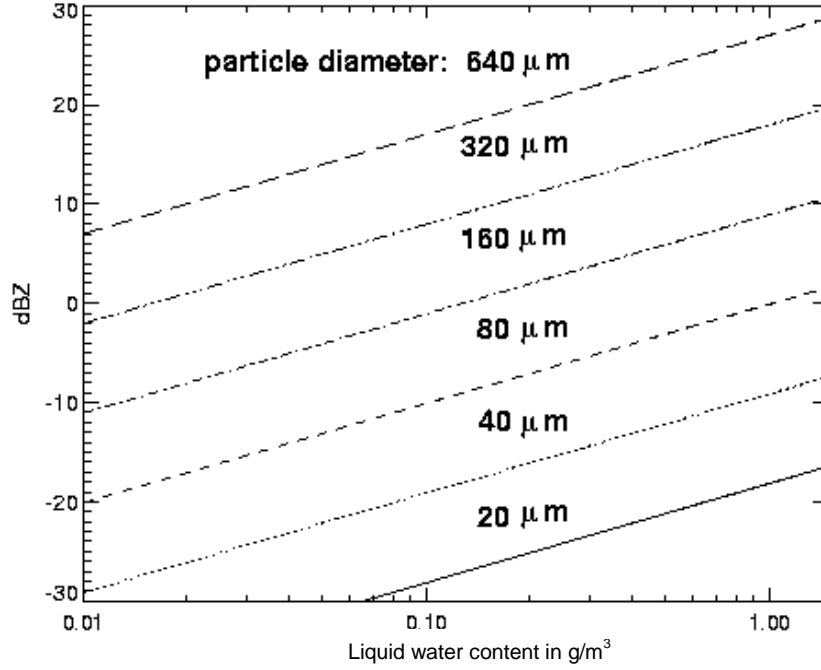


FIGURE 19. CLOUD REFLECTIVITY IN dBZ AS A FUNCTION OF LIQUID WATER CONTENT WITH PARTICLE SIZE AS A PARAMETER

The atmospheric loss term, L_a , in equation 27 is equal to the sum of extinction due to small droplets and loss due to water vapor and oxygen absorption. Absorption by water vapor was computed using formulas found in Ulaby et al. 1981. Loss values computed for the saturation vapor pressure at 800 mb (2-km altitude in standard atmosphere) are tabulated in table 2.

TABLE 2. ABSORPTION DUE TO WATER VAPOR FOR SATURATION CONDITIONS AT 800 mb

Temperature	Frequency		
	10 GHz	35 GHz	95 GHz
0°C	0.0051 dB/km	0.0465 dB/km	0.297 dB/km
-15°C	0.0018	0.0169	0.109

Extinction due to liquid water, k_w , is given by Ulaby et al. 1981,

$$k_w = \frac{.082m_v \operatorname{Im}(-K)}{\lambda} \text{ dB/km} \quad (29)$$

where $\operatorname{Im}(-K)$ is the imaginary part of $-K$. The factor $\operatorname{Im}(-K)/\lambda$ is proportional to $f^{1.95}$ where f is the frequency throughout the microwave region; therefore, loss due to liquid water scales linearly with m_v and scales roughly as the square of the frequency. Figure 20 plots k_w as a function of frequency for various water contents.

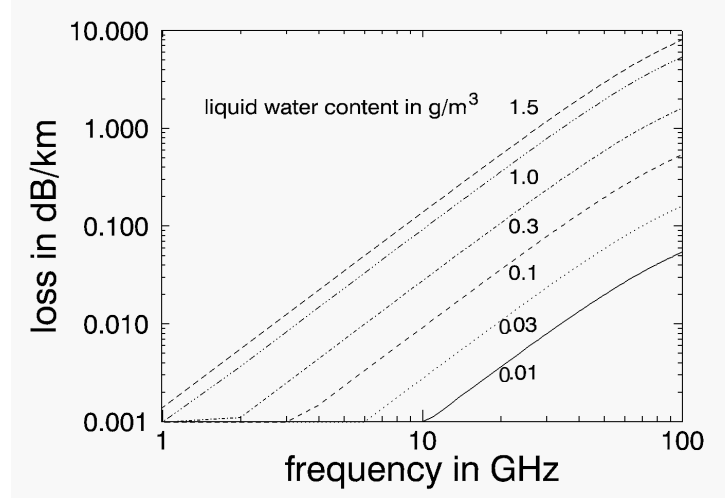


FIGURE 20. ATMOSPHERIC EXTINCTION DUE TO SCATTERING AND ABSORPTION BY LIQUID WATER AT 0°C

2.5.1 Minimum Detectable Particle Size.

Equations 27 and 28 were combined to solve for the minimum detectable particle diameter as a function of range for the pulsed, high-power radar parameters shown in table 3. These results are displayed for 10, 35, and 95 GHz in figure 21 (assumptions: monodisperse particle size distribution, Rayleigh scattering, and uniform cloud layer). Cloud liquid water content was varied between 0.01 and 1.5 $\text{g}\cdot\text{m}^{-3}$, which strongly affects the depth of penetration for the 35- and 95-GHz radars. The dominance of the atmospheric loss term in equation 24 causes the range performance to degrade for higher liquid water contents, even though Z increases linearly with m_v . The curves for the highest liquid water content should be viewed as worst case, i.e., they assume the average liquid water content is 1.5 $\text{g}\cdot\text{m}^{-3}$.

TABLE 3. PARAMETERS FOR A HIGH-POWERED, TUBE-PULSED RADAR USED IN ESTIMATING RANGE PERFORMANCE OF MULTIFREQUENCY RADAR

Parameter	Radar Frequencies		
	10 GHz	35 GHz	95 GHz
P_t , dBm	70	62	62
G , dB	26	37	47
P_{min} , dBm	-124	-123	-122
β , radians	0.122	0.034	0.013
λ , m	0.03	0.0086	0.00316

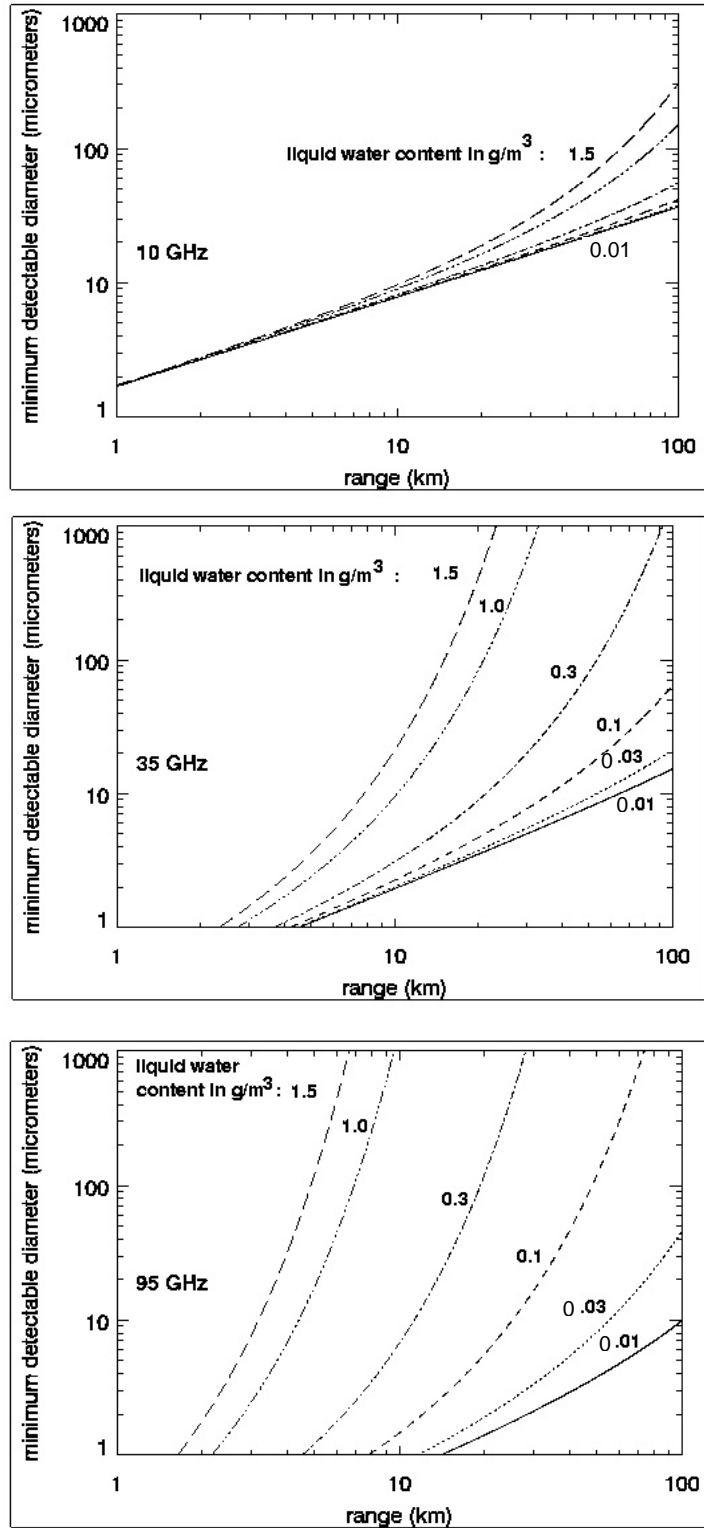


FIGURE 21. MINIMUM DETECTABLE PARTICLE DIAMETER VERSUS RANGE WITH LIQUID WATER CONTENT AS A PARAMETER AT 10, 35, AND 95 GHz

2.5.2 Statistical Analysis of Range Performance.

Range performance can also be simulated by assuming varying cloud water content, following the statistics presented by Cooper et al. 1982. They report that 1 km averaged data exceeded $0.1 \text{ g}\cdot\text{m}^{-3}$ 5 percent of the time and exceeded $0.5 \text{ g}\cdot\text{m}^{-3}$ only 1 percent of the time. Over a 10-km path, m_v exceeded $0.5 \text{ g}\cdot\text{m}^{-3}$ only 0.5 percent of the time. These statistics can be used to generate more representative plots of range performance at all three frequencies.

To simplify generation of liquid water statistics, cloud cells of 3 km length were generated where 95 percent of the clouds were uniformly distributed between 0.0 and $0.1 \text{ g}\cdot\text{m}^{-3}$, 4.3 percent of the clouds had liquid water contents between 0.1 and $0.5 \text{ g}\cdot\text{m}^{-3}$, and 0.7 percent had liquid water content exceeding $0.5 \text{ g}\cdot\text{m}^{-3}$. Using 3-km cells balances Cooper et al.'s statistical requirements for 1 and 10 km averaging lengths. The cumulative distribution function (CDF) for this example is shown in figure 22. In addition to varying the liquid water content, the temperature was varied randomly, as shown in figure 23.

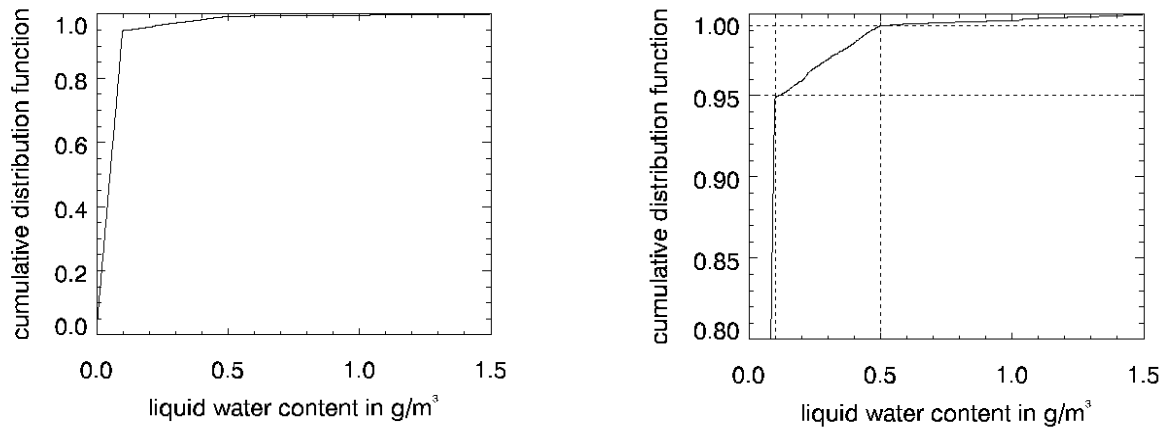


FIGURE 22. CUMULATIVE DISTRIBUTION FUNCTION (LEFT) AND HIGHEST 20 PERCENT OF CDF (RIGHT) FOR SIMULATED CLOUD LIQUID WATER CONTENT

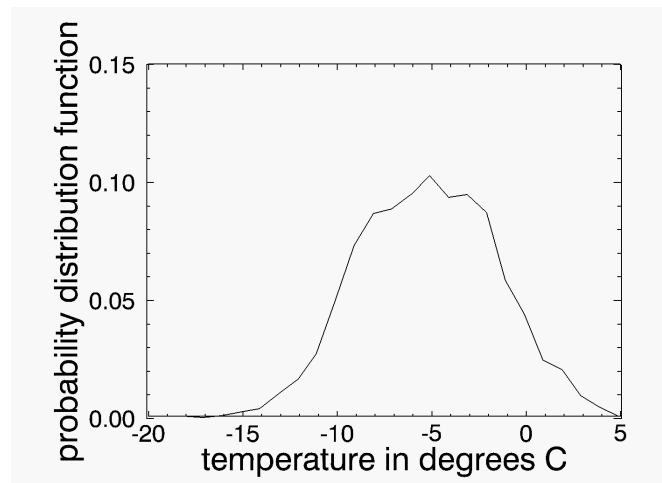


FIGURE 23. SIMULATED TEMPERATURE DISTRIBUTION

Typical range profiles of temperature and liquid water content are shown in figure 24 for the radar parameters of table 3. Simulations of minimum detectable reflectivity are displayed for 10, 35, and 95 GHz in figure 25 and include the effect of water vapor absorption at zero degrees centigrade, assuming 100 percent relative humidity. One hundred different range profiles of randomly varying clouds were simulated in generating figure 25. The spread in the data represents the statistical distribution of the total attenuation between the radar and the range corresponding to the data point. This figure, along with figure 19, can be used to estimate the probability of detecting a particle of a given size versus range.

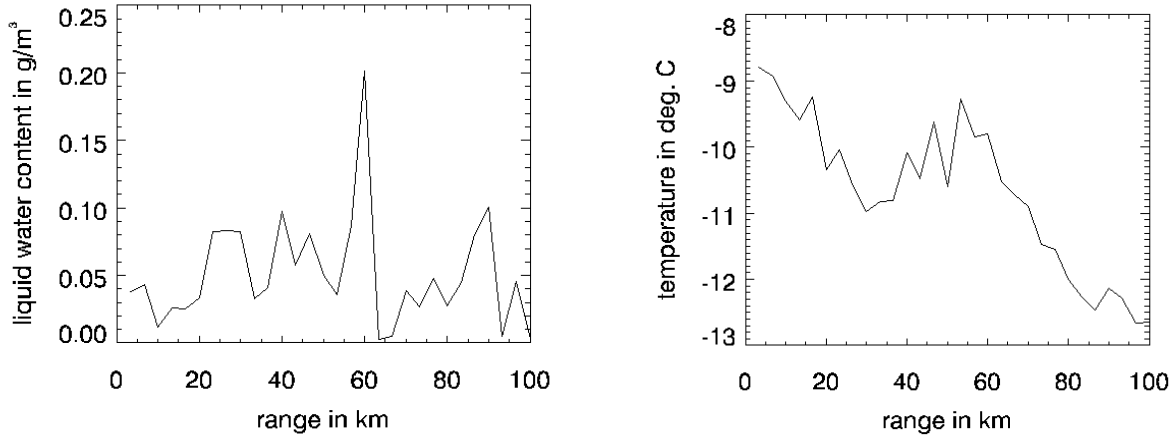


FIGURE 24. TYPICAL RANGE PROFILES OF LIQUID WATER AND TEMPERATURE

2.5.3 Sensitivity of Solid-State Radar.

A similar statistical analysis was carried out for three solid-state cloud radars, as shown in figure 26, using the FM-CW radar parameters given in table 4. The beamwidth assumes separate 0.2-m-diameter antennas. These data show between 15 and 20 dB less sensitivity for the solid-state systems as compared to the pulsed systems. This means that the minimum detectable particle size for the solid-state radar is between three and four times larger than for the tube-powered systems.

TABLE 4. PARAMETERS USED IN ESTIMATING RANGE PERFORMANCE OF SOLID-STATE FM-CW MULTIFREQUENCY RADAR

Parameter	Radar Frequencies		
	10 GHz	35 GHz	95 GHz
P_b , dBm	40	33	27
G , dB	24	35	44
P_{rmin} , dBm	-136	-135	-134
β , radians	0.118	0.05	0.02
λ , m	0.03	0.0086	0.0032

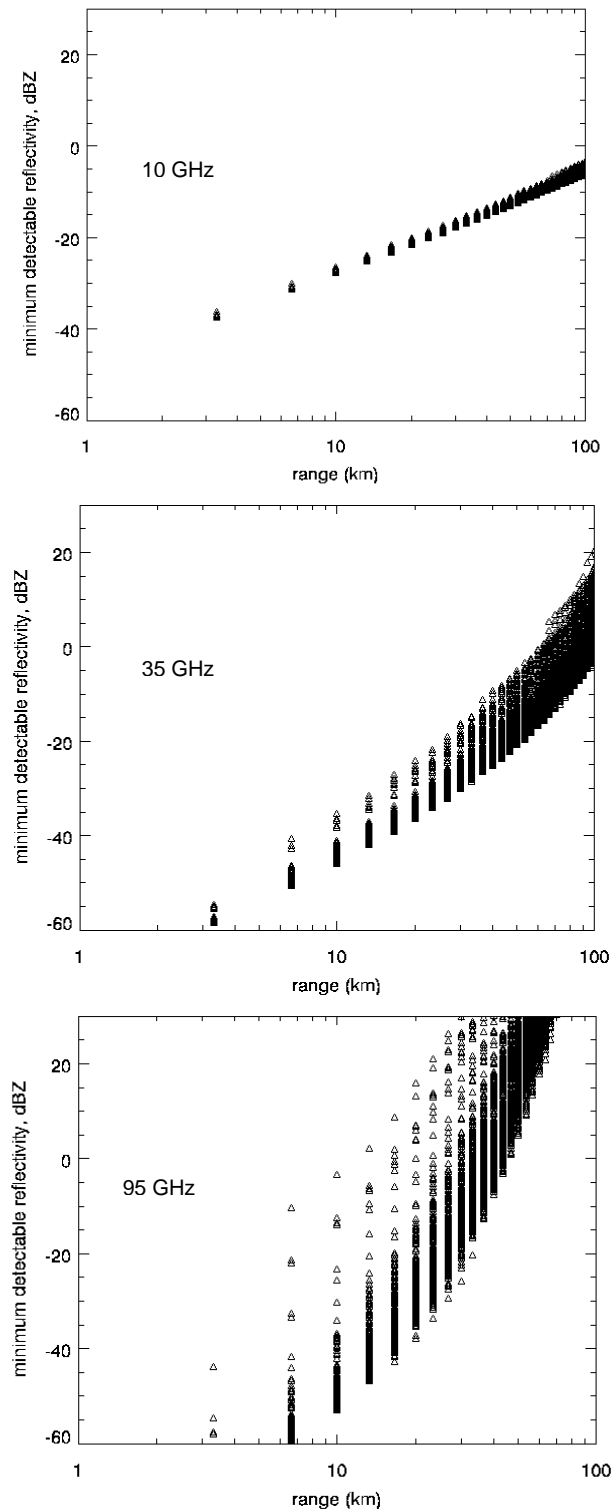


FIGURE 25. MINIMUM DETECTABLE REFLECTIVITY VERSUS RANGE WITH SIMULATED CLOUD LIQUID AND TEMPERATURE DISTRIBUTION AT 10, 35, AND 95 GHz FOR A TUBE-POWERED SYSTEM

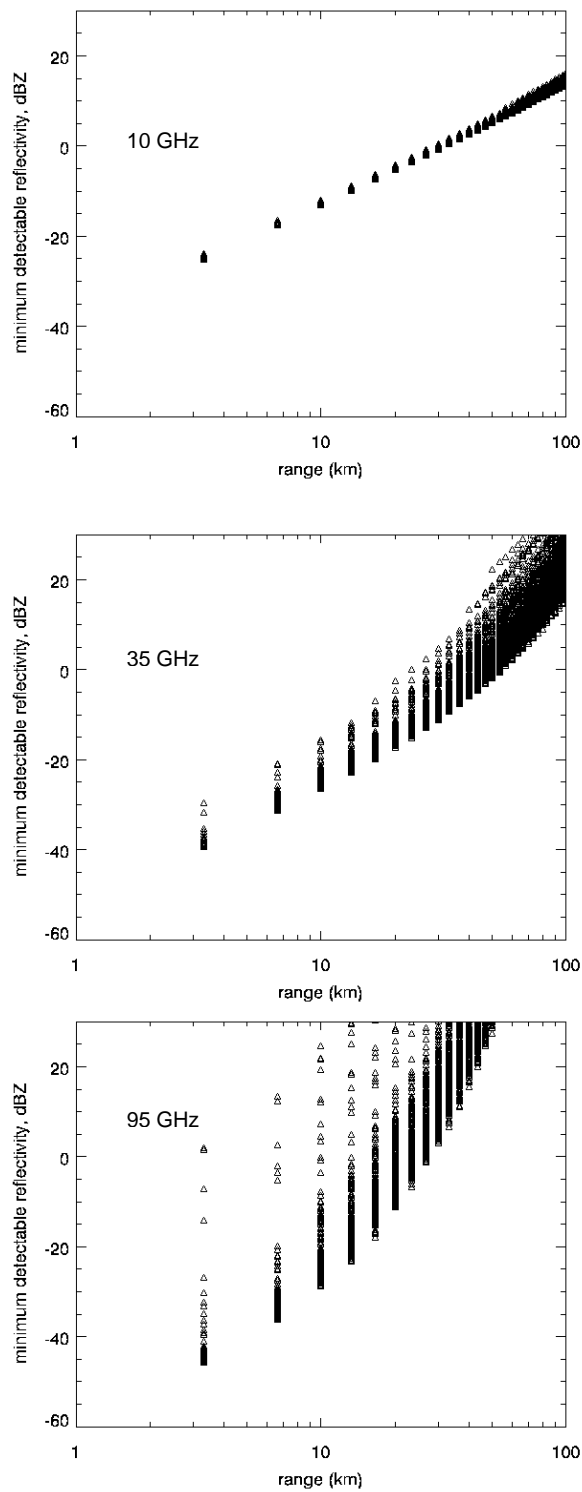


FIGURE 26. MINIMUM DETECTABLE REFLECTIVITY FOR SOLID-STATE RADARS WITH SIMULATED CLOUD LIQUID AND TEMPERATURE DISTRIBUTION AT 10, 35, AND 95 GHz

3. LIDAR.

Published studies have shown that a multiple-field-of-view lidar operating at $10.6\ \mu\text{m}$ can extract liquid water content and particle size distribution at short ranges [Hutt et al., 1994]. Optical attenuation due to scattering from small droplets is the primary factor limiting the utility of lidar for long-range particle sizing. The optical limit extinction coefficient is plotted as a function of drop diameter in figure 27 with liquid water content as a parameter. The dashed line indicates a loss of 1 dB/km, which cannot be exceeded if a penetration depth of 30 km is required. The lidar will only be effective for icing potential detection for particles falling within the shaded area shown in this figure (i.e., the region of low attenuation with liquid water content above $0.05\ \text{g}\cdot\text{m}^{-3}$). This shows that the lidar will only be effective in supercooled liquid with particles larger than 500 micrometers—primarily drizzle or rain.

One scenario that might benefit from lidar is drizzle or mixed phase ice and drizzle below cloud base. Figure 28 plots liquid water content as a function of rain rate assuming a Marshall-Palmer drop-size distribution for drizzle and rain (the curves for drizzle and rain are essentially identical). Taken together, figures 28 and 27 indicate that for drizzle rates of 1 mm/hr or less the liquid water content is small enough to allow optical propagation with low attenuation. Neural network simulations of a lidar with three-frequency radar confirmed an improvement in sizing drizzle sized particles as seen in figure 29. However, no sizing improvement was found for the bulk of the supercooled icing region.

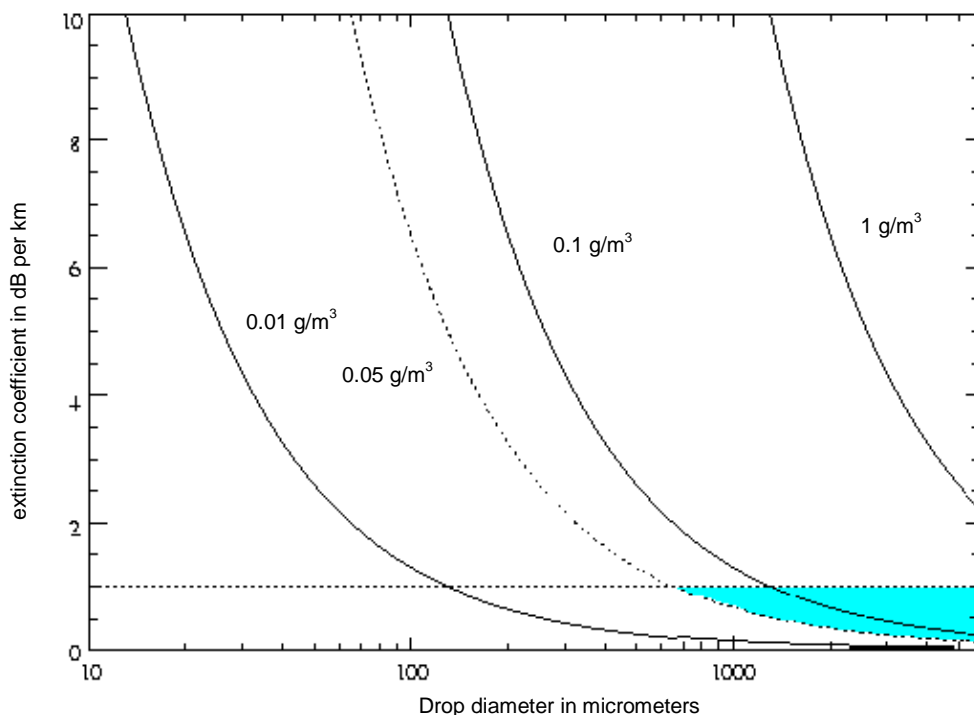


FIGURE 27. OPTICAL EXTINCTION COEFFICIENT FOR LIQUID WATER CONTENTS BETWEEN 0.001 AND 1 GRAM/CUBIC METER
(Assumptions: optical limit (particle much larger than one wavelength); monodisperse drop-size distribution. Shading highlights region that may benefit from lidar.)

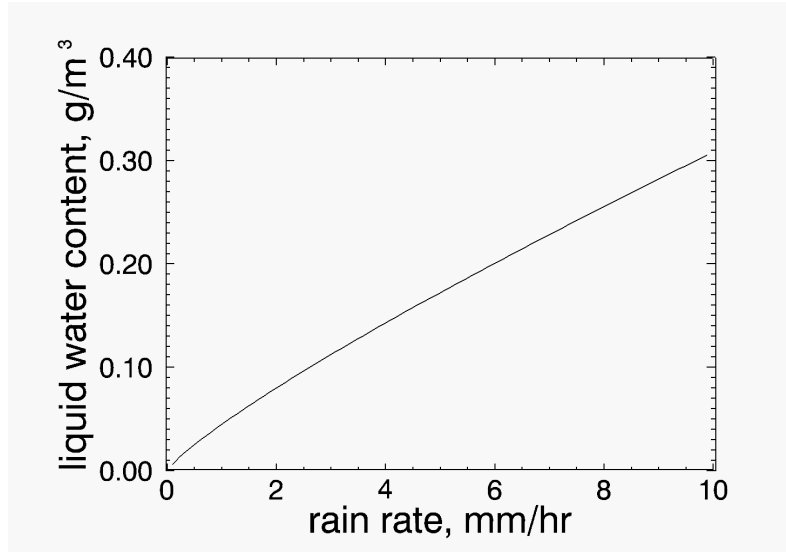
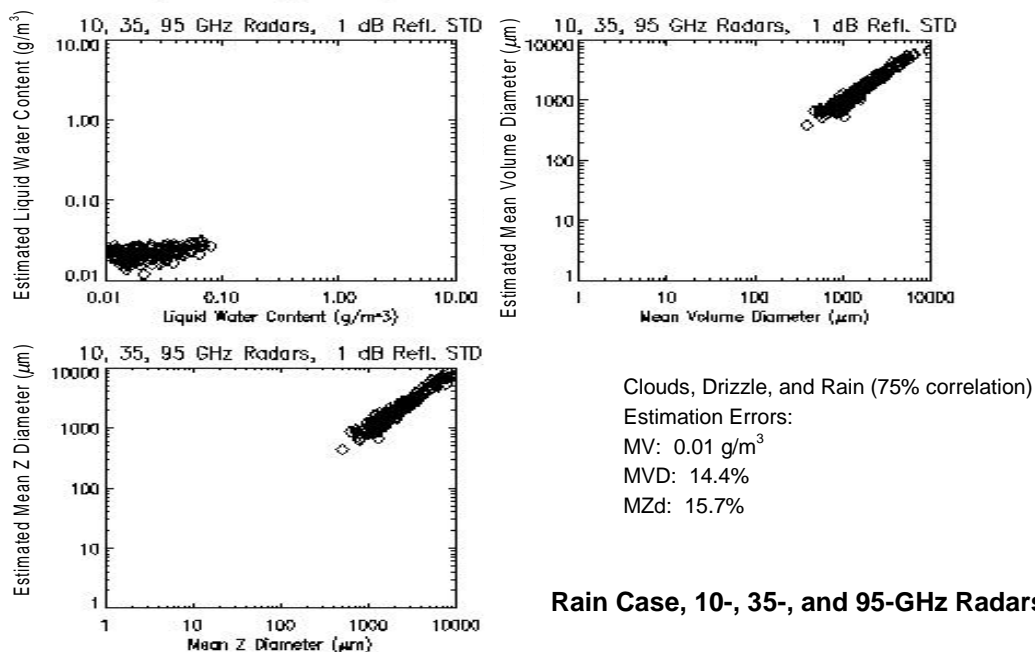


FIGURE 28. LIQUID WATER CONTENT VERSUS RAIN RATE
(Liquid water content is less than $0.05 \text{ g}\cdot\text{m}^{-3}$ for rain rates below 1 mm/hr.)

Another potential advantage of lidar is its ability to detect ice. The polarization lidar technique has been used in cloud research since the 1970s [Sassen, 1991]. Polarization lidar uses a single transmit polarization and a dual-polarized receiver to measure linear depolarization ratio, termed δ in the lidar literature. Since ice depolarization is usually quite strong, δ is normally expressed in linear, as opposed to logarithmic, units. Sassen presents a useful figure, displaying a linear depolarization ratio for various ice habits and water droplets, derived from laboratory and field studies. In the absence of multiple scattering, there is a clear separation between scattering from water droplet clouds (δ less than 0.15) and various frozen hydrometeors (δ in the range of 0.4 to 0.7.)

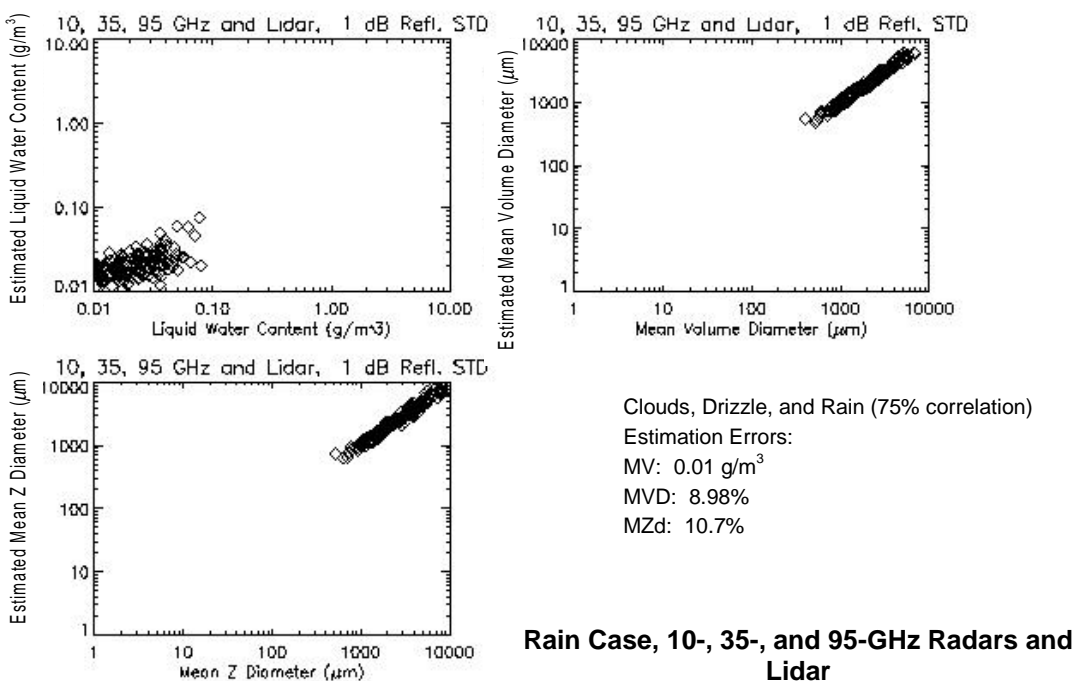
Depolarization due to multiple scattering in water clouds can be large with δ values in excess of 0.5 reported for penetration depths of less than 200 meters [Pal and Carswell, 1973]. Depolarization is much less a problem in drizzle, since droplet concentration is greatly reduced. According to Sassen, drizzle causes very little depolarization since the particles are “small enough to stay spherical and the concentrations are usually small enough to significantly negate multiple scatter” [Sassen, 1998]. Multiple scatter can also be greatly reduced by using a narrow field-of-view lidar. According to Sassen, “very narrow lidar beamwidths can seriously restrict the viewing of multiple scatter and cause only small depolarization increases—high spectral resolution lidars, for example, hardly see more than a few percent linear depolarization ratio (LDR) increases in dense water clouds” [Sassen, 1998]. These facts suggest that a lidar can detect the presence of ice over many kilometers and could be an aid to detecting mixtures of ice and drizzle. However, the minor advantage gained by being able to detect precipitating ice or mixtures of ice and drizzle does not provide strong motivation for including a lidar in a practical in-flight system.

Case #2 (1 of 2 figures):



Rain Case, 10-, 35-, and 95-GHz Radars

Case #2 (2 of 2 figures):



Rain Case, 10-, 35-, and 95-GHz Radars and Lidar

FIGURE 29. LARGE DROPLET PARTICLE SIZING USING THREE-FREQUENCY NEURAL NETWORK (TOP) AND THREE-FREQUENCY NEURAL NETWORK PLUS LIDAR (BOTTOM)

4. TEMPERATURE PROFILING.

Ideally, an airborne icing avoidance system will include an instrument capable of remote temperature measurements. Even though horizontal temperature gradients are usually small over short distances, a few degrees increase in temperature can provide an escape window out of dangerous icing conditions. Two methods for temperature profiling were considered: oxygen band radiometry and RASS. These are described separately in the following sections.

4.1 OXYGEN BAND RADIOMETRY.

Dr. Goodberlet of Quadrant Engineering Inc. prepared a report on radiometric profiling of temperature, which is attached as appendix A to this report. The findings of appendix A are summarized below:

- a. Horizontal temperature profiling using a 50- to 60-GHz radiometer will work with accuracy similar to vertical profiling radiometers (2-3 K, rms) when range resolution is scaled linearly (1:1) with range. For example, at a range of 20 km, the reported temperature will represent an average of the atmospheric temperature between 10 and 20 km with an accuracy of 2-3 K.
- b. Some auxiliary method must be used to correct for liquid water and water vapor fluctuations. For example, the estimate of liquid water content made by the neural network algorithm could be used to correct the radiometer data.

This study has demonstrated that a radiometer can profile temperature over a horizontal path. However, implementation problems suggest that the technique may not be practical. These problems include:

- Correcting for liquid water at ranges beyond the detection capability of the radar.
- Accounting for loss due to water and ice on the radome (see section 5 and appendix B).

Correcting for contamination from ground emissions is another significant problem, although this can be reduced to manageable levels by using a narrow beam.

A temperature profiling radiometer could be added to the proposed radar design described in section 6 for about 10 percent of the total cost of the prototype system. However, the instrument's coarse range resolution and susceptibility to errors argue against the added expense of a radiometric channel for horizontal temperature profiling.

The results of the analysis presented in appendix A suggest that a low-cost radiometer could be developed for upward and downward looking temperature profiling. Placing several radiometer channels between 55 and 60 GHz can allow downward looking profiling without serious ground contamination, which is more of a problem at lower frequencies (below 55 GHz). Such an instrument may provide valuable information if a pilot needs to escape an icing condition and can detect warm air above or below the aircraft.

4.2 TEMPERATURE PROFILING USING RASS.

RASS operates using the principle of Bragg interaction between an acoustic wavefront and an electromagnetic signal, as shown in figure 30 [Frankel and Peterson, 1976]. Bragg resonance occurs when $\lambda_e = 2\lambda_a$ where λ_e is the electromagnetic wavelength and λ_a is the acoustic wavelength. The scattering efficiency of an acoustic wavefront of n wavelengths increases as n^2 due to the coherent summation of the backscattered electric field from each wave crest. The speed of sound, V_s , is related to the absolute temperature, T , by the following formula, assuming still air:

$$V_s = 20.05\sqrt{T} \quad (30)$$

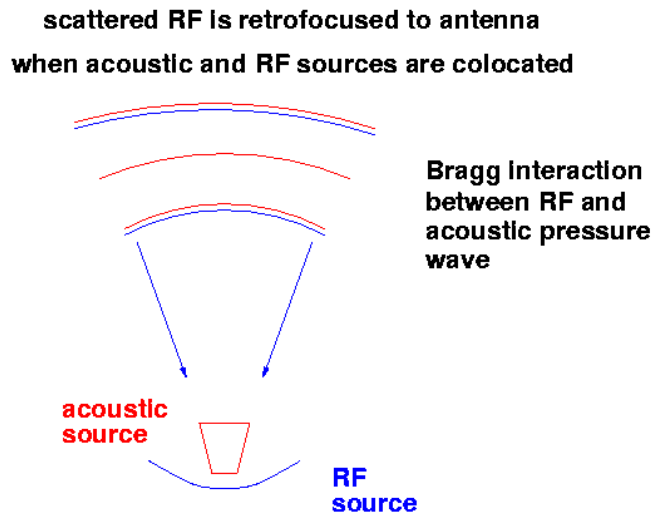


FIGURE 30. RADAR ACOUSTIC SOUNDING SYSTEM CONCEPT

The airborne RASS concept is shown in figure 31. Acoustic power emitted by the engines (equivalent to a 0.1 to 1 kW isotropic source in the forward direction) creates an acoustic wavefront traveling at the speed of sound, c . The aircraft traveling at v lags behind this wavefront at a distance $(c-v)t_l$. The acoustic wavefront and RF wavefront interact coherently over a small section of the spherical wavefront, where the phase difference between the RF and acoustic wavefronts is less than $\pi/4$.

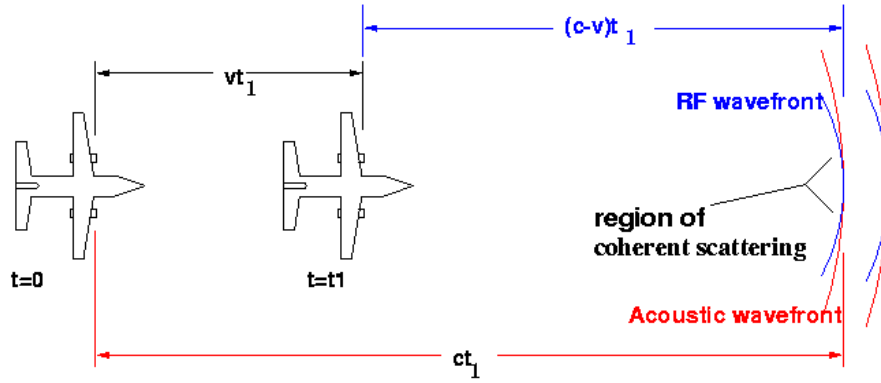


FIGURE 31. AIRBORNE RASS CONCEPT

The effective beamwidth over which the phase error is small can be computed using the following formula, where the geometry is shown in figure 32.

$$\varepsilon = 2k_e \left[(c-v)t_1 (\sec \theta - 1) - ct_1 (\sec \theta - 1) \sec(\phi - \theta) \right] \quad (31)$$

where ε is the RF phase difference between acoustic and RF wavefronts, k_e is the electromagnetic wavenumber, and θ and ϕ are related by

$$\theta = \sin^{-1} \left[\frac{c-v}{c} \sin \phi \right] \quad (32)$$

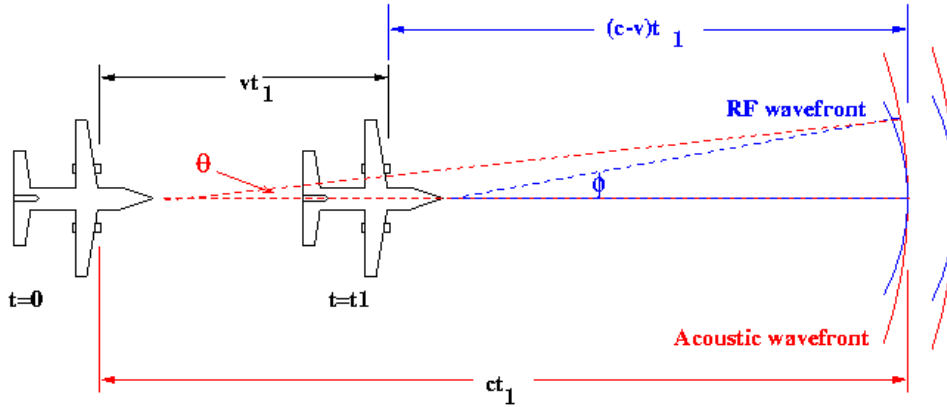


FIGURE 32. AIRBORNE RASS GEOMETRY

Phase error as a function of θ is plotted in figure 33 for the conditions given in table 5. This shows that a two degree sector of the acoustic wavefront will maintain phase coherence with the RF wavefront, assuming ideal acoustic propagation. This wavefront can be significantly disturbed by horizontal winds and turbulence.

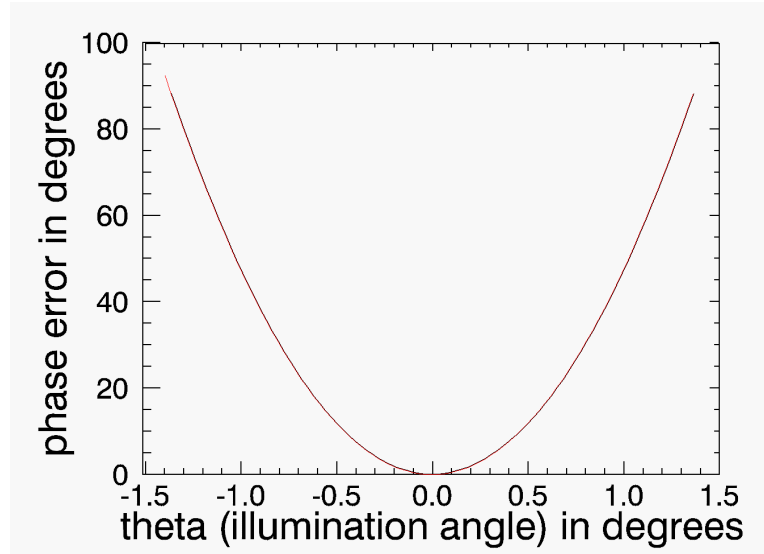


FIGURE 33. PHASE ERROR IN DEGREES VERSUS ILLUMINATION ANGLE θ

TABLE 5. CONDITIONS FOR EVALUATING EQUATION 31

Parameter	Value
Speed of sound, c	340 m/s
Aircraft velocity, v	100 m/s
range to acoustic wavefront $(c-v) t_1$	10 km
t_1	41 s

Using Marshall's equation for signal-to-noise ratio (SNR) for a RASS [Frankel and Peterson, 1976] allows the effective range of a RASS to be computed for ideal conditions. Figure 34 displays SNR versus range for the conditions listed in table 6. Acoustic attenuation of 0.9 dB/km at 100 Hz was found in an article by Marshall et al., 1972. The acoustic power of 300 W was estimated from ground measurements of a two-blade propeller over ground [Hubbard and Lassiter, 1951] for a tip speed over Mach 1.2. Three hundred W corresponded to acoustic power with a drive power of 362 hp. Figure 34 shows that RASS should work to ranges of 10 km for the parameters given in table 6.

There are two other factors known to degrade the performance of RASS that could limit the range performance below that predicted by figure 34. These are the effects of advection of the acoustic wavefront by horizontal winds and the effects of turbulence in degrading the coherence of the acoustic wavefront. For ground-based RASS, these factors limit the height coverage to a few kilometers. We expect that variations in crosswinds over a 20- to 30-km path could significantly shift the focal point of the acoustic wavefront, further reducing the backscattered signal strength. This effect, combined with loss of coherence due to turbulence, will likely limit the maximum range to distances less than 10 km, even for slow-moving aircraft, such as helicopters.

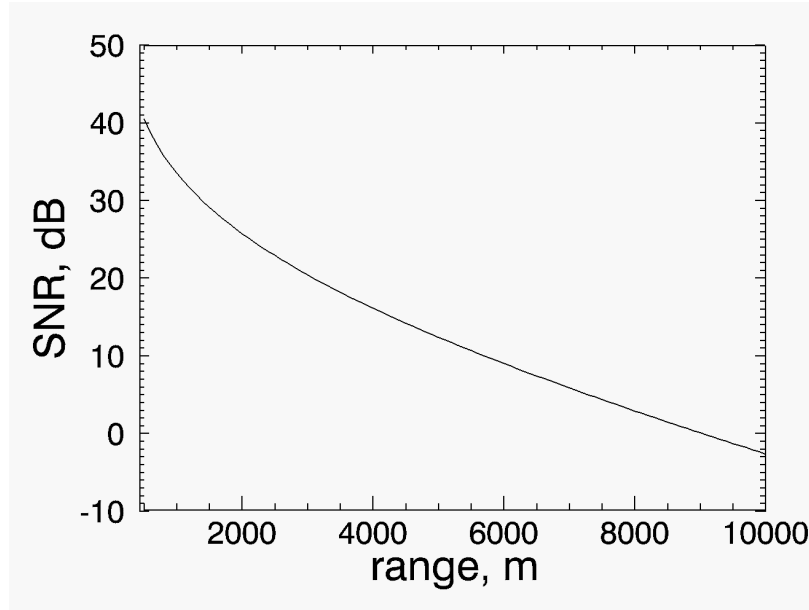


FIGURE 34. RASS SNR VERSUS RANGE

TABLE 6. CONDITIONS USED IN PREDICTING SNR FOR AIRBORNE RASS

Parameter	Value
RF peak power	1 kW
Acoustic power	300 W
RF antenna gain	16 dB
Range resolution	1 km
Integration time	2 s
Acoustic attenuation	09 dB/km

4.3 SUMMARY OF TEMPERATURE PROFILING RESEARCH.

In summary, neither of the horizontal temperature profiling techniques investigated were considered promising enough to warrant prototyping or further investigation. The radiometer technique is capable of long-range profiling but results in very coarse spatial resolution and is subject to errors that are difficult to account for in practice. The RASS technique is capable of fine spatial resolution but has poor sensitivity beyond a few kilometers range. Finally, it is noted that the multifrequency radar neural network was initially trained to extract temperature profiles along with liquid water content, MVD, and MZD. Although the neural network was able to profile temperature in the absence of measurement errors, these errors became high as soon as noise was added to the radar data.

5. MULTIFREQUENCY RADOME AND LOSSES DUE TO ICE AND WATER.

Any radar or radiometer used for an icing potential detection system will require a radome as pictured in figure 35. A multiple frequency radome can readily be designed from a solid

dielectric by specifying radome thickness as a multiple of a half-wavelength at all frequencies. This is readily achieved by selecting operating frequencies that are integer multiples of the lowest frequency. For example, 10.5, 31.5, and 94.5 GHz form a set of three frequencies that are all matched to a Rexolite radome 0.227 inch thick. Broader bandwidths can be achieved by using a multilayer radome approach, which will allow any frequency combination to be used. However, for the present analysis, the simplest single-layer design was employed.

Radomes are subject to ice and water buildup, both of which will have a significant effect on power transmission and the measured radiometric brightness temperature. Loss can be computed using a simple plane wave analysis, assuming the rectilinear geometry shown in figure 35. In figure 36 the transmission of a dry radome and ice/water coated radome is plotted versus frequency. Note that the dry radome has no transmission loss at the three design frequencies of 10.5, 31.5, and 94.5 GHz. Adding only 1 cm of ice and 0.3 mm of water significantly degrades insertion loss. The additional two-way loss at 94.5 GHz for this case is over 7 dB. Similar calculations were carried out in figures 37-40 for the response at 10.5, 31.5, and 94.5 GHz for three different cases: ice coated radome versus ice thickness (figure 37); same case with 0.3 mm coating of water (figure 38), and loss versus water thickness with and without ice (figures 39 and 40).

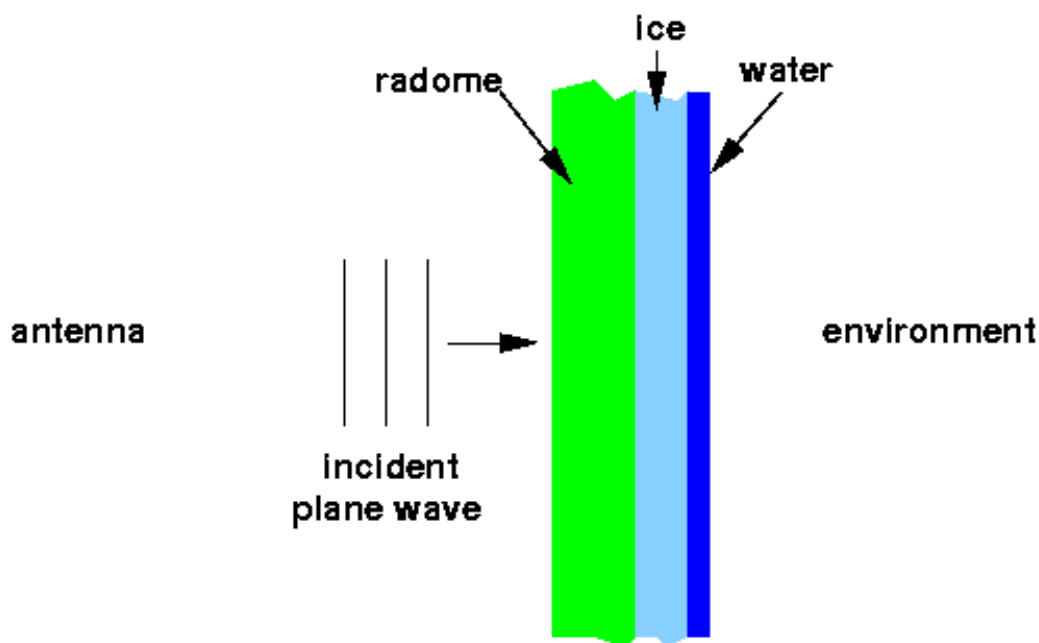


FIGURE 35. RADOME SHOWING ICE AND WATER BUILDUP

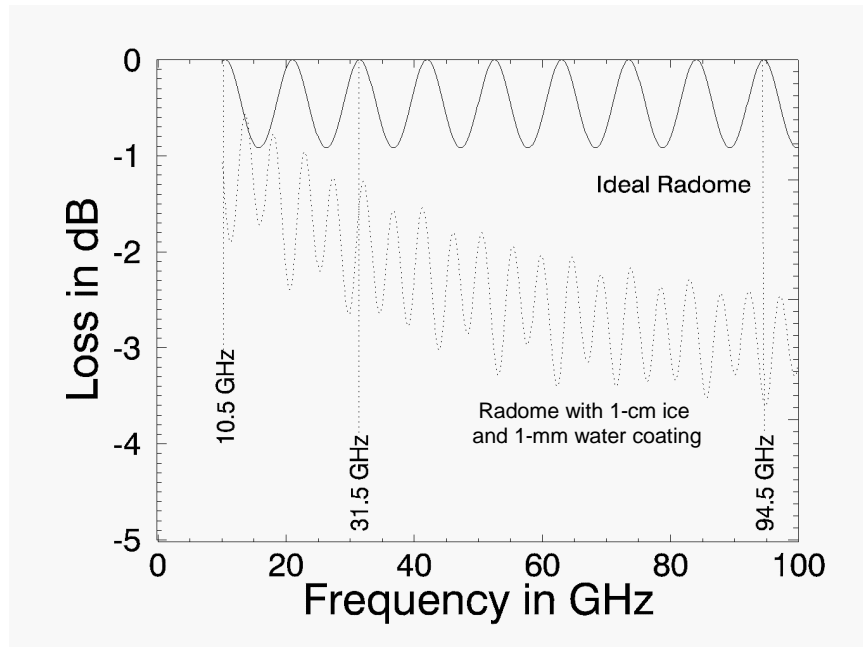


FIGURE 36. ONE-WAY TRANSMISSION LOSS OF DRY RADOME AND RADOME COATED WITH 1 cm OF ICE AND 0.3 mm OF WATER

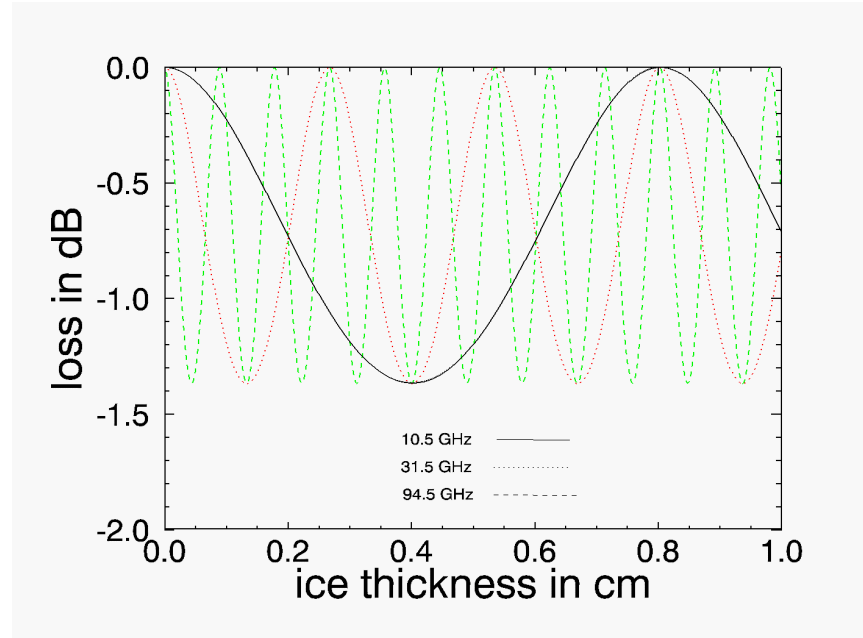


FIGURE 37. TRANSMISSION LOSS AS A FUNCTION OF ICE THICKNESS

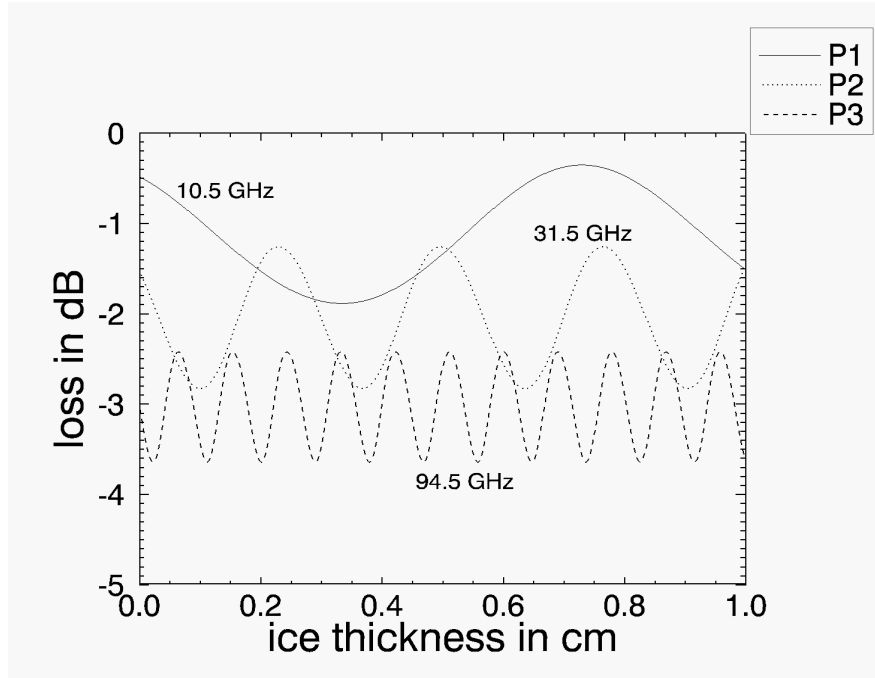


FIGURE 38. TRANSMISSION LOSS AS A FUNCTION OF ICE THICKNESS WITH 0.3-mm COATING OF WATER

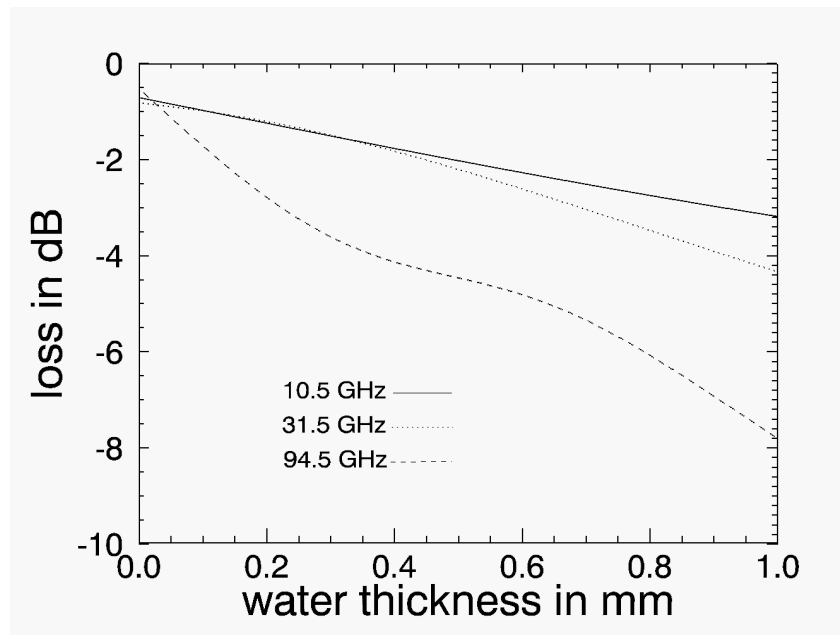


FIGURE 39. TRANSMISSION LOSS AS A FUNCTION OF WATER THICKNESS ASSUMING ICE THICKNESS OF 1 cm

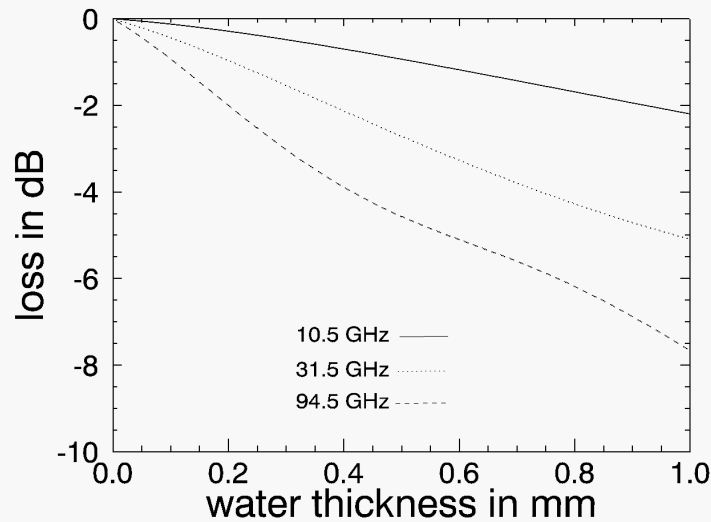


FIGURE 40. TRANSMISSION LOSS AS A FUNCTION OF WATER THICKNESS WITHOUT ICE

Nose radomes covering X-band weather radars do not need to be deiced since absolute calibration is not critical and two-way loss due to ice buildup is never more than 3 dB. For the current application, radome deicing will assure that the loss at higher frequencies is as low as possible, a critical issue when sensitivity is at a premium.

Loss due to water is difficult to quantify without a knowledge of water thickness as a function of deposition rate, air speed, and radome shape. It is unlikely that water would exceed a few hundred micrometers in thickness for nonprecipitating conditions. It is possible to monitor water build-up using capacitive probes embedded in the radome. This would allow the system to compensate for the frequency dependent water loss—information that could be used by the neural network inversion algorithm or by a radiometric channel.

Dr. Goodberlet has prepared a short report (appendix B) on the effects of radome water and ice on the temperature profiling radiometer.

6. PROPOSED PROTOTYPE SYSTEM DESIGN.

The prototype system will be used as a research tool to evaluate the ability to detect icing potential under a wide range of conditions. As such, it should be designed with as much sensitivity as possible and should include at least a single polarimetric channel. Quadrant recommends that a prototype multiparameter radar system for research applications include the following components:

- Three-frequency radar sharing a common antenna
- Limited scan capability to allow sampling of common volume at all three frequencies
- Tube-powered transmitters at all three frequencies
- Dual polarized X-band channel configured to measure Z_{dr}

A block diagram of the proposed prototype system is shown in figure 41. Most of the components will be mounted separately from the scanning unit, although the 95-GHz components must be mounted to the antenna to minimize waveguide loss. The details of exactly how the scanning mechanism will be implemented will be worked out during the design phase. For example, it may be possible to scan the subreflector or use a pair of dielectric wedges for scanning.

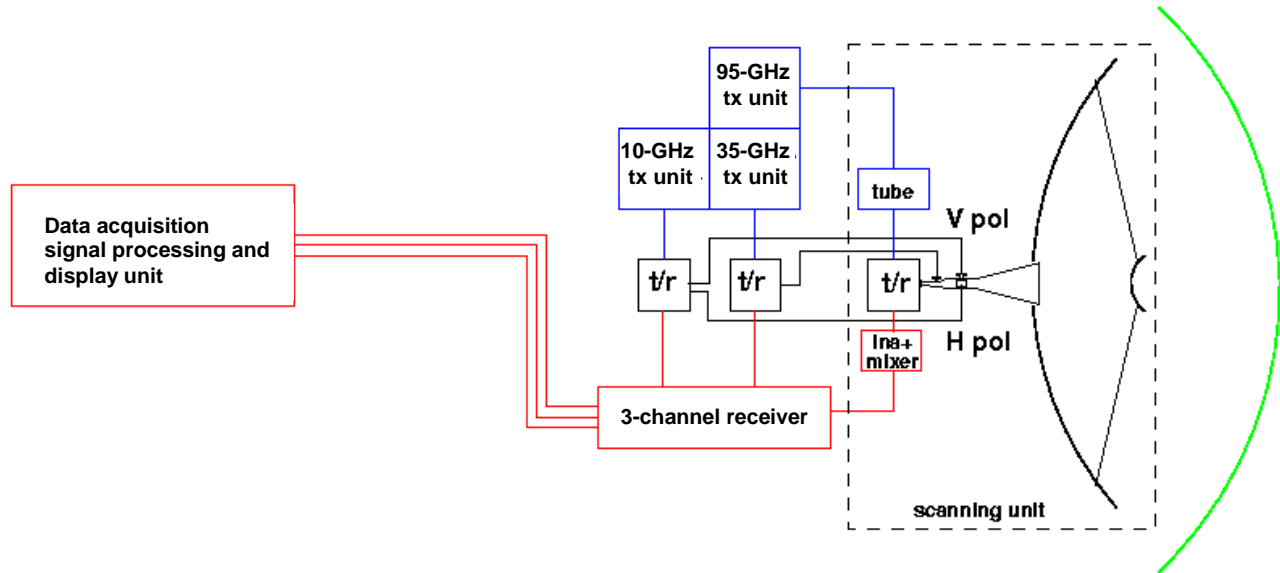


FIGURE 41. SYSTEM BLOCK DIAGRAM OF THE PROPOSED MULTIFREQUENCY RADAR

Specifications for the radar are provided in table 7. The transmitters consist of a modulator and transmit tube, probably a magnetron at 10 GHz, and an extended interaction klystron oscillator (EIKO) at 35 and 95 GHz. By using an oscillator-based system, as opposed to a fully coherent system using power amplifiers, significant savings can be achieved on the cost of millimeter wave sources, waveguides, switches, etc. Since no Doppler measurements are proposed, savings can also be realized in the cost of the data acquisition system. Instead of coherent detection, the proposed design uses simple log detectors and noncoherent integration circuitry. This will greatly simplify receiver design and data acquisition requirements.

A block diagram of the receiver is shown in figure 42. Each individual receiver will include a low-noise amplifier (LNA), filter, mixer combination with a stable local oscillator (STALO) to down-convert the signal to a few hundred MHz. An automatic frequency control (AFC) loop (not shown) will control the frequency of the STALO to keep the scattered signal within the passband of the receiver. The output of the log detector will be sampled by a 192 kilosample/second multichannel digitizer (HP-E1433A or equivalent). These data can be processed in real time by an on-board DSP processor (HP-E1485 or equivalent) to display range profiles of reflectivity in flight. The VXI-to-SCSI interface will allow storage of all raw data, which is essential for testing the inversion algorithm. Ancillary data generated by the INS, temperature probes, and antenna position controller will be also be merged with the raw data stream.

TABLE 7. SPECIFICATIONS FOR THE PROPOSED MULTIPARAMETER RADAR

Parameter	Radar Frequencies		
	10 GHz	35 GHz	95 GHz
Transmitter	Magnetron	EIKO	EIKO
P_t , dBm	70	62	62
Pulse repetition frequency, Hz	1.0-5.0	1.0-5.0	1.0-5.0, variable
Receiver noise figure, dB	2.0	3.0	4.0
Receiver bandwidth, kHz	75	75	75
Pulse length, μs	13.2	13.2	13.2
Antenna diameter, m	0.3	0.3	0.3
Antenna beamwidth, degrees	7.0	2.0	0.75
Range resolution, km	2.0	2.0	2.0
Number of range gate (max)	50	50	50

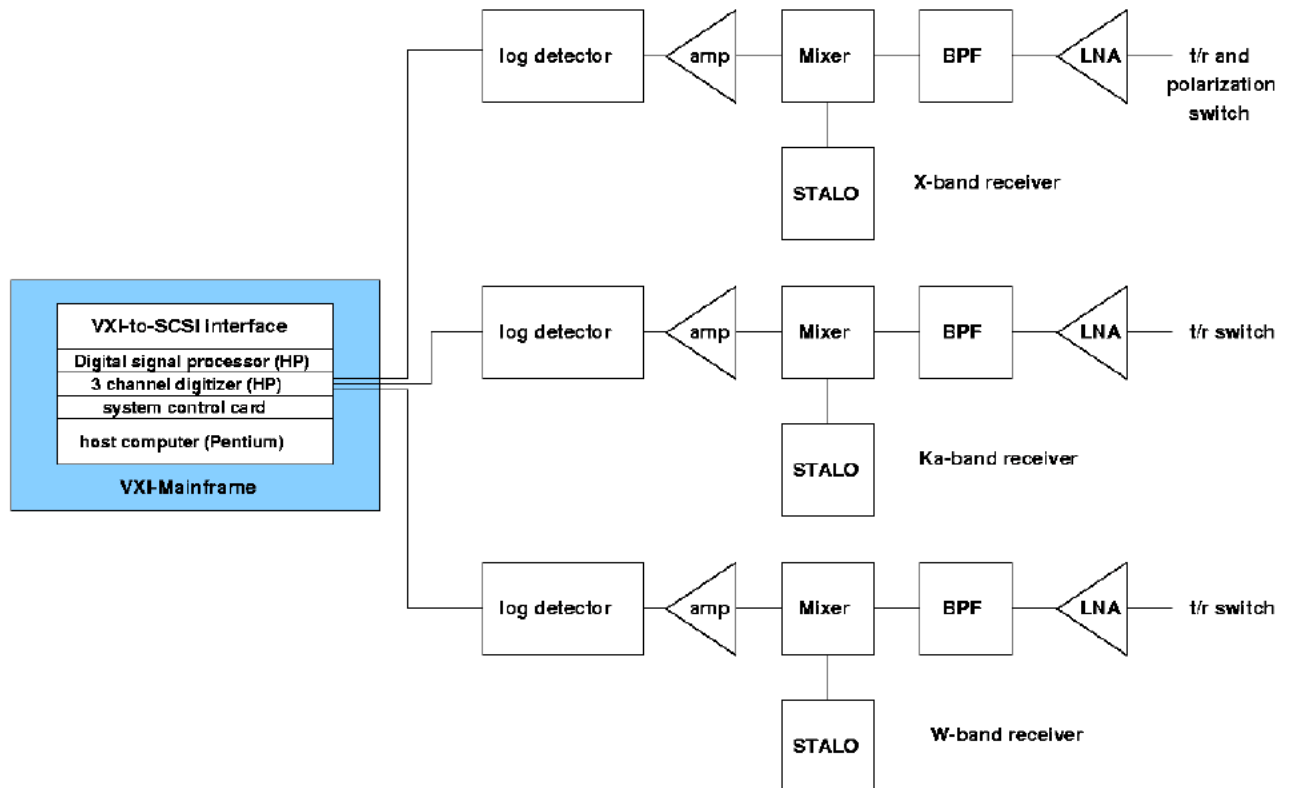


FIGURE 42. RECEIVER BLOCK DIAGRAM

7. CONCLUSIONS.

This report summarizes the results of our investigation of remote sensing technologies applicable to the problem of remote icing potential detection from aircraft. This investigation examined all of the major technologies being considered for icing detection: multifrequency radar, lidar, and radiometry, as well as novel concepts such as the airborne RASS system. Multifrequency radar proved to be the most promising method for detecting cloud parameters, including liquid water content, MVD, and MZD. The difficult problem of inverting cloud parameters from range profiles of reflected power was solved using a neural network.

A significant software development effort was undertaken to simulate random profiles of cloud and precipitation conditions for training and testing the neural network. This exercise demonstrated that a two- or three-frequency radar could remotely detect cloud parameters with kilometer-scale range resolution, even in the presence of significant measurement error. The range performance of radars at 10, 35, and 95 GHz was also simulated using published statistics on stratus clouds to show that the proposed approach is viable with existing radar technology.

Instruments capable of probing air temperature were also investigated, as they may provide a means of detecting regions of warmer air, free of supercooled drops. The technologies studied for temperature profiling included multifrequency radar, radiometry, and a radar-acoustic sensor. None of these technologies was deemed promising enough to warrant further development within the current program.

On March 10, 1998, Quadrant Engineering Inc. presented its findings to a review panel that convened at the US Army Cold Regions Research and Engineering Laboratory in Hanover, New Hampshire. Quadrant's recommendation to the panel was to continue development of the three-frequency radar system and to continue development and testing of multifrequency neural network software. Efforts are currently underway to obtain existing in-flight droplet distributions that can be used to test neural network software as well as to train a new neural network tailored to actual drop-size distributions. It must be emphasized that combined radar and in situ measurements of clouds are essential to test the ideas developed in this report.

8. BIBLIOGRAPHY.

- [Chen, 1996] Chen, C.H., editor, *Fuzzy Logic and Neural Network Handbook*, McGraw-Hill, New York, 1996.
- [Cooper et al., 1982] Cooper, W., M. Politovich, and W. Sand, "Nature of Icing Conditions Encountered During Meteorological Research," Unpublished contract report, Martin, Pringle, Oliver, Triplett, and Wallace, Wichita, Kansas, 1982.
- [Deirmendjian, 1969] Deirmendjian, D., *Electromagnetic Scattering on Spherical Polydispersions*, American Elsevier Publishing Co., Inc., New York.
- [Doviak and Zrnic, 1993] Doviak, R.J. and D.S. Zrnic, *Doppler Radar and Weather Observations*, second edition, Academic Press, San Diego, 1993.
- [Frankel and Peterson, 1976] Frankel, M.S. and A. M. Peterson, "Remote Temperature Profiling in the Lower Troposphere," *Radio Science*, 11, March 1976, pp. 157-166.
- [Galloway et al., 1998] Galloway, J., A. Pazmany, J. Mead, R. E. McIntosh, D. Leon, J. French, S. Haimov, R. Kelly, and G. Vali, "Coincident In Situ and W-Band Radar Measurements of Drop-Size Distribution in a Marine Stratus Cloud and Drizzle," to appear in *J. Atmos. Ocean. Tech.*, 1998.
- [Hubbard and Lassiter, 1951] Hubbard, H.H. and L.W. Lassiter, "Sound From a Two-Blade Propeller at Supersonic Tip Speeds," *NACA Report 1079*, 1951, pp. 457-465.
- [Hutt et al., 1994] Hutt, D., L. Bissonnette, and L. Durand, "Multiple Field of View Lidar Returns From Atmospheric Aerosols," *Applied Optics*, 33, 1994, pp. 2338-2348.
- [Huynen, 1970] Huynen, J.R., *Phenomenological Theory of Radar Targets*, Ph.D. dissertation, Drukkerij Bronder-Offset N.V., Rotterdam.
- [Jameson, 1987] Jameson, A.R., "Relations Among Linear and Circular Polarization Parameters Measured in Canted Hydrometeors," *J. Atmos. Ocean. Tech.*, v 4, pp. 634-645.
- [Marshall et al., 1972] Marshall, J.M., A.M. Peterson, and A. A. Barnes, *Applied Optics*, V. 11, January 1972, pp. 108-112.
- [Pal and Carswell, 1973] Pal, S.R. and A.I. Carswell, "Polarization Properties of Lidar Backscattering From Clouds," *Appl. Opt.*, 12, 1973, pp. 1530-1535.
- [Rumelhart et al., 1986] Rumelhart, D.E., Hinton, G.E., and Williams, R.J., "Learning Internal Representations by Error Propagation," In Rumelhart, D.E., McClelland, J.L., and the PDP Research Group, editors, *Parallel Distributed Processing*, v. 1, Chapter 8, pp. 318-362, MIT Press, Cambridge, MA, 1986.

- [Ryerson, 1996] Ryerson, C., "Remote Detection and Avoidance of In-Flight Icing," *Proceedings of the FAA International Conference on Aircraft In-flight Icing, Volume II, Working Group Papers*, August 1996, Springfield, VA, pp. 179-190.
- [Ryerson, 1997] Ryerson, C., "Prospects and Problems of Remotely Detecting In-flight Icing Potential," *Preprints of the Seventh Conference on Aviation, Range and Aerospace Meteorology*, Long Beach, CA, February 2-7, 1997, Amer. Met. Society, pp. 138-143.
- [Sassen, 1991] Sassen, K., "The Polarization Lidar Technique for Cloud Research: A Review and Current Assessment," *Bul. Amer. Met. Soc.*, 72, December 1991, pp. 1848-1866.
- [Sassen, 1998] Sassen, K., personal communications.
- [Sekelsky and McIntosh, 1995] Sekelsky, S. M. and R.E. McIntosh, "Cloud Observations With a Polarimetric 33-GHz and 95-GHz Radar," *Meteorology and Atmospheric Physics*, 58, 1996, pp. 123-140.
- [Ulaby et al., 1981] Ulaby, F.T., R.K. Moore, and A.K. Fung, *Microwave Remote Sensing, Active and Passive*, Volume 1, Addison Wesley, Reading, Mass., (456 pages).
- [14 CFR Part 25 Appendix C] *Code of Federal Regulations*, Title 14, Part 25, "Airworthiness Standards: Transport Category Airplanes."
- [Xiao, et al., 1998] Xiao, R., V. Chandrasekar, and H. Liu, "Development of a Neural Network Base Algorithm for Radar Snowfall Estimation," *IEEE Trans. Geosci. Remote Sens.*, 36, May 1998, pp. 716-724.
- [Zell et al., 1995] Zell, A. et al., *Stuttgart Neural Network Simulator User Manual, Version 4.1*, University of Stuttgart, Report number 6/95, 308 (pages).

9. GLOSSARY.

Drop-Size Distribution—The measured or modeled distribution of drop diameters for clouds or rain. Units are number of drops per meter per cubic meter or m^{-4} .

FM-CW (Frequency Modulated Continuous Wave) Radar—A radar technique that replaces a pulsed transmitter with a continuous wave transmitter. Frequency modulation is used in place of pulse modulation to allow measurements of range and velocity.

Lidar—Acronym for light detection and ranging; a laser radar.

Liquid Water Content—The water content, in grams per cubic meter, of the liquid portion of the cloud or precipitation.

Mean Volume Diameter (MVD)—Particle diameter corresponding to the mean of the volume distribution. Volume distribution is computed from the given drop-size (diameter) distribution. Note that median volume diameter is a more commonly used icing term.

Median Volume Diameter (MeVD)—Particle diameter corresponding to the median of volume distribution.

Mean Z Diameter (MZD)—Particle diameter corresponding to mean cloud reflectivity.

Mie Scattering—Mie scattering refers to the complete solution for electromagnetic scattering from dielectric spheres as computed by G. Mie in 1908. This relatively complicated formulation is required when the particle size is within an order of magnitude of the electromagnetic wavelength. Approximate formulas are often used in the optical limit ($d \gg \lambda$) and Rayleigh limit ($d \ll \lambda$) to simplify calculations.

Multiparameter Radar—Radar system capable of measuring a variety of parameters at one or more frequencies. For a meteorological radar, these parameters include cloud reflectivity, Doppler spectrum of the scattered signal (or its moments), and four additional polarimetric parameters including linear depolarization ratio LDR , differential reflectivity Z_{dr} , and the magnitude and phase of the copolarized correlation coefficient, ρ_{hv} .

Neural Network—A software algorithm used to determine output parameters based on a network of interconnected summing nodes with nonlinear response to the input. The neural network was originally developed to imitate the function of interconnected brain neurons. The basic building block of neural networks are nonlinear summing nodes that are coupled to other nodes through connections with variable weighting factors. These weighting factors, along with the transfer function of the summing nodes, are adjusted to minimize estimation errors by using a set of known input and output vectors.

Polarimetric Radar—Radar capable of measuring the polarization transformation properties of the scattering volume. Polarimetric radars usually include a polarization agile transmitter and

dual-polarization receiver. Polarimetric information is used to characterize the shape and orientation of particles within cloud or precipitation volume.

Radar Acoustic Sounding System (RASS)—A technique that combines an acoustic source with a UHF radar to remotely detect temperature by tracking the speed of sound.

Rayleigh Scattering—Simplified scattering regime for particles much smaller than the electromagnetic wavelength. For larger particles, on the order of the radar wavelength, the complete Mie solution must be computed. Scattering from particles much larger than the electromagnetic wavelength can be approximated using optical limit formulas.

Reflectivity, Z —Frequency-independent parameter equal to the sixth moment of drop-size distribution. Reflectivity is proportional to backscattered power. The sixth moment arises from the fact that the radar cross section of a small particle ($d \ll \lambda$) is proportional to the sixth power of particle diameter. Reflectivity is typically expressed on a decibel scale as dBZ , which equals $10 \log_{10}(Z)$.

APPENDIX A—ATMOSPHERIC TEMPERATURE PROFILING BY RADIOMETERS

A.1 INTRODUCTION.

Meeks and Lilley [1963] and Westwater [1965] did some of the earliest studies on radiometer temperature profiling. Decker et al. [1978] reported that ground-based radiometers operating near the oxygen absorption line frequency of 60 GHz could profile atmospheric temperature to an altitude of nearly 4 km with typical 1-2 K retrieval error. Atmospheric temperature profiling from spaceborne radiometers was demonstrated with the launch of the Nimbus-E(5) Microwave Spectrometer (NEMS) in 1972. Waters et al. [1975] reported that NEMS temperature retrieval error was 2-4 K over much of the upper atmosphere. NEMS temperature retrieval error in the lower atmosphere was significantly higher. Hogg et al. [1980] used a combination of several ground-based sensors, including a temperature profiling radiometer, to detect aircraft icing conditions near Stapleton International Airport in Denver, Colorado. This combined instrument technique yielded good results but, due to the combined size and weight of the sensors, is probably limited to ground-based operation. In this appendix we investigate the use of airborne radiometers for near-horizontal atmospheric temperature profiling.

A.2 BACKGROUND.

Key Concepts—Throughout this appendix, *range* is defined as a distance from the radiometer measured along the antenna bore-site vector.

Radiometer *sensitivity* to changes in atmospheric parameters (e.g., temperature, pressure, water vapor, and cloud liquid) is defined as the change in radiometer measured brightness temperature, T_B K, caused by a 1-unit change in the atmospheric parameter over a 1-km layer of the atmosphere. In this definition of sensitivity, the 1-km atmospheric layer is positioned perpendicular to the range vector. Sensitivity is plotted as a function of the range from the radiometer to the atmospheric layer being perturbed. Others have called these curves *weighting functions*.

Measurement Diversity—Plots of sensitivity that are constant with range indicate that the associated measurement has little value for temperature profiling. In general, radiometer temperature profiling of the atmosphere requires many measurements of atmospheric brightness temperature, each with an associated sensitivity curve that is unique from all others *and* has variation with range. Westwater et al. [1975] achieved this *diversity of measurement* using a two-frequency (53.5 and 54.5 GHz) radiometer tilted to 30 different off-zenith angles. Angle diversity can be used for vertical temperature profiling if one assumes (as Westwater did) that the atmosphere is horizontally stratified. In order to use angle diversity for horizontal temperature profiling, one must assume that the atmosphere is vertically stratified. This assumption is generally incorrect, so frequency diversity becomes the primary method of achieving the necessary measurement diversity for horizontal atmospheric temperature profiling.

Models and Assumptions—Near-horizontal temperature profiling performance of an airborne radiometer operating in 50-60 GHz was investigated. A brightness temperature measurement error, ΔT , of about 0.1 K is probably the best that can be achieved for this system.

To permit calculation of radiometer sensitivity and atmospheric brightness temperature, we have implemented in software the radiative transfer integral [Ulaby et al., 1986] and the atmospheric models shown in table A-1.

TABLE A-1. MODELS FOR ATMOSPHERIC ABSORPTION OF MICROWAVES

Parameter	Reference
Oxygen (O ₂)	Liebe et al. [1992]
Water Vapor	Cruz-Pol et al. [1996], Liebe et al. [1987]
Cloud Water	Westwater [1974]

We have assumed that the atmosphere is spherically stratified (round Earth effects) and that the vertical profiles for water vapor, temperature, and pressure are those of the 1962 U.S. Standard Atmosphere [Ulaby et al., 1986]. Throughout this study we assume the radiometer to be at an altitude of 2 km above sea level.

Inversion Algorithm—The Backus-Gilbert algorithm [Backus and Gilbert, 1970] [Westwater and Cohen, 1973] is used to estimate the near-horizontal profile of atmospheric temperature from the brightness temperature measurements of the radiometer. The Backus-Gilbert technique provides convenient tools for studying temperature retrieval error, range resolution, and the tradeoff between error and resolution.

A.3 ANALYSIS AND DISCUSSION.

Atmospheric Depth—Figure A-1 shows the altitude of an atmospheric element located at various ranges from a radiometer as well as for various off-zenith radiometer tilt angles. Figure A-2 shows typical sky brightness temperatures seen by a radiometer pointed 70°-90° off zenith. Close to 60 GHz, a near saturation condition exists for the radiometer measurements (i.e., brightness temperature is approximately equal to ambient air temperature). This observation suggests that radiometer measurements made at these frequencies have limited depth of measurement. Indeed, figure A-3 shows that for frequencies between 55-60 GHz, the radiometer measured brightness temperature is determined primarily by emission from the 10 km of atmosphere immediately in front of the radiometer. However, for frequencies lower than 55 GHz, figure A-3 shows radiometer depth of measurement to be well over 30 km. Longer depth of measurement is desirable for long-range temperature profiling but does make measurements susceptible to contamination from long-range sources (e.g., ground emission).

Temperature Sensitivity—Figure A-4 shows that radiometer measurements made in the 50- to 60-GHz band have good sensitivity to changes in atmospheric temperature. Temperature sensitivity is the change in radiometer measured brightness temperature caused by a 1 K change in air temperature over a 1-km layer of atmosphere (see also section A.2). These curves are for a radiometer located 2 km above sea level in a U.S. Standard Atmosphere and tilted 90° off zenith. The family of temperature sensitivity curves shown in figure A-4 were achieved using frequency diversity (see section A.2) but are very similar to the family of sensitivity curves which Westwater [1975] achieved through angle diversity. This observation indicates that performance (in terms of error and range resolution) of the horizontal temperature profiling radiometer should

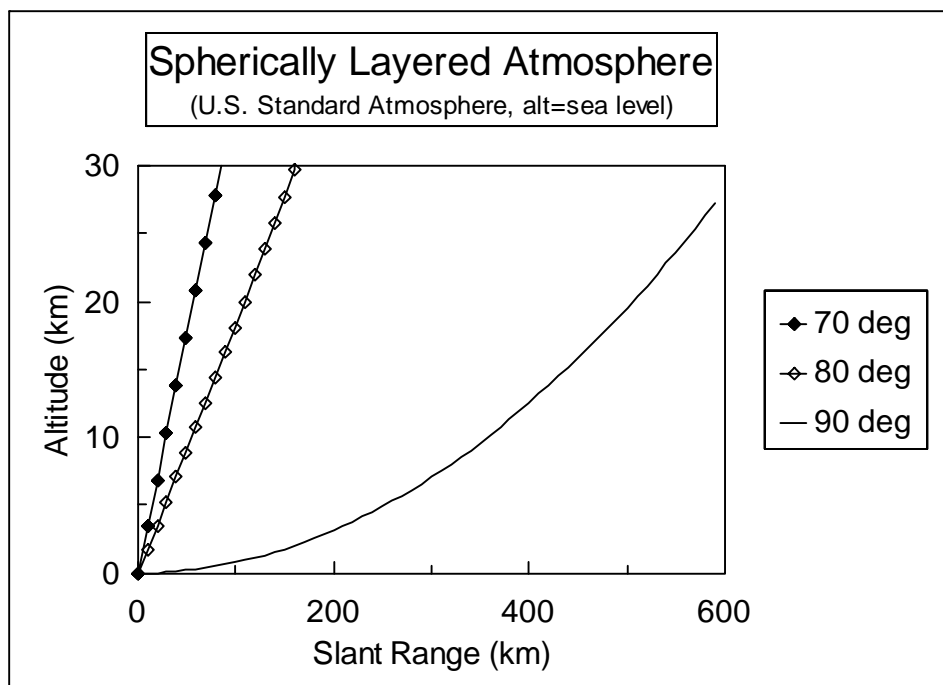


FIGURE A-1. ALTITUDE OF ATMOSPHERIC ELEMENT AT VARIOUS SLANT RANGES FROM A POINT AT SEA LEVEL

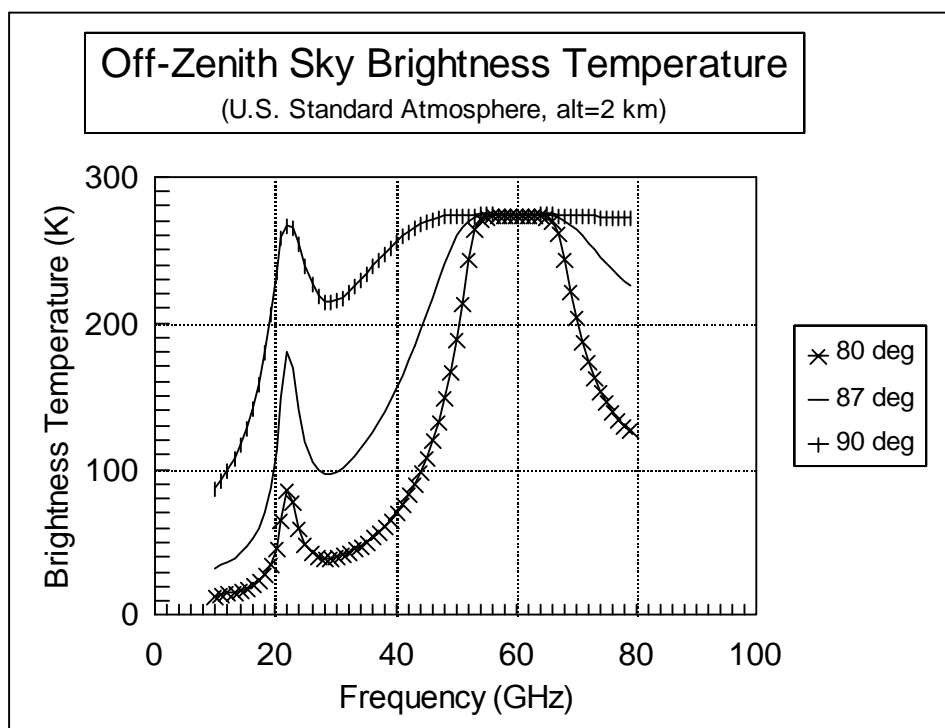


FIGURE A-2. OFF-ZENITH SKY BRIGHTNESS TEMPERATURE SEEN BY RADIOMETER AT 2-km ALTITUDE

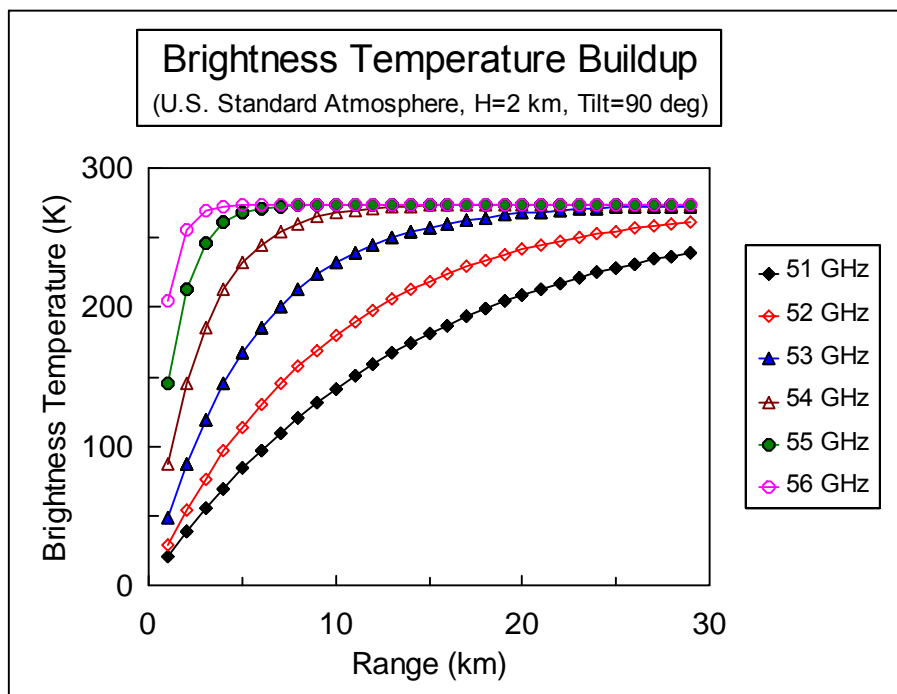


FIGURE A-3. CONTRIBUTIONS OF VARIOUS ATMOSPHERIC LAYERS TO TOTAL SKY BRIGHTNESS TEMPERATURE

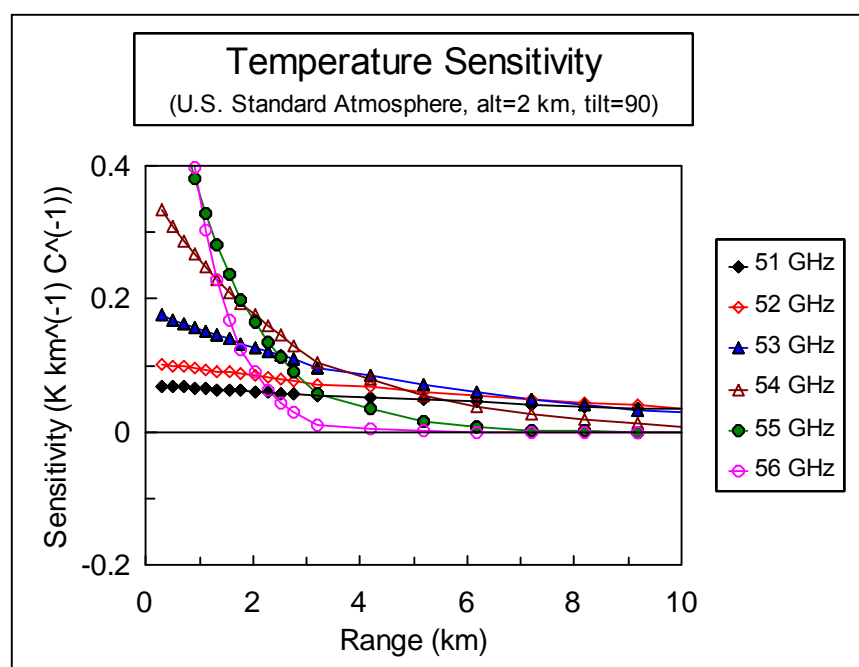


FIGURE A-4. SENSITIVITY OF RADIOMETER MEASUREMENTS IN THE 51- TO 56-GHz BAND TO ATMOSPHERIC TEMPERATURE

be similar to that of Westwater's [1975] vertical temperature profiling radiometer (see figure A-11 and the associated discussion in this appendix).

Sources of Error—Factors affecting atmospheric temperature profiling error generally fall into one of the following three groups:

- Radiometer measurement error (i.e., ΔT).
- Variations in the attenuation profile along the range vector.
- Variations in the background emission.

Radiometer measurement error depends on system design, bandwidth, and the averaging time associated with the data [Tiuri, 1964]. A brightness temperature measurement error, ΔT , of 0.1 K is readily achievable.

Atmospheric temperature profiling performance depends significantly upon how accurately the attenuation profile along the range vector is known. Atmospheric attenuation in the 50- to 60-GHz range at an altitude of 2 km is predominantly due to oxygen absorption but is affected by other atmospheric constituents as shown in table A-2.

TABLE A-2. SOURCES OF ATMOSPHERIC ATTENUATION IN THE 50- TO 60-GHz BAND

Cause	Attenuation (dB/km)
Oxygen (O ₂)	1-10
Clouds	1-10
Rain	0.1-10
Water Vapor (saturation)	0.1

Note that clouds and rain both attenuate microwaves in the 50- to 60-GHz band at a rate similar to that of oxygen. Therefore, the range distribution of clouds, rain, and liquid water must be accounted for during the atmospheric temperature retrieval process.

Background emission consists of cosmic and ground emission. Cosmic emission is constant at about 2.7 K in the 50- to 60-GHz band but ground emission is variable. For the horizontal temperature profiling radiometer, the portion, $T_A(gnd)$, of the total measured brightness temperature which is attributed to ground emission can be calculated as

$$T_A(gnd) = T_G \cdot S_G \quad (A-1)$$

where

$$S_G = \frac{1}{4\pi} \cdot \int_{\pi/2}^{\pi} \int_0^{2\pi} G(\theta - \frac{\pi}{2}, \phi - \pi) \cdot L(\theta, \phi) \cdot \sin(\theta) \cdot d\phi \cdot d\theta$$

$G(\theta, \phi)$ is the radiometer antenna pattern, $L(\theta, \phi)$ is attenuation of the atmosphere between the radiometer and the ground along the path defined by spherical coordinate angles θ and ϕ , and

T_G is the ground brightness temperature (assumed to be uniform). We define the term S_G as the *ground sensitivity* of the radiometer and note that it is the error in total calculated brightness temperature caused by a 1 K error in the estimate of the ground temperature, T_G . Plots of radiometer ground sensitivity are shown in figures A-5 and A-6 where a Gaussian-shaped beam pattern has been used to approximate the sidelobes of the antenna. These plots show that ground sensitivity depends strongly upon radiometer altitude and beamwidth.

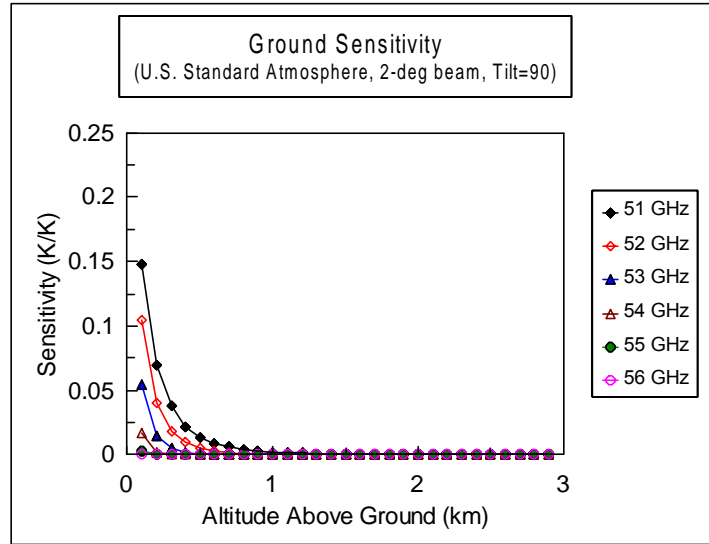


FIGURE A-5. SENSITIVITY OF RADIOMETER WITH 2-DEGREE BEAMWIDTH, OPERATING IN THE 51- TO 56-GHz BAND TO GROUND BRIGHTNESS TEMPERATURE

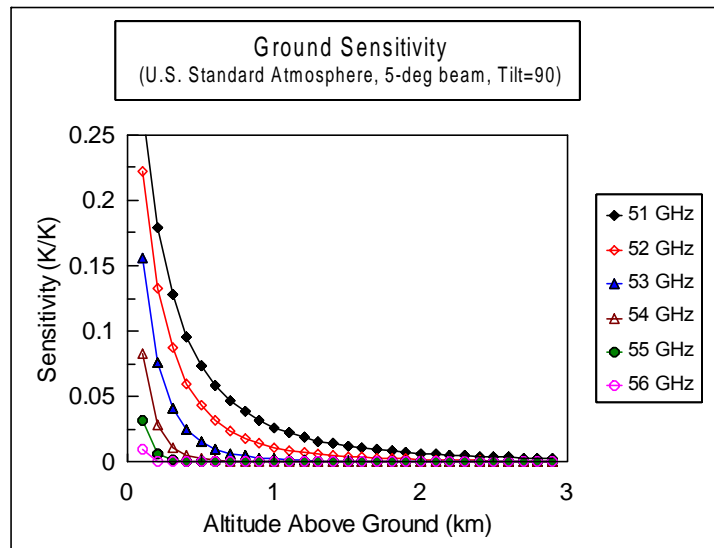


FIGURE A-6. SENSITIVITY OF RADIOMETER WITH 5-DEGREE BEAMWIDTH, OPERATING IN THE 51- TO 56-GHz BAND TO GROUND BRIGHTNESS TEMPERATURE

Profiling Performance—This temperature profiling performance analysis assumes that the radiometer field of view is free of clouds and rain. Attenuation due to rain or clouds will change the shape of the weighting functions used in inverting temperature and will result in significant errors if left uncompensated. If some other method is used to estimate attenuation due to liquid water (e.g., multifrequency radar) then the inversion can be corrected to account for additional attenuation. However, the presence of heavy clouds or rain between the radiometer and the sample volume will bias the weighting functions to short ranges, making it impossible to sense temperature at long distances.

The Backus-Gilbert (BG) technique [Backus and Gilbert, 1970] is used to calculate the atmospheric temperature profile from radiometer brightness temperature measurements. The BG technique utilizes a parameter, α , which varies between 0 and 1 and in many applications permits a tradeoff between range resolution and temperature retrieval error. In general, values of the BG parameter, α , near 1 will result in high-range resolution and high-retrieval error. Values of α near 0 typically result in low-range resolution and low-retrieval error. However, significant tradeoff between range resolution and temperature retrieval error does not appear possible for the temperature profiling radiometer, and the reason for this is still under investigation.

Temperature profiling range resolution is defined as the half-height width of the BG *averaging kernel*. Averaging kernels demonstrate how values from the entire temperature profile are weighted and averaged to produce the retrieved estimate of temperature at a particular range. For all values of range, there is an associated averaging kernel. The range associated with a particular kernel is located approximately at its centroid. The centroid of the averaging kernel does not always coincide with the position of the kernel maxima.

The BG technique defines retrieval error in terms of a noise multiplication factor. For the temperature profiling problem, retrieval error (K) is equal to this multiplication factor times the brightness temperature measurement error, ΔT , of the radiometer.

Figures A-7 and A-8 show temperature profiling performance for the near 60-GHz radiometer as determined by the BG technique with $\alpha = 0.5$. Brightness temperature measurements at 15 frequencies, spaced more or less evenly across the 50- to 60-GHz band, are the inputs to the BG algorithm. Our computer simulations show that using values of α higher than 0.5 does not significantly improve range resolution but will significantly increase retrieval error.

Temperature profiling to a range of about 4 km appears possible if radiometer measurements are restricted to the 55- to 60-GHz band (see figures A-9 and A-10). These plots end at about 4-km range because the BG technique cannot form well defined averaging kernels much beyond this point. The advantage of the 55- to 60-GHz system is its limited depth of measurement and resulting reduced sensitivity to ground contamination. Temperature profiling with this type of system can probably be done in any direction from the aircraft, perhaps even towards the ground if flight altitude is high enough.

Finally, we note that the horizontal temperature profiling performance curve (figure A-7) is similar to Westwater's [1975] result, which is summarized in figure A-11. One finds that temperature sensitivity of the near 60-GHz radiometer does not depend significantly on off-

zenith tilt angle or on flight altitude; hence, the performance of Westwater's [1975] ground-based vertical temperature profiling system should be similar to that of the near-horizontal temperature profiling system.

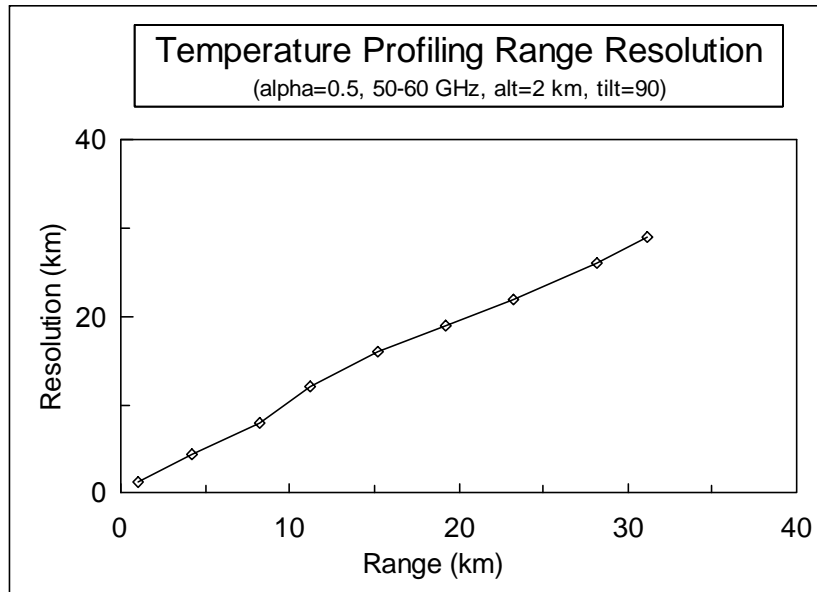


FIGURE A-7. HORIZONTAL TEMPERATURE PROFILING RANGE RESOLUTION FOR THE 50- TO 60-GHz RADIOMETER AT ALTITUDE, 2 km
(Backus-Gilbert parameter, $\alpha = 0.5$)

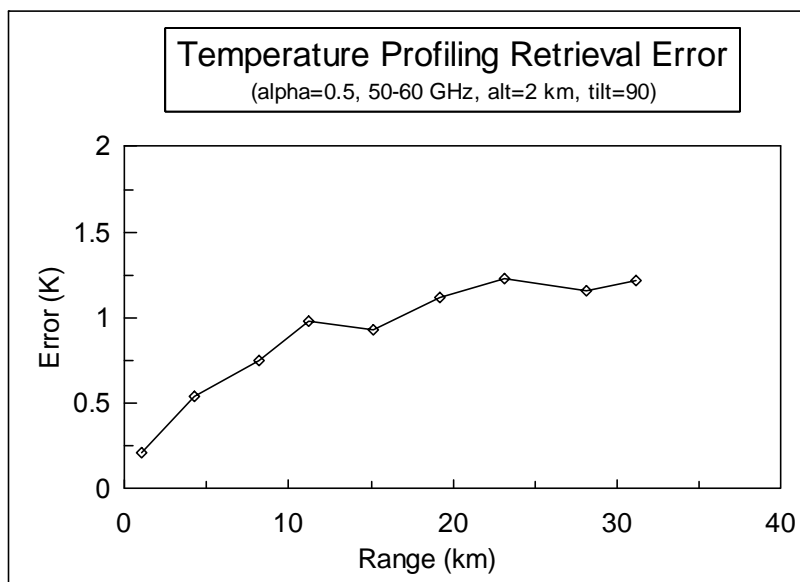


FIGURE A-8. HORIZONTAL TEMPERATURE PROFILING RETRIEVAL ERROR FOR THE 50- TO 60-GHz RADIOMETER AT ALTITUDE, 2 km, WITH $\Delta T = 0.1$ K
(Backus-Gilbert parameter, $\alpha = 0.5$)

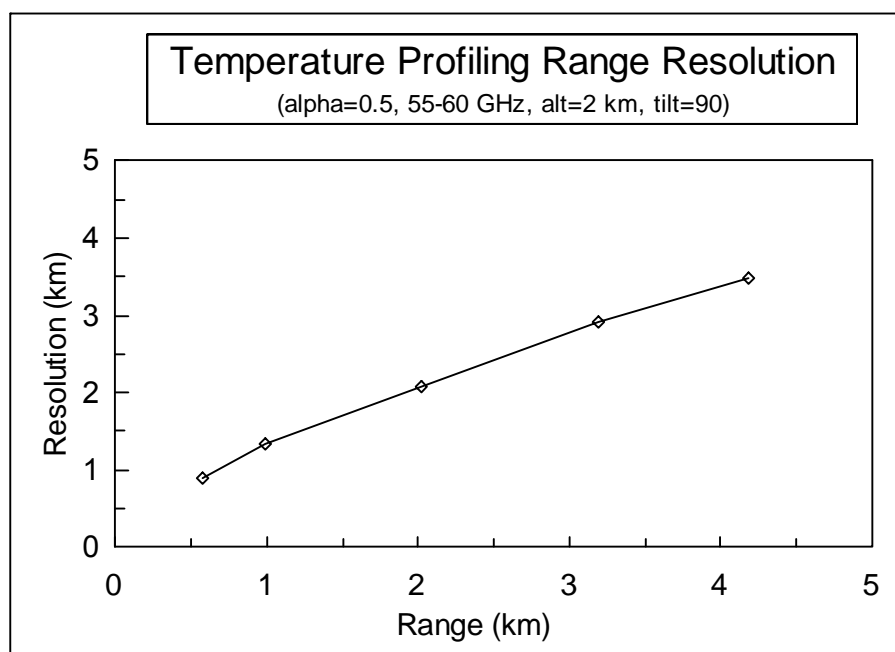


FIGURE A-9. HORIZONTAL TEMPERATURE PROFILING RANGE RESOLUTION FOR THE 55- TO 60-GHz RADIOMETER AT ALTITUDE, 2 km
(Backus-Gilbert parameter, $\alpha = 0.5$)

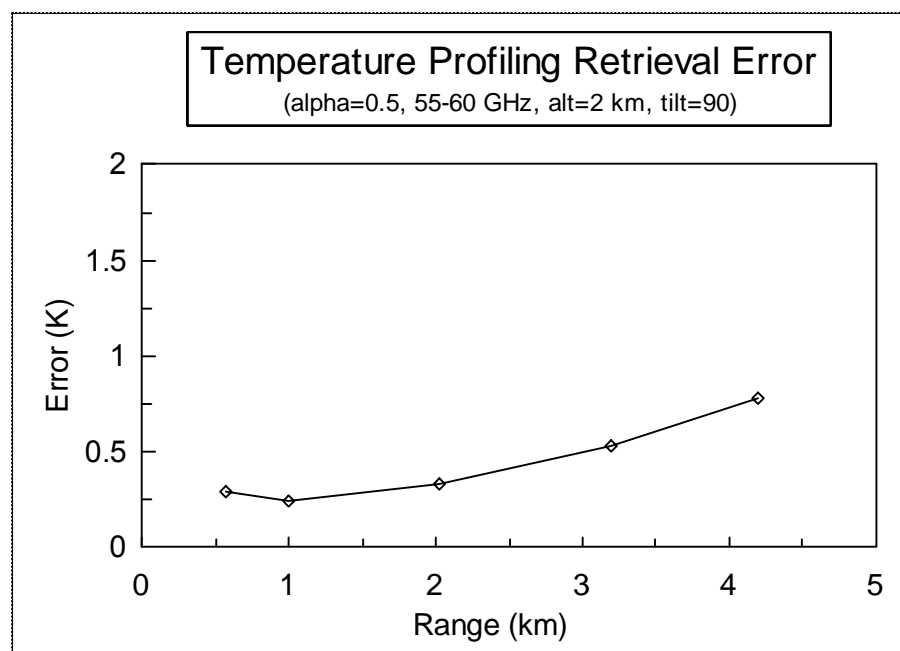


FIGURE A-10. HORIZONTAL TEMPERATURE PROFILING RETRIEVAL ERROR FOR THE 55- TO 60-GHz RADIOMETER AT ALTITUDE, 2 km, WITH $\Delta T = 0.1$ K
(Backus-Gilbert parameter, $\alpha = 0.5$)

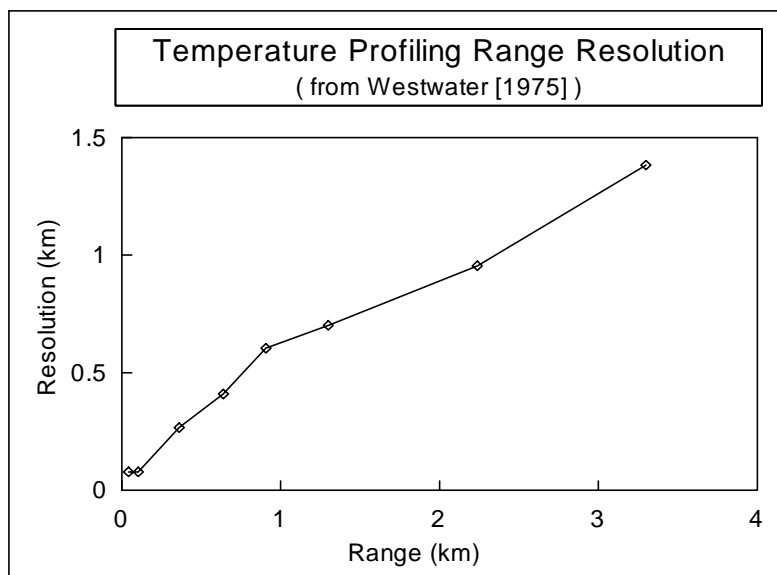


FIGURE A.11. RANGE RESOLUTION OF A GROUND-BASED VERTICAL TEMPERATURE PROFILING SYSTEM (After Westwater [1975])
(Associated temperature retrieval error is 1-2 K)

CONCLUSIONS.

Temperature profiling using a 50- to 60-GHz radiometer will work with an accuracy similar to vertical profiling radiometers (2-3 K, rms) when range resolution is scaled linearly (1:1) with range. Designing the radiometer with a narrow beamwidth (2 degrees or less) is critical to reducing contamination by ground temperature fluctuations. This implies an antenna aperture of greater than 20 cm diameter. In addition, some auxiliary method must be used to correct for liquid water and water vapor fluctuations. For example, the estimate of liquid water content made by the neural network algorithm could be used to correct the radiometer data.

Several implementation problems suggest that the technique may not be practical. These problems include correcting for liquid water at ranges beyond the detection capability of the radar and accounting for loss due to water and ice on the radome. Also, the coarse range resolution at long ranges (for example, 20-km resolution at 20-km range) may not afford the resolution necessary for a useful icing avoidance system.

REFERENCES.

- Backus G. and F. Gilbert (1970), Uniqueness in the Inversion of Inaccurate Gross Earth Data, *Phil. Trans. Roy. Soc. London, Ser. A* 266, pp. 123-129.
- Cruz Pol, S.L., C.S. Ruf, and S.J. Keihm (1996), "Atmospheric Microwave Absorption Parameter Estimation Near 22 GHz," *Proc. IGARSS '96 Symposium*.
- Decker, M.T., E.R. Westwater, and F.O. Guiraud (1978), "Experimental Evaluation of Ground-Based Microwave Radiometric Sensing of Atmospheric Temperature and Water Vapor Profiles," *J. Appl. Meteorol.*, 17, pp. 1788-1795.
- Hogg, D.C., F.O. Guiraud, and E.B. Burton (1980), "Simultaneous Observations of Cool Cloud Liquid by Ground-Based Microwave Radiometry and Icing of Aircraft," *J. Appl. Meteorol.*, 19, pp. 893-895.
- Liebe, H.J. and D.H. Clayton (1987), *Millimeter-Wave Properties of the Atmosphere: Laboratory Studies and Propagation Modeling*, Nat. Telecom. and Inform. Admin., Boulder, CO, NIT Rep. 87-24.
- Liebe, H.J., P.W. Rosenkranz, and G.A. Hufford (1992), "Atmospheric 60 GHz Oxygen Spectrum: New Laboratory Measurements and Line Parameters," *J. Quant. Spectrosc. Radiat. Transfer*, 48, 5/6, pp. 629-643.
- Meeks M.L. and A.E. Lilley (1963), "The Microwave Spectrum of Oxygen in the Earth's Atmosphere," *J. Geophys. Res.*, 68, pp. 1683-1703.
- Tiuri, M.E. (1964), *Radio Astronomy Receivers*, *IEEE Trans. Anten. Propagat.*, AP-12, 7, pp. 930-938.
- Ulaby F.T., R.K. Moore, and A.K. Fung (1986), *Microwave Remote Sensing (Active and Passive)*, vol. I, Addison-Wesley Publishing Company, Reading, MA.
- Waters, J.W., K.F. Kunzi, R.L. Pettyjohn, R.K.L. Poon, and D.H. Staelin (1975), "Remote Sensing of Atmospheric Temperature Profiles With the Nimbus 5 Microwave Spectrometer," *J. Atmos. Sci.*, 32, pp. 1953-1969.
- Westwater, E.R. (1965), "Ground-Based Passive Probing Using the Microwave Spectrum of Oxygen," *Radio Sci.*, 69D, pp. 1201-1211.
- Westwater, E.R. and A. Cohen (1973), "Applications of Backus-Gilbert Inversion Technique to Determination of Aerosol Size Distributions from Optical Scattering Measurements," *Appl. Opt.*, 12, pp. 1340-1348.
- Westwater, E.R. (1974), "Microwave Emission From Clouds," *Tech. Rep. ERL-219-WPL 18*, NOAA/Environmental Research Laboratories, Boulder, CO.

Westwater E.R., J.B. Snider, and A.V. Carlson (1975), "Experimental Determination of Temperature Profiles by Ground-Based Microwave Radiometry," J. Appl. Meteor., 14, pp. 524-539.

APPENDIX B—FRONT-END LOSS EFFECTS ON RADIOMETER PERFORMANCE

Ice forming on a radiometer antenna radome will cause the brightness temperature, T_a , seen by the radiometer receiver to be a combination of the apparent target brightness temperature, T_A , and other terms [Hardy et al., 1974] as shown in equation B-1.

$$T_a = T_A (1-r)(1-l) + l T_L + r T_R \quad (\text{B-1})$$

In equation B-1, r is ice reflective loss, l is ice ohmic loss, T_L (K) is ice physical temperature and T_R (K) is the brightness temperature of the radiometer receiver noise propagating towards the antenna. The values r and l vary between zero (no loss) and one (no transmission).

The accuracy, ΔT_a (K), with which the radiometer can measure T_a is determined solely by radiometer receiver parameters. For a Null Feedback Dicke-Switched receiver design, ΔT_a is given by equation B-2 [Tiuri, 1964],

$$\Delta T_a = 2 T_{\text{SYS}} / (B \tau)^{0.5} \quad (\text{B-2})$$

where T_{SYS} (K) is system noise temperature, B (Hz) is predetector bandwidth, and τ (s) is data averaging time. Brightness temperature measurement accuracy, ΔT_A (K), will be affected by the ice even if r , l , and T_L are time invariant as shown in equation B-3 and in figure B-1.

$$\Delta T_A = \Delta T_a / ((1-r)(1-l)) \quad (\text{B-3})$$

Ice also affects both the scale, a , and bias, b , factors found in the radiometer calibration equation used to convert radiometer output voltage, V , to a value of T_A .

$$T_A = a V + b \quad (\text{B-4})$$

For the typical values $T_L = 273$ K and $T_R = 300$ K, the icing induced error (bias) in the calculated value of T_A is shown in figure B-2. In practice, measurements of ambient air temperature can be used to estimate T_L , T_R can be measured during laboratory calibration of the radiometer, and should remain relatively constant with time.

The conclusion is that very little front-end loss can be tolerated if radiometer measurement accuracy on the order of 0.1 K is desired. Our calculations predict that this amount of loss can be caused by as little a 1-mm layer of water or ice on the antenna radome.

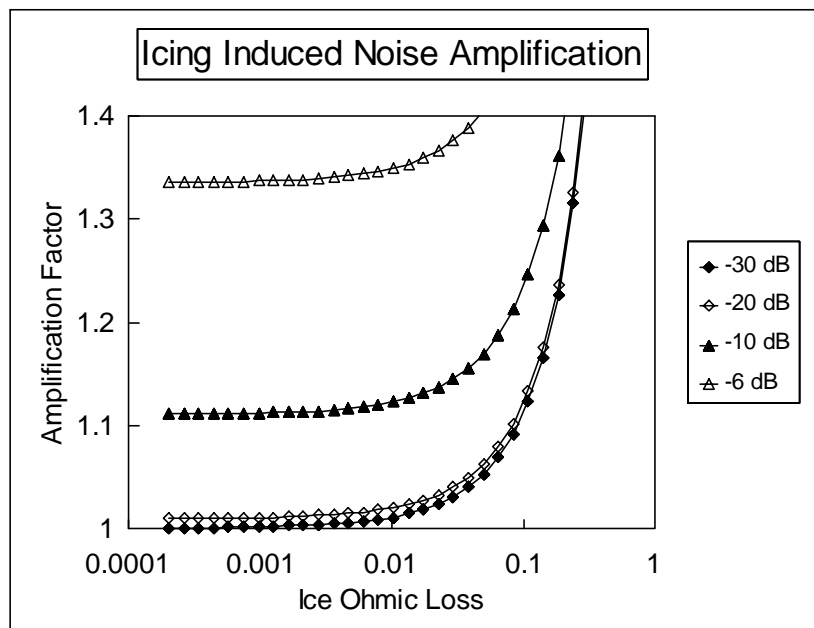


FIGURE B-1. TYPICAL INCREASE IN BRIGHTNESS TEMPERATURE MEASUREMENT ERROR CAUSED BY RADOME ICING (Each curve represents a different value of ice reflective loss)

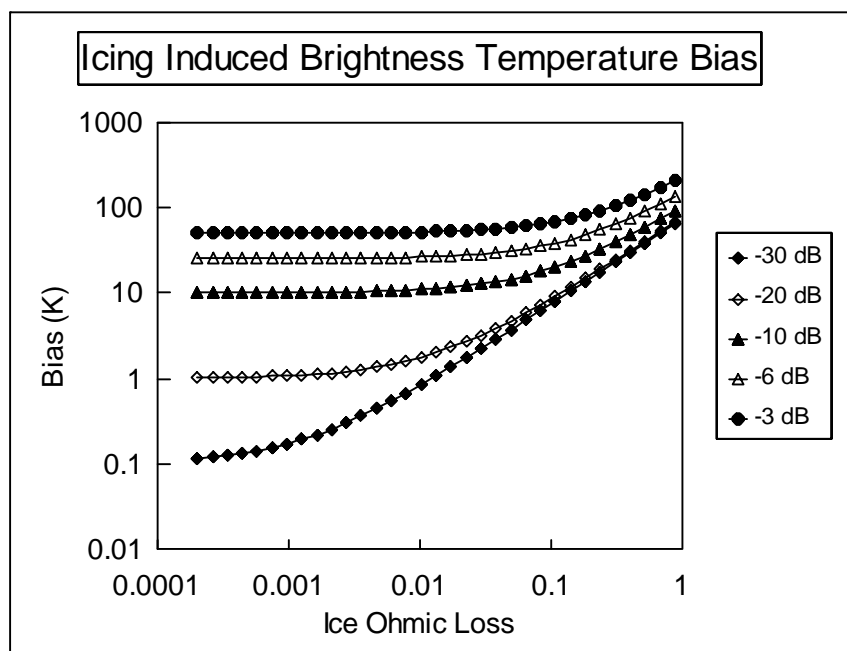


FIGURE B-2. TYPICAL BRIGHTNESS TEMPERATURE BIAS CAUSED BY RADOME ICING (Each curve represents a different value of ice reflective loss, e.g., $R = 0.001$ (low loss) is shown as -30 dB)

REFERENCES.

Hardy W.N., K.W. Gray, and A.W. Love (1974), An S-Band Radiometer Design With High Absolute Precision, IEEE Trans. Microwave Theory Tech., 22, 4, pp. 382-390.

Tiuri, M.E. (1964), Radio Astronomy Receivers, IEEE Trans. Anten. Propagat., AP-12, 7, pp. 930-938